Physics Reports 795 (2019) 1–51

Contents lists available at ScienceDirect

Physics Reports

journal homepage: www.elsevier.com/locate/physrep

Photonics and optoelectronics using nano-structured hybrid perovskite media and their optical cavities

Yupeng Zhang [a], Chang-Keun Lim [b], Zhigao Dai [c], Guannan Yu [a], Joseph W. Haus [d], Han Zhang [a,*], Paras N. Prasad [b,*]

[a] *Collaborative Innovation Center for Optoelectronic Science and Technology and Key Laboratory of Optoelectronic Devices and Systems of Ministry of Education and Guangdong Province, and College of Electronic Science and Technology, Shenzhen University, Shenzhen 518060, PR China*
[b] *Institute for Lasers, Photonics, and Biophotonics and Department of Chemistry, University at Buffalo, State University of New York, Buffalo, USA*
[c] *School of Printing and Packaging and School of Physics and Technology, Wuhan University, Wuhan 430072, PR China*
[d] *Department of Electro-Optics and Photonics, University of Dayton, Dayton, OH 45469-2951, USA*

ARTICLE INFO

Article history:
Received 14 September 2018
Available online 6 February 2019
Editor: G. E. W. Bauer

ABSTRACT

This review focuses on the physics of optical excitation dynamics, band gap engineering and charge carrier dynamics in metal-halide perovskites and their organic hybrids as well as on their technological applications. The role of plasmonic coupling and photonic cavities in enhancing light–matter interactions and manipulating carrier dynamics is clearly presented by examples of studies of perovskite–hybrid plasmonic nanostructured perovskite cavities. Perovskite metasurface is a nascent approach to enhancing photonic device performance that is also briefly described. In addition, nonlinear optical interactions and charge carrier dynamics in (pseudo-) 2D perovskites and photonic structures are discussed. We discuss how photonic communication between a perovskite layer and an interlayer of photoactive organic material in hybrid perovskites contributes to new designs for novel devices. Applications covered are: photodetectors, solar cells, light-emitting diodes and nanolasers, displays, waveguides and modulators, and nonlinear optical devices. Device performance is enhanced by incorporating nanophotonics design concepts. The review concludes with a discussion of technical challenges. New opportunities in multiscale modeling, perovskites with epsilon near zero, perovskites–plasmonic semiconductors, perovskite sensors and quantum applications are presented also presented in the concluding outlook section.

Contents

---

[*] Corresponding authors.
E-mail addresses: hzhang@szu.edu.cn (H. Zhang), pnprasad@buffalo.edu (P.N. Prasad).

https://doi.org/10.1016/j.physrep.2019.01.005

1. Introduction

Metal-halide perovskite semiconductors generally have a crystal structure in the form of ABX_3 with A designating a monovalent inorganic or organic cation [*e.g.*, cesium, Cs^+; methylammonium (MA), $CH_3NH_3^+$; or formamidinium (FA), $CH(NH_2)_2^+$], B as a bivalent metal cation (*e.g.*, Pb^{2+}, Sn^{2+} or Ge^{2+}) and X as a halide anion (*e.g.*, I^-, Br^- or Cl^-) [1,2]. The cations have very different sizes and fit into different coordination sites of the crystal lattice. In addition to their possessing a high absorption coefficient ($\sim 5 \times 10^4$ cm^{-1}) [3], an optical band-gap that is tunable across the entire visible spectrum to near infrared region, is easily realized in metal-halide perovskite crystals by compositional substitution via solution, vapor and solution-vapor hybrid processing [4–8]. The halide perovskites also exhibit unique electronic properties [9–11] such as electron–hole diffusion lengths longer than 175 μm in $CH_3NH_3PbI_3$ bulk single-crystals [12], but longer than 1 μm in perovskite polycrystalline films [13], and strong charge depletion characteristics with a depletion width over 10 μm in $CH_3NH_3PbI_3$ nanosheet-based *p*-*n* junctions [14].

Perovskite compounds have been studied for decades, but awareness of their unusual properties rapidly spread with the recent discovery of high-efficiency solar cells achieving validated efficiencies exceeding 23% with potential for more than 30% [15]. Due to their outstanding optical and electronic properties, in association with ease of thin film preparation, research and development in halide perovskite-based photonics and optoelectronics related applications have evolved quickly in the past decade, achieving continually various exciting landmarks each year. The increased interest in perovskite properties and applications is revealed by the timeline of publication records (Fig. 1). The number of publications per year has increased drastically since 2009, with the sharpest increase being after 2013 following the report of high solar cell efficiency.

In the solar field, significant research efforts reported high-performance photovoltaic cells with power conversion efficiency increasing from 3.8% in 2009 to 23.3% reported very recently [16,17]; this rapid progress in high-efficiency solar cells is unprecedented. In fact, the efficiency has already exceeded that of multi-crystalline silicon solar cells (22.3%) [17], clearly demonstrating the tremendous potential for optoelectronic applications of the perovskite family.

While energy harvesting is a notable field of research, considerable attention is drawn toward much broader and more significant photonic and optoelectronic applications. For instance, light-emitting devices (LEDs) employing metal-halide perovskite emitters have demonstrated excellent performance with photoresponsivity beyond 62 cd A^{-1} and external quantum efficiency of 14% [18]; these performance values are already comparable to the state-of-the-art organic LEDs. Similarly, ultrasensitive photodetectors with responsivity over 10^4 AW^{-1} and detectivity higher than 10^{15} Jones have been

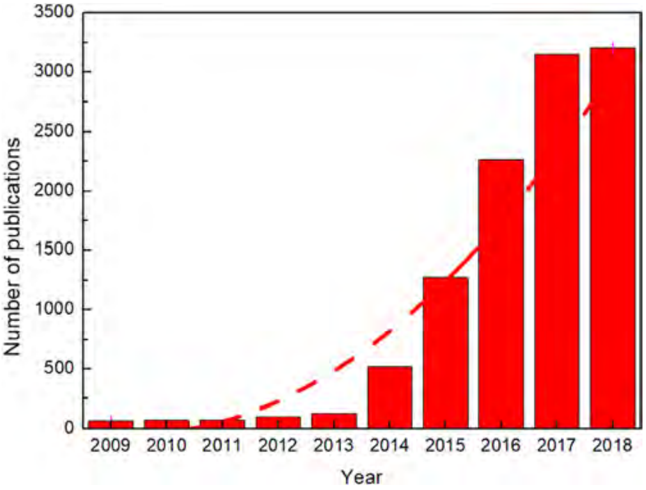

Fig. 1. Publication output per year on perovskite for the period 2009 to 2018.

achieved by using single-crystalline layered metal-halide perovskites, far exceeding the performance of commercial Si-based photodiodes [19].

In addition to the above-mentioned exciting progress in materials engineering and device fabrication, metal-halide perovskites can achieve additional improvements by hybridizing devices incorporating several areas of nanophotonics, namely plasmonics and nanoscale cavity structures [20–22]. There is a myriad of established design tools that researchers bring to bear in resolving technical issues and for performance improvements. There are unprecedented possibilities in photonics and optoelectronics by joining the perovskite's optoelectronic characteristics with advanced optical cavities, to accelerate the development of more efficient devices.

Particularly, low-dimensional halide perovskites including zero-dimensional (0D), one-dimensional (1D) and two-dimensional (2D) crystals are rapidly emerging as new types of nanoscale photonic and optoelectronic components [23–26]. A photonic cavity generally utilizes multiple reflection, absorption or diffraction of light in a confined space and can provide useful enhanced light–matter interactions. Nanostructured hybrid perovskite crystals including nanowires and nanoplatelets have been demonstrated recently with an active wave-guiding performance for optical modulators [27,28], as well as with low lasing thresholds and high-quality factors [29–31]. Nanopatterning perovskite films into periodic arrays increase the light coupling efficiency in the device; for instance, periodic patterns and perovskite metasurfaces assist in enhancing light absorption in solar cells and light extraction for LEDs [32,33]. Coupled with external optical cavities including distributed Bragg reflector (DBR) and photonic crystal, halide perovskites also show improved light emission performance (*e.g.*, polariton condensation and lasing in a $CsPbCl_3$-DBR cavity) [34–36].

Plasmonic coupled metal-halide perovskite systems possess great potential in enhancing the optical response of perovskites. Plasmonic effects are classified into two categories: localized surface plasmon resonance (LSPR) and propagating (or delocalized) surface plasmon polariton (SPP) [20]. Extensive efforts are made to exploit the coupling effect between conventional semiconductors and plasmonic structures, and understand the coupling mechanisms that can enable researchers to develop high-efficiency plasmonic-enhanced optoelectronic devices [37–40]. Similarly, plasmonic nanostructures can be incorporated into metal-halide perovskite-based devices in order to evoke plasmonic enhancement of specific optical phenomena [41–43]. For instance, preliminary studies that combine perovskites with plasmonic metal nanoparticles (*e.g.*, Au, Ag) have demonstrated a ∼28% improvement in solar cell power conversion efficiency [44] and ∼40% improvement in external quantum efficiency of LEDs [45]. Periodic arrays of metallic nanostructures can also be used to modulate the responsive optical spectra and boost the photon/electron conversion efficiency in perovskite optoelectronic devices [46–48]. For example, the external quantum efficiency of a perovskite photodetector functionalized by arrays of Au nanostructures exhibits 2.5 times enhancement due to the huge localized electric field induced by the surface plasmon resonance [46].

A conceptual roadmap of the substance of this review is illustrated in Fig. 2. On the top level, broad bandwidth optical radiation can be absorbed to produce a current response or photon emission can be elicited from electron/hole recombination to create efficient light emission devices. On the lower tier, plasmonic structures or photonic (crystal) cavities can boost electron/photon interactions for useful devices. Here we focus on the physics of optical excitation dynamics, band gap engineering and charge carrier dynamics in metal-halide perovskites. The role of plasmonic coupling and photonic cavities in enhancing light–matter interactions and manipulating carrier dynamics is presented by examples of studies of perovskites hybrid plasmonic and perovskites nanostructure cavities. We further discuss how photonic communication between perovskite and optical gain structures contributes to new designs for novel photonic devices.

In this review, we make an attempt to capture the recent advances in nanostructured metal-halide perovskite media and their optical cavities, discuss the fundamental physical and photonic mechanisms and summarize the potential device

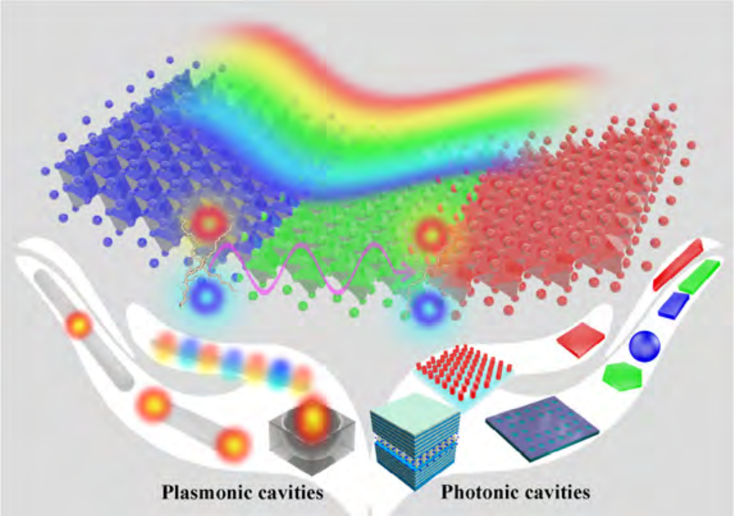

Fig. 2. Illustration to capture the key concepts explained in this review.

applications in photonics and optoelectronics. Future research scopes in this field are also presented. It is therefore anticipated that this review will strengthen the understanding of halide perovskite-based optical cavities and stimulate research and development of high-performance photonic and optoelectronic devices.

2. Optical properties of metal-halide perovskites materials

A metal-halide perovskite crystal can be viewed as an anion corner-shared 3D network of $(BX_6)^{4-}$ octahedra, with B cations at their centers and A cations between them. Generally, the designated A cation is supposed to have no direct contribution to the electronic properties of perovskites, and the band structures of perovskites are mainly correlated with the largest metal-halide-metal bond angle, which according to theoretical investigations can be adjusted by the BX_6 octahedral tilting [49]. The valence band maximum (VBM) consists of anti-bonding states derived from hybridizations of the atomic *p* electron orbitals in the valence shell of the halide and 6*s* orbitals of lead, whereas the conduction band minimum (CBM) is mainly formed of empty 6*p* electron orbitals of lead. Representatively, in methylammonium lead iodide ($CH_3NH_3PbI_3$), the large ionic sizes of lead and iodine ions allow significant spin–orbit coupling and thus decrease the energy band gap [50,51].

The electronic structure of metal-halide perovskites is also tuned by composition engineering [52,53]. The substitution of the halide anion with different atoms from Chlorine(Cl) to Bromine(Br) and Iodine(I), leads to a decrease in the energy band-gap from 3.1 eV to 1.9 eV [54]. Similarly, the substitution of the organic cation will generally shift the absorption onset energy downward, while increasing the cation size by tuning the metal-halide-metal angle [55]. However, reverse trends are also observed upon replacing the metal cation with a larger-size cation. The absorption onset shifts downward from 1.6 eV to 1.2 eV when the larger lead cation is replaced with a smaller Tin cation [56,57]. Consequently, the absorption and emission of perovskites can be well tuned from 400 nm towards 800 nm, which covers the entire visible wavelength range, making them available for a potential broadband optical application.

The knowledge of the complex refractive index (n, k) of an optical material is important for its use in optical devices. Especially the extinction coefficient, k, changes rapidly at the band edge. Murtaza and Ahmad reported by theoretical calculation that the refractive index (n) of $CsPbX_3$ perovskite increases, when substituting X from Cl to I anions, for photon energies in the visible and near infrared regimes [50]. Based on band structure calculations, we also expect a large tetragonal anisotropy in refractive index, with different components [58]. For I-based perovskites, z is the direction with larger reflectivity and absorption, while, for the Cl- or Br-based perovskites, the planar dimension prevails, consistent with the electronic properties.

2.1. Photon excited species in perovskites

When incident photons have an energy exceeding the band gap energy, excitons are generated in semiconductors at the initial stage. Coulomb correlations between electrons and holes affect the operation of optoelectronic devices since the resulting exciton has associated binding energy that needs to be overcome. In tetragonal phase organic–inorganic $CH_3NH_3PbI_3$ and $CH_3NH_3PbI_{3-x}Cl_x$ perovskites, diverse conclusions on the excitonic binding energy (reported in a range from few meV to $\sim$55 meV) have been obtained with various experimental techniques [59–68]. Furthermore, substitution of Cl- or Br-into I-based perovskite may result in a decrease in exciton binding energy. Compared with a standard semiconductor like CdS, in which the excitonic optical properties are dominant at room temperature (RT) with a ∼26 meV excitonic binding energy [69], interpretation of experiments with perovskites are more complex. From the experimental results, it is difficult to conclude that the primary photo-excited species in perovskites are excitons or free carriers at room temperature. Instead, it is more likely that in thermal equilibrium at room temperature, both coexist. The un-dissociated excitons belong to delocalized Wannier-type with reported Bohr radius (r_B) ∼30 Å [59,70].

Recently, there have been several reports on elucidating the photoexcited species and the dynamic behavior in $CH_3NH_3PbI_3$ and $CH_3NH_3PbI_{3-x}Cl_x$ perovskites with ultrafast spectroscopy approaches [71–79]. By using time-resolved microwave conductivity and THz spectroscopy measurements, free charge carriers are found to originate within a few ps upon following fs laser pulse excitation [71,72]. The standard Drude model shape of the photoinduced conductivity spectra further suggests that the primarily photo-excited species in these perovskites are free carriers [73,74]. With time-resolved THz, transient absorption and time-resolved photoluminescence measurements and decay modeling, the free electron and hole bimolecular recombination dominated dynamical behavior has been evidenced in a large range of photoexcited charge carrier concentration [64,73–78]. The results clearly suggest that the primary photoexcited species are free charge carriers inside the $CH_3NH_3PbI_3$ and $CH_3NH_3PbI_{3-x}Cl_x$ perovskites. These results also suggest that the exciton binding energy in these perovskites is much smaller than the room temperature thermal energy (26 meV).

In comparison to 3D ionic perovskites, stable excitons with large binding energies of hundreds of meV can be created in Ruddlesden–Popper 2D layered perovskites, due to the strong quantum and dielectric confinement [80]. This gives rise to intense photoluminescence with narrow peak width and high radiative recombination rate at RT, making them promising candidate materials for light emitter and laser applications.

2.2. Trap states dominated monomolecular decay at low pump fluence

Solutions-processed semiconductors tend to exhibit a large degree of electronic disorders and numerous bulk and surface traps. The $CH_3NH_3PbI_3$ and $CH_3NH_3PbI_{3-x}Cl_x$ perovskites are typically processed using solution methods and annealed under a temperature lower than 150 degree. However, they exhibit very limited trap state densities [77–79,81].

The trapping state density in solution-processed $CH_3NH_3PbI_3$ was first examined by Xing et al. using a pump fluence dependent PL method [79]. Following photo-excitation across the $CH_3NH_3PbI_3$ band-gap (at low pump fluence, where multiparticle recombination is not dominant), the excited charge carriers either relax through band-edge photon emission or trap-mediated non-radiative pathways. The former gives rise to spontaneous emission with lifetime (τ_0). An estimate of the bulk and surface trap densities can be made under these conditions, where trap state recombination is much slower than band edge radiative recombination. The photo-generated charge carrier density ($n_C(t)$) after photoexcitation can be described with the following set of differential equations:

$$dn_c(t)/dt = -\sum_i a_i n_c(t) n^i_{TP}(t) - (n_c(t)/\tau_0), \tag{1}$$

$$dn^i_{TP}(t)/dt = a_i n_c(t) n^i_{TP}(t), \tag{2}$$

where, $n^i_{TP}(t)$ is the i^{th} species trapping states density and a_i is the product of the trapping cross section and the carrier velocity. Therefore, the first term in Eq. (1) represents various trap-mediated non-radiative pathways, while the second term denotes the radiative recombination inside the film. Consequently, the relationship between the integrated band edge PL intensity ($I_{PL} = k\int_0^\infty n_c(t)/\tau_0 dt$, where k is a constant) and the initial photogenerated charge carrier density $n_c(0)$ is obtained from

$$n_c(0) = \sum_i n^i_{TP}(0)(1 - e^{-a_i\tau_0 I_{PL}/k}) + I_{PL}/k \tag{3}$$

Fitting the experimental result using Eq. (3) (Fig. 3) suggests two types of traps in $CH_3NH_3PbI_3$ thin films, with the bulk (surface/interfacial) traps exhibiting fast (slow) trapping times [79]. The bulk trap density is estimated to be $n^F_{TP} \sim 5 \times 10^{16} cm^{-3}$ while the surface/interfacial trap density is found to be $n^S_{TP} \sim 1.6 \times 10^{17} cm^{-3}$. This well correlates with a simple estimation of the total trap density (bulk and surface) obtained by the intersection of the linearly extrapolated PL intensity with that of the pump fluence axis (i.e., $n^0_{TP} \sim 2 \times 10^{17} cm^{-3}$). This intersection represents the pump fluence required to fill all the traps (*i.e.*, the threshold trap pump fluence P^{Trap}_{th}). The trap densities measured in $CH_3NH_3PbI_3$ are comparable to defect densities in highly ordered organic crystals (10^{15}-10^{18} cm^{-3}) [82] and superior to that of solution processed organic thin films (10^{19} cm^{-3}) [83]. Solution deposited, high-temperature annealed Cu-In-Ga-S/Se (CIGS) chalcogenide layers [84] also display comparable defect densities to that reported here (10^{16} cm^{-3}). These low bulk defect densities in perovskite are also consistent with the high solar cell efficiencies in this material.

For certain trap state concentrations, the photoexcited free electron and free hole decay in a semiconductor can be described by the following differential equation [73]

$$\frac{dn(t)}{dt} = -k_3 n^3 - k_2 n^2 - k_1 n, \tag{4}$$

where n is the photo-excited charge carrier density and t is time. k_1 is the monomolecular excitonic type recombination or trap states mediated recombination rate; k_2 is the free carrier bimolecular recombination rate; and k_3 is the three body Auger recombination rate.

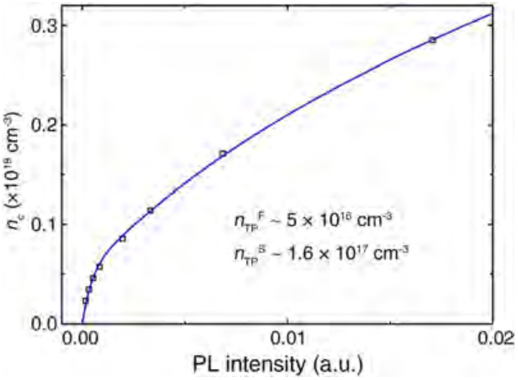

Fig. 3. Trap state density determination by PL intensity as a function of photon-generated exciton density in the low pump fluence range. The experimental data can be well-fit ($R^2 = 0.99$) using Eq. (3) with two types of trapping states [79]. Copyright 2014, Springer Nature.

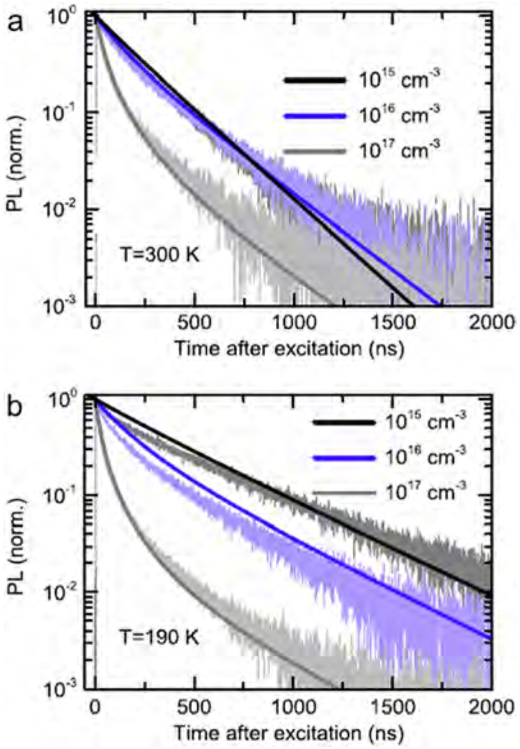

Fig. 4. PL decay at 780 nm from $CH_3NH_3PbI_{3-x}Cl_x$ perovskite at two temperatures (a) 300 K and (b) 190 K. The PL decay follows pulsed laser excitation (510 nm, 300 KHz) and variable laser fluence leading to different initial photoexcitation densities N(0). Solid lines are theoretical fits [78]. Copyright 2014, the American Physical Society.

At low pump fluence, the photoinduced minority carrier concentration is much smaller than the total majority carrier concentration (photoinduced + original doped). Under this condition the third term in Eq. (4) will be dominated, and the recombination of carriers is almost monomolecular. The shape of the decay curves for different experimental techniques (transient absorption (TA), time-resolved photoluminescence (TRPL), Time-resolved THz) should be mono-exponential under this situation. By fitting the decay curves with Eq. (4), the trap states density also can be extracted. With this method, a trap state density of 2.5×10^{16} cm^{-3} is obtained in solution processed $CH_3NH_3PbI_{3-x}Cl_x$ perovskite film at room temperature by Stranks et al. (Fig. 4) [78], which agrees well with the results obtained with the above mentioned pump fluence dependent state PL method [79].

The trap state density is strongly dependent on the sample procession conditions as well as on the surface treatment. Different trap densities result in different lifetimes observed for trap dominated monomolecular recombination at low pump fluence [77–79,81]. For example, the crystal surface under-coordinated Pb atoms could be electronically passivated by

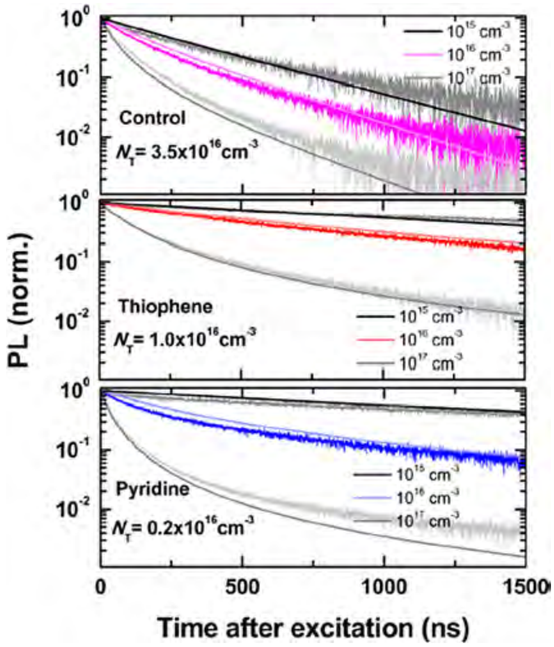

Fig. 5. PL decay at 780 nm from the $CH_3NH_3PbI_{3-x}Cl_x$ perovskite at temperatures (a) 300 K and (b) 190 K. Pulsed laser excitation (510 nm, 300 KHz) with different initial photoexcitation densities N(0) were used as in Fig. 5. Solid lines are theoretical fits [81]. Copyright 2014, the American Chemical Society.

exposing the surface to thiophene and pyridine molecules. As previously demonstrated by Noel et al. and shown in Fig. 5, the trap dominated single exponential PL lifetime in perovskites can be increased by over an order of magnitude; they observed lifetimes up to 2 μs [81]. Bastiani et al. demonstrated that even a substrate can greatly alter the crystallization of perovskites, resulting in different PL lifetimes observed for films spin-coated with the same solution [85]. Bass et al. investigated the influence of moisture on the crystal structure and photophysical properties of organohalide perovskites [86]. You et al. further reported observations that thermal annealing of the perovskite precursor film in a humid environment improves the film quality, grain size, carrier mobility, and lifetime [87].

2.3. Free electron–hole bimolecular recombination at higher pump fluence

At higher optical pump fluence, where the photo-generated charge carrier concentration is much higher than the trap states density inside the perovskites, free electron–hole recombination exhibits a bimolecular type characteristic response. The second term in Eq. (4) dominates over the third term and the charge carrier dynamics follows a power-law decay. The single exponential decay appears again when the charge carrier concentration drops below the trap states density.

A bio-molecular dynamical behavior of the photoexcited free charge carriers in $CH_3NH_3PbI_3$ and $CH_3NH_3PbI_{3-x}Cl_x$ perovskites was first described by Wehrenfenning et al. using time-resolved THz spectroscopy [73]. They observed that the perovskites possess large charge carrier mobilities ($11.6\ cm^2V^{-1}s^{-1}$ for $CH_3NH_3PbI_{3-x}Cl_x$ and $8\ cm^2V^{-1}s^{-1}$ for $CH_3NH_3PbI_3$) and slow bimolecular recombination rates ($8.7\times10^{-11}\ cm^3s^{-1}$ for $CH_3NH_3PbI_{3-x}Cl_x$ and $9.2\times10^{-10}\ cm^3s^{-1}$ for $CH_3NH_3PbI_3$), as shown in Fig. 6. They also found that the ratio of the bimolecular recombination constant to the charge carrier mobility (k_2/μ) in all these perovskites is nearly four orders of magnitude smaller than the value expected from the Langevin's theory, $e(\varepsilon_0\varepsilon_r)^{-1}$, where e is the elementary charge, ε_r is relative value of the dielectric function and ε_0 is the dielectric permittivity of free space. The Langevin theory predicts that the free electron and hole will recombine, once they collide within their capture radius [88]. Low charge recombination rate and high charge carrier mobility suggest that $CH_3NH_3PbI_3$ and $CH_3NH_3PbI_{3-x}Cl_x$ perovskites are particularly well-suited as light absorbers and charge transporters in photovoltaic cells.

A slow bimolecular dynamical behavior of the free charges in $CH_3NH_3PbI_3$ and $CH_3NH_3PbI_{3-x}Cl_x$ perovskites was subsequently confirmed by several other research groups [64,74–78]. Manser et al. reported a bimolecular recombination rate of $2.3\pm0.6\times10^{-9}\ cm^3s^{-1}$ for $CH_3NH_3PbI_3$ [75]. They observed the bimolecular recombination in the whole detection time window (∼1.5 ns) over a range of pump fluences (1–40 $\mu J/cm^2$). However, they did not observe any trap mediated monomolecular recombination at low pump fluence or at long decay time. Saba et al. experimentally observed and theoretically modeled electron–hole plasma bimolecular radiation recombination (rate $\sim2.6\times10^{-10}\ cm^3s^{-1}$) in $CH_3NH_3PbI_3$ and $CH_3NH_3PbI_{3-x}Cl_x$ perovskites (Fig. 7) [76]. A quadratic power dependence of the PL intensity at the initial time following above bandgap pulse photon excitation is clearly observed, which provides a direct evidence for a free electron–hole bimolecular recombination mechanism in these perovskites. They also found that electron–hole plasma radiative

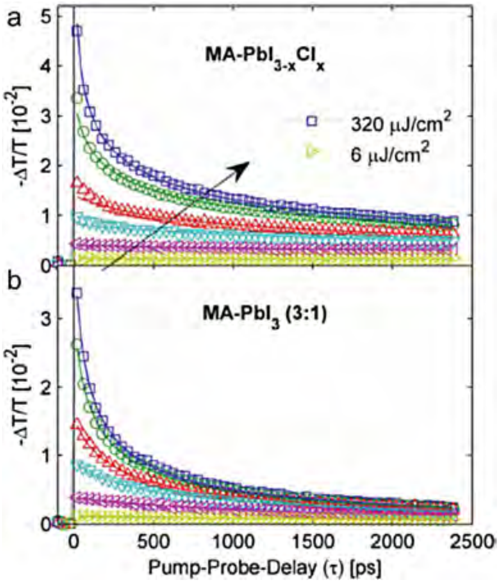

Fig. 6. THz photoinduced absorption transients: (a) $CH_3NH_3PbI_{3-x}Cl_x$ and (b) $CH_3NH_3PbI_3(3{:}1)$ after laser excitation at 550 nm for fluences between 6 μJ cm^{-2} and 320 μJ cm^{-2}. Solid lines are fits based on second- and third-order charge recombination as described in Eq. (4) [73]. Copyright 2014, Wiley.

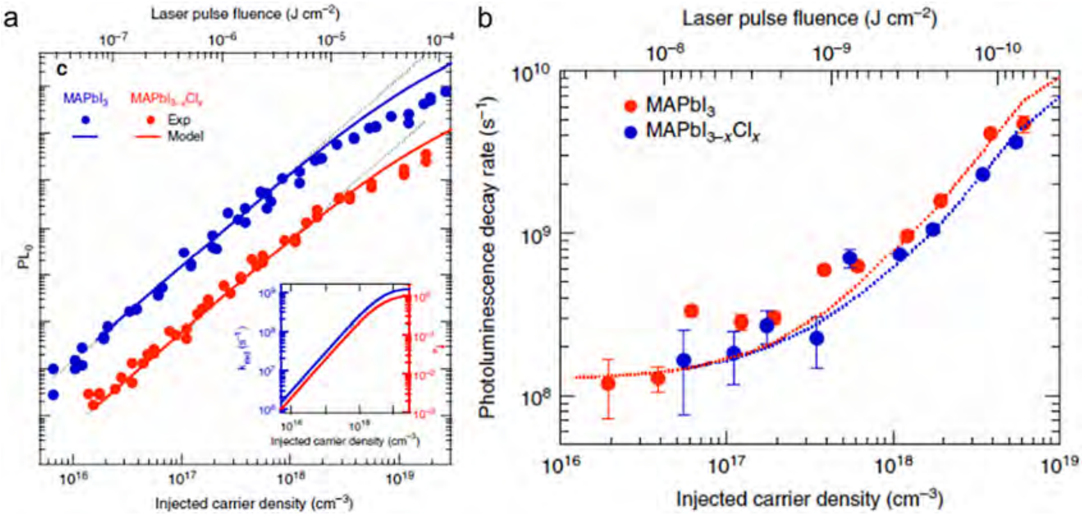

Fig. 7. (a) PL intensity estimated at $t = 0$ (PL_0) as a function of injected electron–hole density (lower axis) and laser pulse fluence (upper axis) from the TRPL measurements. The quadratic dependence is shown by the black-dotted lines as a guide for eyes. The solid lines are simulations according to Eq. (5). Inset shows the calculated spontaneous photon emission per electron–hole pair (k_{rad}, blue line) and occupation number of the lowest electron (hole) states in a non-interacting plasma based on Fermi–Dirac statistics ($f_{e(h)}$, red line). (b) The experimental (dots) and calculated (dotted lines) PL decay rate at the initial time [76]. Copyright 2014, Springer Nature.

recombination intensity and decay rate can be well reproduced with the Kubo–Martin–Schwinger relation [89,90]:

$$\mathrm{R}\,(\mathrm{n}) \approx \int_0^{\infty} \left(\frac{\omega n_r}{\pi c}\right)^2 \alpha_0\,(\omega)\, f_e\,(\omega)\, f_h\,(\omega)\, d\omega \tag{5}$$

where n_r is the refraction index, $g(\omega) = 1/(e^{\frac{\hbar\omega-\mu}{k_B T}} - 1)$ is the Bose function, μ is the chemical potential of the photoexcited electron–hole plasma, $\hbar$ is Planck's constant, k_B is Boltzmann's constant, T is the lattice temperature, ω_g is the band gap angular frequency, and c is the speed of light in vacuum. The right side of Eq. (5) neglects many-body interactions and bound-exciton states. It includes band filling effects through the product of the Fermi distributions of electrons and holes, $f_e(\omega)f_h(\omega)$.$\alpha_0(\omega)$ is the absorption coefficient of the continuum states for $n = 0$. The detailed experimental results and model results are shown in Fig. 7.

Applying the time-resolved microwave photoconductance method, Savenije et al. observed that the bimolecular recombination rate in $CH_3NH_3PbI_3$ increases from 2.0×10^{-10} cm^3s^{-1} to 13×10^{-10} cm^3s^{-1} when the temperature is increased from 165 K to 300 K [64]. They attributed this trend to temperature activated charge recombination processes. Yamada et al. reported a bimolecular recombination rate of 1.7×10^{-10} cm^3s^{-1} for $CH_3NH_3PbI_3$ with time-resolved photoluminescence (TRPL) and transient absorption (TA) methods [77].

2.4. *Charge carrier mobilities in perovskites*

A DC dark high charge carrier (electron) mobility ($\sim$66 $cm^2V^{-1}s^{-1}$) in $CH_3NH_3PbI_3$ was first reported by Stoumpos et al. with Hall-effect measurements [9]. The black, rhombic dodecahedral $CH_3NH_3PbI_3$ crystals were prepared with solution method. With the non-contact time-resolved THz spectroscopy method, Wehrenfennig et al. reported the lower bounds for the high-frequency charge effective mobility of 11.6 $cm^2V^{-1}s^{-1}$ for $CH_3NH_3PbI_{3-x}Cl_x$ and 8 $cm^2V^{-1}s^{-1}$ for $CH_3NH_3PbI_3$, and the perovskites were spin-coated on mesoporous Al_2O_3 [73]. With the same method, Ponseca et al. reported charge carrier effective mobility up to 25 $cm^2V^{-1}s^{-1}$ for the solution-processed $CH_3NH_3PbI_3$ on a Al_2O_3 scaffold [71]. By comparing the THz kinetics of $CH_3NH_3PbI_3$ on TiO_2 and with $CH_3NH_3PbI_3$ on Al_2O_3, they further claimed that they can estimate the ratio ($\sim$2) of the electron and hole mobilities. The same group (Savenije et al.) observed that charge carrier mobilities in $CH_3NH_3PbI_3/Al_2O_3$ decreases with increasing lattice temperature, following $T^{-1.6}$ dependence [64]. They attributed this to an increase in phonon scattering. However, a smaller charge carrier effective mobility of 6.2 $cm^2V^{-1}s^{-1}$ at 300 K is reported with the same technique. No explanation is given for the different observations from the same samples from the same group. With high quality vapor deposited $CH_3NH_3PbI_{3-x}Cl_x$film, Wehrenfennig et al. further reported that charge carrier mobilities $\geq$ 33 $cm^2V^{-1}s^{-1}$ could be achieved with these perovskites [74]. Recently, with time-resolved microwave conductivity measurements at 9 GHz, Oga et al. reported that the charge carrier mobilities increase with increasing the $CH_3NH_3PbI_3$crystal size [91]. However, by modulating the microwave frequency from 9 GHz to 23 GHz, they suggested that the intrinsic mobilities of the perovskites (up to 60–75 $cm^2V^{-1}s^{-1}$) could be obtained, which is independent of the mesoporous scaffold. In short conclusion, charge carrier mobilities $\geq$6 $cm^2V^{-1}s^{-1}$ have been reported for both $CH_3NH_3PbI_3$ and $CH_3NH_3PbI_{3-x}Cl_x$ perovskites. These values are remarkably high for solution-processed materials, and are even comparable with those of classical semiconductors such as Si, GaAs, *etc*.

2.5. *Electron–hole diffusion length in perovskites*

Low temperature solution processed semiconductors tend to have a large degree of electronic disorder and numerous defect states. Therefore, exciton or electron–hole diffusion lengths in these semiconductors are typically 10 nm. Decoupling light absorption and charge carrier transport is usually utilized to design high efficiency photovoltaic cells based on these semiconductors used as light absorber. The low temperature solution processed organic–inorganic halide perovskite materials appear to be opposite of this trend. Impressive efficiency values of up to 20% have been achieved with a variety of photovoltaic architectures [92–95]. Lee et al. have shown that high efficient solar cells based on $CH_3NH_3PbI_{3-x}Cl_x$ perovskite can be fabricated by replacing the mesoporous TiO_2 (electron collector) with an insulating Al_2O_3 scaffold [92]. This indicates that the perovskite is a good electron transporter. Etgar et al. demonstrated high efficiency solar cells based on these perovskites without an additional hole transporting layer [95].

It further suggests that these perovskites are also good hole transporters. Long range balanced electron–hole transporting in $CH_3NH_3PbI_3$ and $CH_3NH_3PbI_{3-x}Cl_x$ perovskites was firstly elucidated by Xing et al. [3] and Stranks et al. [13] at the same time, with the transient spectroscopy method. By selectively extracting photoinduced electrons or holes in $CH_3NH_3PbI_3$, Xing et al. revealed a clear evidence of balanced and long-range electron–hole diffusion lengths of at least 100 nm in this solution processed perovskite (Fig. 8). The same conclusion is further obtained by Stranks et al. with the same method [13]. Additionally, they reported that the electron–hole diffusion lengths in $CH_3NH_3PbI_{3-x}Cl_x$ are nearly one order of magnitude longer than that in $CH_3NH_3PbI_3$. The mechanism for the different diffusion lengths observed for these two kinds of perovskites was not clearly explained at that time. Later, it was found that the Cl^- incorporation could improve the crystallinity and homogeneity of the resultant perovskite film [96].

The charge carrier diffusion lengths in a semiconductor are strongly dependent on the charge recombination rates (trap states density and photo-generated charge carrier concentration) and charge carrier mobilities. Therefore, the crystallinity of perovskite absorber domains determines the diffusion lengths obtained. Liang et al. found that with the improved crystallinity and homogeneity of the perovskite thin film, the charge carrier diffusion length can be increased from $\sim$160 nm in $CH_3NH_3Pb(I_{1-Y}Br_Y)_3$ to $\sim$800 nm in $CH_3NH_3Pb(I_{1-Y}Br_Y)_XCl_{3-X}$ [97]. Bai et al. reported that longer charge carrier diffusion lengths can be obtained with optimized film processing conditions and procedures [98]. In another type of organic–inorganic $HC(NH_2)_2PbI_3$ perovskite (where the methylammonium cation is replaced by the larger FA cation), long but unbalanced charge carrier diffusion lengths (L_e $\sim$177 nm, L_h $\sim$813 nm) were reported by Eperon et al. with the TRPL method [5]. However, power conversion efficiency up to 14.2% was still achieved by fabricating a planar architecture solar cell with this type perovskite, according to their report. Here, we emphasize that as the primary photogenerated species in $CH_3NH_3PbI_3$ and $CH_3NH_3PbI_{3-x}Cl_x$ perovskites are free electrons and holes, the charge carrier dynamics is dominated by trap related monomolecular recombination at low pump fluence (lifetime is independent of photogenerated charge carrier concentration). The dynamics is dominated by free electron–hole bimolecular recombination as well as three-particle Auger

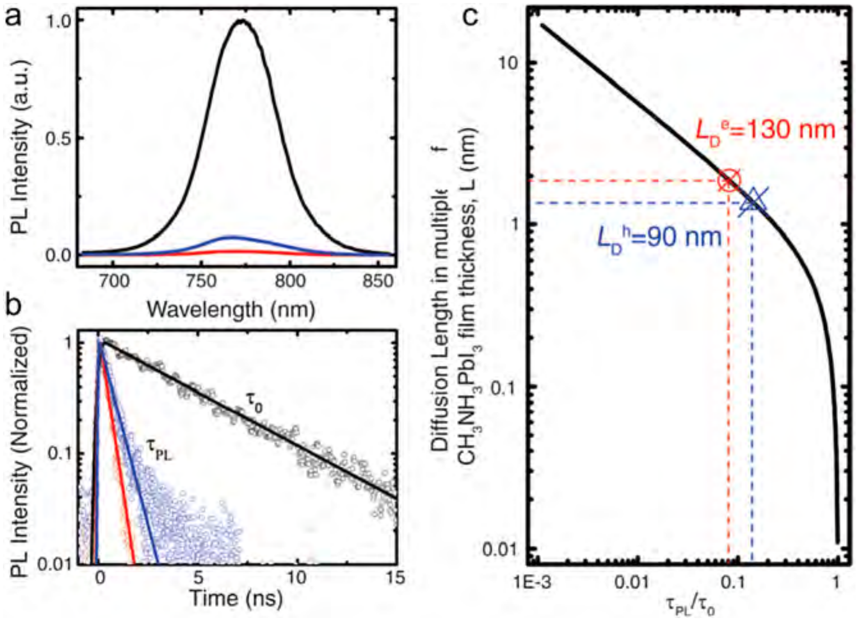

Fig. 8. (a) Time-integrated PL spectra and (b) Time-resolved PL decay transients measured at 760 ± 10 nm for quartz/$CH_3NH_3PbI_3$ (65 nm) (black), quartz/$CH_3NH_3PbI_3$ (65 nm)/PCBM (red), quartz/$CH_3NH_3PbI_3$ (65 nm)/Spiro-OMeTAD (blue) films in vacuum after excitation at 600 nm (1 KHz, 150 fs, 1.3 $\mu J/cm^2$). The solid lines in (b) are the single-exponential fits of the PL decay transients. a.u., arbitrary units. (c) A plot of exciton diffusion length versus PL lifetime quenching ratios. Diffusion length is scaled in multiples of $CH_3NH_3PbI_3$ layer thickness ($L = 65$ nm) [3]. Copyright 2013, AAAS.

recombination at higher pump fluence (contrarily, lifetime is strongly dependent on the photogenerated charge carrier concentration). Therefore, the charge carrier diffusion length will be greatly shortened at higher pump fluence (bimolecular dominated) by the increased recombination rate. The diffusion length extracted under the solar illumination condition (trap dominated charge carrier recombination regime) is of more broad interest.

The electron–hole diffusion length determined by the simple selective charge carrier extracting method, is strongly affected by the perovskites domain boundary, charge carrier transfer time and efficiency across the interface. The diffusion length determined with this simple method, is directly linked with the overall solar cell performance. More intrinsic bulk perovskites related charge carrier diffusion lengths can be extracted by measuring the local charge carrier mobilities and lifetimes in single layer perovskite film with time-resolved microwave or THz spectroscopy [71,73,74]. With these techniques, the electron–hole diffusion lengths up to few micrometers have been reported by Wehrenfennig et al. [73,74] and Ponseca et al. [71] for both the $CH_3NH_3PbI_3$ and $CH_3NH_3PbI_{3-x}Cl_x$ perovskites. In general, long range charge carrier diffusion lengths have been observed for low-temperature solution-processed organic–inorganic lead halide perovskites. The traditional short charge carrier diffusion length constraint for the solution-processed photovoltaic semiconductors is transcended with these perovskites.

In summary, perovskite chemical composition can be tailored to yield high optical absorption coefficient, low non-radiative recombination rate, long carrier diffusion lengths, high photoluminescence quantum yield, and broadly tunable optical properties, for intriguing potential in optoelectronic and photonic applications. Nanostructures of perovskites could offer added unique opportunities due to the controllability over dimensionality, size, architecture, composition, and surface functionalization. Moreover, nanostructured hybrid perovskite media and their optical cavities provide a feasible strategy to tune the optical properties of perovskites including their excitation dynamics and to realize enhanced light–matter interactions towards various optoelectronic and photonic applications.

3. Optical properties of metal-halide perovskites cavities and their hybrid platforms

Optical cavities confine light within a small volume by resonant recycling. Metal-halide perovskite devices based on cavities have become indispensable for various applications and explorations. In metal-halide perovskite devices, cavities produce perovskite materials emitting spontaneous emission in a desired direction, or they can provide an environment where dissipative mechanisms, such as spontaneous emission, are overcome such that quantum entanglement between radiation and matter becomes possible. The applications of these excellent devices are as diverse as their geometric and cavity resonant characteristics.

Through different manufacturing processes, perovskite nanostructures can be integrated into diverse applications with different compositions, crystal structures, and morphologies. Perovskite single crystals have uniform shape, smooth surfaces,

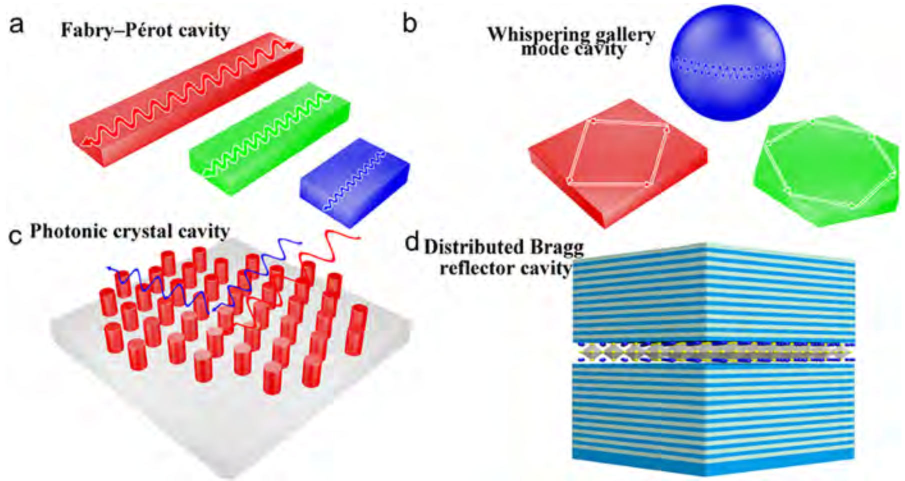

Fig. 9. Schematics of different types of perovskite cavities (a) F–P cavity; (b) Whispering gallery mode (WGM) cavity; (c) Photonic crystal cavity; (d) Distributed Bragg reflector (DBR) cavity.

and specific crystal orientation. The smooth crystal planes can be developed as mirrors so that a perovskite crystal itself functions as a gain medium; it is also beneficial for coupling perovskite crystals to other optical devices. Schematics of the different types of photonic cavities used for perovskites are shown in Fig. 9. In addition, perovskite nanoparticles exhibited enhanced PL due to intrinsic Mie resonances, suggesting that one can expect interference between exciton and Mie resonances even in an isolated perovskite nanoparticle [99,100].

The important parameter of a cavity is its quality factor (Q value), which is defined as follows [101]:

$$Q = \omega \frac{U}{R_l} = \omega\tau, \tag{6}$$

where, ω is the modal frequency, U is the light field energy in the cavity, and R_l is the energy loss rate. The energy in the cavity changes with the time in the form $U(t) = U(0)e^{-t/\tau}$, where τ is the average photon lifetime. A higher Q value corresponds to a longer photon lifetime, resulting in a strong interaction between the bound light field and matter. From the above equation, the Q value of a micro-cavity mode is inversely proportional to the energy loss, and the total intrinsic loss is primarily composed of different physical mechanisms including: radiation, absorption and scattering losses.

$$\frac{1}{Q_{int}} = \frac{1}{Q_{rad}} + \frac{1}{Q_{abs}} + \frac{1}{Q_{sca}} \tag{7}$$

The radiation loss, Q_{rad}, is derived from the fact that light has a certain tunneling probability, when it is totally reflected from a curved surface, which is analogous to loss from the surface of a curved waveguide. The absorption loss, Q_{abs}, is derived from absorption of electromagnetic waves by the dielectric material constituting the micro-cavity, and its surrounding environment. The scattering loss, Q_{sca}, is derived from uneven undulations on the surface of the microcavity and defects inside the medium, which will scatter light. This loss can be found in many optical materials and micro-cavities. By improving the processing technology, scattering losses from micro-cavities can be reduced. In addition, the surface roughness scattering loss can be reduced by surface reprocessing [102].

3.1. *Fabry–Pérot cavities*

Perovskite structures like nanorods and nanowires, have been shown to act as excellent Fabry–Pérot (F–P) cavities. Due to their ultra-small physical size, highly localized coherent output, and efficient wave guiding capabilities, perovskite nanowires are expected to be used for fully integrated nanoscale photonic and optoelectronic devices. Perovskite nanowires can effectively overcome one of the major obstacles of traditional semiconductor nanowire lasers, namely the high threshold carrier density. Such superior performance is attributed to their long carrier lifetime and low non-radiative recombination rates [29]. Therefore, it is expected that perovskite nanolasers exhibit more interesting features than corresponding lasers made from bulk materials or other semiconductors, by integrating the various advantages of perovskites and one-dimensional materials. The mode spacing $\Delta\lambda$ and the cavity length L are related by the equation:

$$\Delta\lambda = \frac{\lambda^2}{2L\left[n - \lambda(dn/d\lambda)\right]} \tag{8}$$

where λ is the resonant mode wavelength, n is the refractive index, and $n - \lambda(dn/d\lambda)$ is the group refractive index [103,104]. As shown in Fig. 9, the smooth facets on perovskites NWs with triangular or rectangular cross-section, reflect photons like mirrors. Light travels along the long axis of the nanowires, reflects, and oscillates between the 'mirrors' on the two end-facets of the nanowire. Certain wavelengths of light in an F–P nanowire cavity in nanowires lead to resonance [105,106]. Due to the high effective refractive index of perovskites, a light field can be firmly confined and low-loss guided along the length of the NWs with low loss. Consequently, various resonance modes can be realized by controlling the length, composition and cross-section of perovskite nanowires.

The Q factor of a F–P cavity can be calculated using the following equation [107,108]

$$Q = \frac{2\pi nL}{\lambda(1-R)}, \tag{9}$$

where n is the refractive index, R is the reflectivity at the perovskites/air boundary, and L is the cavity length.

A cube-corner pyramid F–P cavity has three surfaces that act as mirrors and can function as miniature retroreflectors. Therefore, a cube-corner pyramid perovskite F–P cavity can reflect light parallel to the input light, and is widely used in many applications such as laser resonators, long-path interferometry, and ranging [108].

Zhu et al. prepared a series of high-quality $MAPbX_3$ perovskite-NWs as F–P cavities using a surface-initiated solution growth strategy [29]. The method involves contacting a solid film of lead acetate deposited on a glass substrate with a high concentration of MAX in an isopropyl alcohol solution at room temperature. The single-crystal $MAPbX_3$ perovskite-NW F–P cavity exhibits room-temperature and broad wavelength-tunable lasing covering the near-infrared to visible wavelength region, with a very low lasing threshold and a high-quality factor. These excellent properties have been shown to originate from rectangular cross-section perovskite NWs with long carrier lifetimes and low non-radiative recombination rates. Fu et al. reported using a similar method to synthesize a series of $FAPbX_3$-based single crystal nanowire F–P cavities in a low temperature solution [109]. The room temperature near-infrared lasing exhibits long-lasting laser emission over 10^8 excitation cycles, thus solving the optical and thermal stability problems in perovskite NW F–P cavities. These results suggest that formamidinium lead halide perovskite nanostructures could become more promising and stable materials for the development of light-emitting diodes and continuous-wave lasers. Furthermore, Eaton et al. reported the growth of a high-stability cesium lead halide nanowire as an F–P cavity laser with low-threshold at low temperatures by using the same solution method [110]. The as-grown nanowires are single crystals that exhibit excellent stability when stored and used in ambient conditions over several weeks. With constant illumination, emission can be maintained for more than 1 h (equivalent to 10^9 excitation cycles), while the performance is still reliable in ambient condition.

In order to reduce the influence of chemical solvent residues and further improve the aspect ratio of F–P cavities, chemical vapor-phase deposition has become more advantageous than the solution method. Xing et al. reported the synthesis of $CH_3NH_3PbI_3$ nanowire F–P cavities with high crystalline quality, rectangular cross-section, and lengths of up to 20 μm by using PbI_2 and CH_3NH_3I as precursors through a two-step gas-phase method [111]. It has been reported that F–P cavities with a triangular cross section exhibit a uniform high Q factor over a wide spectral range compared to other shapes, thus one-dimensional nanostructures with a triangular cross section are more suitable for tunable laser applications [112]. Zhou et al. reported the synthesis of high-quality, all-inorganic cesium lead halide alloy perovskite micro/nanorods by vapor deposition, with the ability to completely control their composition [113]. The as-grown micro/nanorods are found to be single crystals, with triangular cross-section which can act as efficient F–P cavities for nanoscale lasers. Chemical vapor deposition can also be used to prepare special cube-corner pyramid F–P cavities. High quality $CH_3NH_3PbBr_3$ single crystals with uniquely shaped cube-corner pyramids on mica substrates have been fabricated. These microscopic pyramids naturally form cube-corner cavities and are considered as candidates for small resonators and reflectors. Through a special F–P cavity mechanism, the perovskite pyramid shows strong emission in the vertical direction at room temperature [114].

Unlike the single perovskite F–P cavity, a high-quality F–P cavity array may become more suitable for low-cost, large-area optoelectronic applications. Using a combination of micro/nanofabrication techniques such as capillary-bridge lithography and template methods, uniform-shape F–P cavity arrays can be fabricated from both solution and etching methods, which will have important significance for manufacturing large-area, high-power laser sources [115,116].

3.2. *Whispering-gallery-mode cavities*

For hexagonal perovskites cavities, the situation becomes more complicated, as shown in Fig. 10, where three different total reflection scenarios are illustrated. A F–P cavity is usually converted to a WGM cavity, when the common perovskite F–P cavity aspect ratio is gradually reduced, *i.e.*, as the nanowires or nanorods are converted into nanoplatelets or plates [104]. In addition to the geometry of a F–P cavity, polygonal sheets, discs, or spheres are also fundamentally interesting, given that they naturally form a WGM cavities (Fig. 9b) and provide total internal reflection, resulting in excellent light confinement. In a WGM cavity, light can be captured in a sphere or ring of gain material with a higher index of refraction than the surrounding environment, providing a higher cavity quality factor (Q) than a F–P cavity.

Considering the case of a WGM, the Q factor for an m-faceted polygonal cavity can be expressed as [117,118]:

$$Q = \frac{\pi DmnR^{\frac{m}{4}}}{2\lambda(1-R^{\frac{m}{2}})} sin\frac{2\pi}{m}, \tag{10}$$

where D is the diameter of the circle circumscribing polygon, m is the number of facets of the polygon, and R is the reflectivity of the facets. Taking into account the cavity loss at corners, this result is valid for total internal reflection. In fact, for a WGM

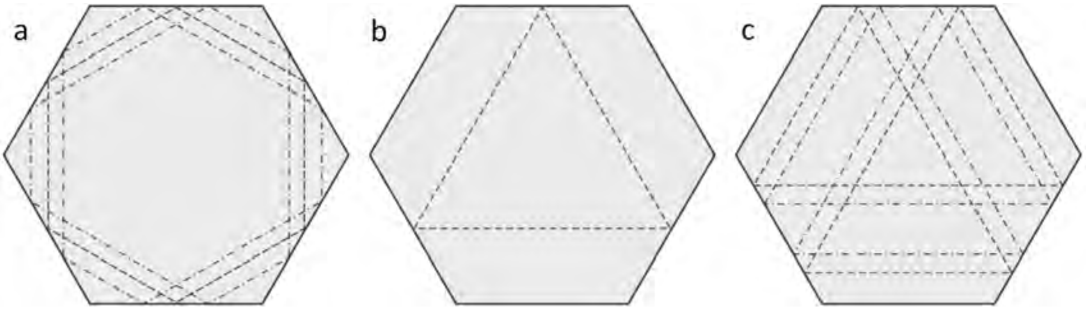

Fig. 10. Schematic geometry of rays with a closed path in a uniform hexagonal cavity (gray area). (a) Hexagonal mode (6-WGM); the symmetric mode is shown with dashed line and two non-symmetric modes with dash-dotted lines. (b) Triangular mode (3-WGM, dashed line). (c) Two different double-triangular modes (D3-WGM) shown by dashed and dash-dotted lines [120]. Copyright 2012, Wiley.

cavity, light does not have to be centered between the two corners (see Fig. 9c [119]). This is why a light field is strongly distributed in the corners of the hexagonal disk, but the intensity is very low at the center of the disk. It is also worth noting that the WGM cavities are more preferable due to their better optical constraints.

The mode spacing, $\Delta\lambda$, is also an important parameter in these cavities. In order to form a stable oscillation in the cavity and enhance the intensity due to constructive interference, the phase change of reciprocating light in the perovskite cavity should be an integral multiple of 2π, *i.e.*, the resonance condition is:

$$nL = m\lambda, \tag{11}$$

where n is the phase index, L is round trip distance in the perovskite cavity, and m is the mode order (integer). Certain frequencies are limited by the resonance conditions, and are finally enhanced only by the perovskite cavity. The spectral spacing, $\Delta\lambda$, between the adjacent laser modes is given by the following relationship:

$$\Delta\lambda = \frac{\lambda^2}{n_g L}, \tag{12}$$

where, n_g is the group refractive index, expressed as follows:

$$n_g = \mathrm{n}\left(1 - \frac{\lambda \mathrm{dn}}{\mathrm{n} \mathrm{d}\lambda}\right). \tag{13}$$

In circular discs or spheres, where a fundamental WGM mode is located near the rim of the cavity, *i.e.*, $\mathrm{L} \approx 2\pi \mathrm{R}$ is used as an approximation. Then

$$\Delta\lambda = \frac{\lambda^2}{\pi n_g R}, \tag{14}$$

where R is the radius of cavity [102].

For a cubic WGM cavity, the mode spacing $\Delta\lambda$ can be expressed as:

$$\Delta\lambda = \frac{\lambda^2}{2\sqrt{2} L n_g}, \tag{15}$$

where in this instance L is the side length of the cube, and n_g is the group refractive index as a function of wavelength, which further verifies a four-edge reflected WGM lasing mechanism.

For higher order modes and for a simplified theoretical treatment, a constructive interference between planar waves and ray optics are often invoked. First, true hexagonal WGMs (6-WGM, Fig. 10a) modes exist. The symmetric mode is shown in Fig. 10a as a dashed line, two other 6-WGMs are shown as dash-dotted lines. All 6-WGMs have six reflections, and the same path length ($\mathrm{L} = 3\sqrt{3}R$, where, R is the side length of the hexagonal cavity), and we further note that a 6-WGM exists for all ray positions on the facets. The mode spacing $\Delta\lambda$ for the 6-WGM cavity can be expressed as:

$$\Delta\lambda = \frac{\lambda^2}{3\sqrt{3} R n_g}. \tag{16}$$

Triangular WG modes (3-WGM, Fig. 10b) have been discussed and have been termed "quasi-WGM". This mode has three reflections and a path length of $\mathrm{L} = \frac{9}{2}R$. The mode spacing $\Delta\lambda$ for the 3-WGMcavity can be expressed as:

$$\Delta\lambda = \frac{2\lambda^2}{9 R n_g}. \tag{17}$$

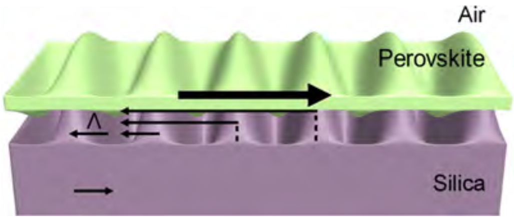

Fig. 11. Schematic structure of a perovskite DFB laser with corrugations of period Λ. Light of wavelength $\lambda=2n_{eff}\Lambda$ propagating from left to right is scattered from the periodic structure to create a diffracted wave propagating in the counter propagating waveguide mode.

As can be seen in Fig. 10c, double-triangular modes (D3-WGM) have a closed path. The 3-WGM is a special case of the D3-WGM when the beam is incident exactly at the center of the facet. While there is only a single 3-WGM, a D3-WGM exists for all ray positions on the facet, similar to the 6-WGM. Therefore, we consider these modes to be similarly important [120].

3.3. 2D Photonic-crystal cavities

Perovskite nanostructures can also serve as a gain medium, and can be integrated with other passive optical cavity geometries, thus forming lasers [121] (Fig. 9c, 9d). A photonic crystal cavity is an alternative approach to integrate a periodic dielectric nanostructure and yield a high-performance laser that is different from Bragg reflector cavities. A mature research and experience on assembling epitaxial III–V photonic crystal diode lasers like GaN and InAsP/SiO_2 quantum wells have paved the way for fabricating similar devices in other systems [122–124]. Chen et al. first embedded solution processed $CH_3NH_3PbI_3$ thin-films into a two-dimensional photonic crystal structure [36]. A high degree of temporally and spatially coherent lasing with well-defined directional emission is achieved at a low optical pumping fluence threshold of 68.5 ±3.0 $\mu J/cm^2$. The photonic crystal cavities are integrated with different dimensional active layer perovskites in various reports, Xing et al. demonstrated lasing by infiltrating a naturally occurring photonic crystal shaped like butterfly wings [125]. More recently, Tuysuz and co-workers assembled a 3D organometallic halide perovskite photonic crystal coupled with a distributed feedback (DFB) laser, where a strong and adjustable photonic band gap effect was observed [126]. From the perspectives of cavity geometry, these photonic crystals based micro-resonators do not use mirrors, nor do they require total internal reflection for feedback. Instead, they apply periodic, wavelength-scale structures that diffract or Bragg–scatter light. These periodic structures can be readily incorporated into planar semiconductor waveguides (as shown in Fig. 11), and do not require better-quality end facets to provide feedback. By imposing a periodic surface corrugation on an organic semiconductor film, one may create a structure that can reflect propagating waveguide modes by a distributed scattering mechanism that obviates the need for end facets.

Fig. 11 shows a typical DFB laser fabricated using a corrugated perovskite waveguide, the diffractive feedback of the DFB design creates band edge resonances that confine the electromagnetic field analogous to a F–P cavity [127]. The laser is fabricated using a thin perovskite film deposited on top of a corrugated fused silica substrate. Light propagating in the waveguide mode of the high-index film is scattered by the periodic corrugations. For a corrugation period, there is a set of discrete wavelengths that will be diffracted from a propagating waveguide mode into the counter-propagating waveguide mode. This situation will arise when the Bragg condition is satisfied:

$$m\lambda = 2n_{eff}\Lambda \ . \tag{18}$$

Here, λ is the wavelength of the light, Λ is the period of the DFB structure, and m is an integer that represents the diffraction order. n_{eff} is the effective refractive index of the waveguide; this is a geometric weighted average of the refractive indices of the three waveguide layers and may be calculated from a solution to the Helmholtz wave equation for a planar multilayer structure. Recently, Jia et al. demonstrated $MAPbI_3$ DFB lasers that operate CW above optical pumping thresholds of ~17 Kw cm^{-2} and at temperatures below the tetragonal-to-orthorhombic phase transition (T<160 K) [128]. Continuous gain originates from tetragonal-phase inclusions that are photogenerated by the pump within the bulk orthorhombic host matrix on a sub-microsecond timescale. The results suggested a general strategy to design perovskite gain media for CW lasing.

Referring to the perovskite gain media embedded in photonic crystal cavities, intensive research has been published for a 2D triangular lattice photonic crystal structure. It provides an in-plane distributed optical feedback mechanism, while, in principle, capable of enhancing the light–matter interaction [129,130]. The lattice-periodic change in the refractive index creates a photonic band structure, which in a laser is exploited by matching the band edge resonance wavelength of the photonic crystal to the gain spectrum of the active medium. The geometric factors are determined by the lattice symmetry and the strength of the feedback is determined by the relative refractive index between the active layer and the substrate. As an example, consider the classic combination of $MAPbI_3$on a quartz substrate, the high refractive index of the perovskite (n~2.7) compared to a quartz substrate (n~1.5) increases the resonator mode spacing at the high symmetry K-points of the photonic crystal (PhC) reciprocal lattice, thereby offering a further benefit to single mode lasing operation.

3.4. Distributed-Bragg reflector (DBR) cavities

A Distributed Bragg reflector (DBR) cavity is also a one typical mirror configuration used in vertical-cavity surface-emitting lasers, where a laser resonator is made with at least one DBR outside the gain medium (shown as Fig. 9d). A Bragg mirror is a light-reflecting device based on Bragg reflection. In most cases, a quarter-wave mirror provides the maximum amount of reflection for a given number of layers. A significant feature of the DBR laser configuration, compared to the aforementioned photonic crystal cavity-based DFB lasers, is that the entire active medium is embedded in a single distributed reflector structure.

Symmetric structures with low-loss dielectric Bragg reflecting mirrors on both sides of a polymer film have also been studied. Such structures have been demonstrated by sandwiching together two polymer-coated mirrors. More recently, structures in which the top dielectric Bragg mirror is directly deposited on the organic semiconductor have been demonstrated. Such lasing structures are comparable to the inorganic semiconducting vertical cavity surface emitting lasers (VCSELs) that have been widely studied and have low oscillation threshold combined with low-divergence surface emission. A variant of such lasers is the vertical external cavity surface emitting lasers (VECSELs) in which one of the mirrors is in direct contact with the gain material and the second curved "external" mirror is spaced a small distance from the gain medium. Such structures have definitively shown the impact of the resonator on the polymer laser emission and hence clearly confirmed the resonant nature of the lasing.

Friend's group firstly reported the photophysical properties of an organic—metallic lead halide perovskite vertical cavity optical DBR structure in which a perovskite film is sandwiched between a gold mirror and dielectric stack mirror, as shown in Fig. 12a [131]. A high luminescence efficiency is observed in this structure (Fig. 12b). Su et al. observed direct evidence for polariton condensation and lasing in an all-inorganic $CsPbCl_3$perovskite planar microcavity at room temperature. It exhibits polariton lasing within a low Q-factor microcavity (∼300) [34]. An improved polycrystalline perovskite ($FAPbBr_3$) VCSEL device with a planar sputtered DBR was reported recently, where the stacked structure forms a high-Q cavity that enables low threshold lasing (Fig. 12c) [132]. These DBR cavity devices open a new platform for large area, low cost, and high-performance lasing devices, and they exhibit a strong potential to realize a perovskite based coherent light source at room temperature in the future.

Recently, Gharajeh et al. reported a directly patterned perovskite DFB resonator in which narrow amplified spontaneous emission (ASE) at pump powers as low as 0.1 W/cm^2 were demonstrated under continuous-wave (CW) optical pumping conditions at room temperature [133]. They used thermal nanoimprint lithography to produce direct nanostructuring of perovskites and observed a 16-fold reduction in emission linewidth in the $MAPbI_3$ DFB cavity, compared to the pristine thin film photoluminescence spectrum.

4. Metal-halide perovskites with coupled plasmonic cavities

This section describes the effects which can manifest to impact on the device performance of an optical medium comprised of perovskites coupled to a metallic nanostructure plasmonic cavity. For the sake of clarity, we first introduce basic concepts on optical excitations in metals and their nanostructures as well as on interactions, energy transfer and charge transfer processes in semiconductors couple with a plasmonic cavity. Much of this area is still relatively unexplored in relation to perovskites.

4.1. Plasmonic optical resonances in metals

In order to describe the conductivity and optical response of electrons in a metal simultaneously, the Drude model has been used. The Drude model is based on the following premise: (1) a set of valence electrons occupy delocalized states and are spread over the entire lattice, and do not interact with one another due to the ion screening (free electron approximation); (2) electrons weakly interact with the lattice and external fields, which are sources of radiation reaction forces leading to damping [134,135]; (3) the damping is described by a probability rate of an electron damping coefficient γ, where γ is also called the relaxation time, or the scattering frequency; the electron damping drives it toward thermal equilibrium with the lattice.

In the Drude model, dielectric constant is given as

$$\varepsilon\left(\omega\right)=\varepsilon_0-\frac{n_0e^2}{m}\frac{1}{\omega^2+i\gamma\omega}=\varepsilon_0(1-\frac{\omega_p^2}{\omega^2+i\gamma\omega}), \tag{19}$$

and,

$$\omega_p=\sqrt{\frac{\mathrm{n_0e^2}}{\mathrm{m}\varepsilon_0}}, \tag{20}$$

is also called the plasma frequency, which is a measure of the electron density. When $\omega=\omega_\mathrm{p}$, $\mathrm{Re}(\varepsilon(\omega))=0$; this is the bulk plasmon resonance condition to be discussed later. If we ignore the damping term due to electron collisions, the Drude model becomes a free electron model and the dielectric constant is

$$\varepsilon\left(\omega\right)=\varepsilon_0\left(1-\frac{\omega_p^2}{\omega^2}\right). \tag{21}$$

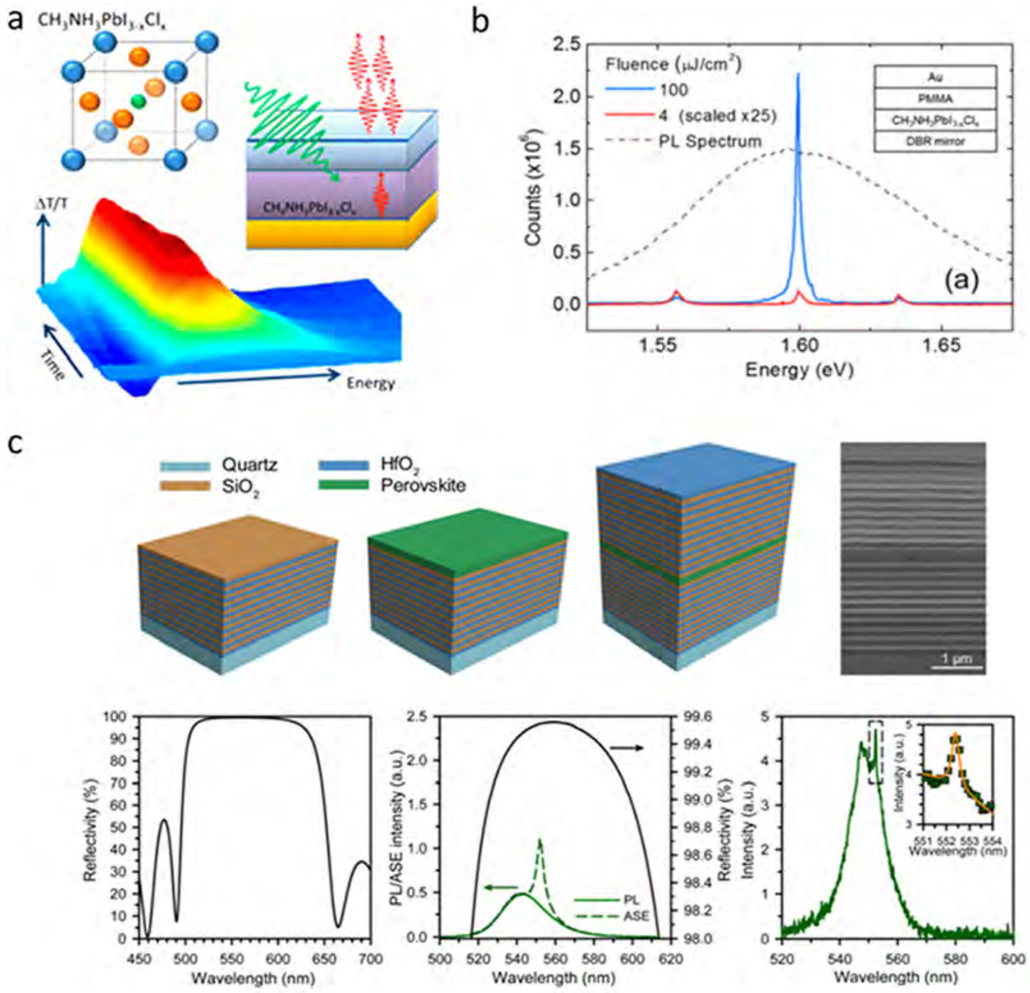

Fig. 12. (a) Schematics of $CH_3NH_3PbI_xCl_{3-x}$vertical microcavity structure [131]. Copyright 2014, the American Chemical Society. (b) Emission spectrum of a vertical microcavity with the structure as shown in the inset using a perovskite film as the gain medium. The thickness of the perovskite layer was around 500 nm, and the PMMA layer thickness is 1 μm [131]. Copyright 2014, the American Chemical Society. (c) Vertical cavity with HfO_2/SiO_2 dielectric DBR mirrors [132]. Copyright 2017, the American Chemical Society.

It should be pointed out that the Drude model only considers contributions from valence electrons. The bound valence electrons can also be polarized under the action of electromagnetic or external electric fields [135,136]. The bound valence electrons contribution to the dielectric constant will create deviation from the local Drude model [21]. If we ignore their frequency dependence for a moment their contribution can be approximated as

$$\varepsilon\left(\omega\right)=\varepsilon_0(\varepsilon_\infty-\frac{\omega_p^2}{\omega^2+i\gamma\omega}). \tag{22}$$

ε_∞ is the contribution to the dielectric function from bound valence electrons. It is noted that across the entire wavelength region, there are bound valence electron contributions to the dielectric function. In the short-wave region, additional inter-band transitions in the metal can also be excited by light, leading to significant changes in the dielectric function. For example, light with a wavelength below about 500 nm stimulates 3d to 4s band transitions in gold. Thus, gold will have a significant increase in absorption as the wavelength crosses this region.

Due to the delocalized nature of free valence electrons and the long-range nature of the Coulomb interaction, the free electrons can be treated like a fluid with additional terms derived from a hydrodynamic model [21]. The linearized hydrodynamic model introduces a nonlocal term in the dielectric function expressed in angular frequency and wave vector space, which is approximated as

$$\varepsilon\left(\omega\right)=\varepsilon_0(\varepsilon_\infty-\frac{\omega_p^2}{\omega^2+i\gamma\omega-|\mathbf{k}|^2\beta^2}). \tag{23}$$

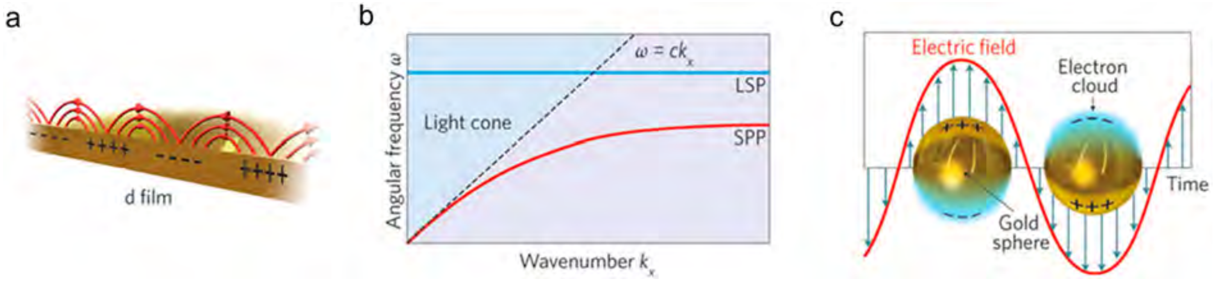

Fig. 13. Illustration of surface plasmon polaritons (SPPs) and localized surface plasmons (LSPs), together with their associated dispersion diagrams. (a) Collective oscillation of electron excess density with the incident electromagnetic E field at a flat gold–air interface, called SPP. (b) Typical dispersion curves of SPPs (red) and LSPs (blue). The light cone is bounded by the vacuum dispersion curve (dotted line). (c) Collective oscillation of electrons with the incident electromagnetic field in a gold nanoparticle. The LSP dispersion is independent of the wave vector, as shown in (b) [151]. Copyright 2016, the American Chemical Society.

where β is proportional to the Fermi velocity v_F, which is directly related to the electron pressure contribution. For noble metals, $v_F \sim 10^{-2}c$, which sets the size of the nonlocal contribution. The nonlocal contribution is generally small; an exception is in situations where the metals have nanoscale sizes which changes the electron density at metal surfaces. It can become especially relevant at metal surfaces where handling this term leads to the issue of additional boundary conditions. This expression reduces to the local form of the Drude model when $\beta = 0$.

Nonlocal contributions are especially significant in limiting the field enhancement [137–142]. Additional nanoscale quantum electron effects are due to electron spill out into the insulator film at a metal/insulator interface.

Models incorporate quantum aspects of the metal (*e.g.*, gold) film interface from the atomic scale have been applied to nanoscale structures in the past few years [143,144]. The models are built into simulations that help understand the role of quantum effects in nonlinear optical experiments. Gold is characterized by a nearly-free, s-shell electron that extends to an approximate distance r_s ~1.5 Å from the nucleus, and d-shell electrons whose orbits extend out approximately r_d ~0.5 Å from the nucleus [145]. The simple atomic scale picture that emerges from even a cursory look at atomic surface is one of a negatively charged electron cloud that spills outside the ionic surface and screens the inside portions of the metal [141]. Upon further inspection, it becomes obvious that the interior sections of the medium contain a combination of free and bound charges, whose dynamical properties are represented by Lorentz oscillators [146].

Furthermore, any external perturbation in the electron density in the microscopic interior of the metal will inevitably cause correlation between electronic motion throughout the system. This results in the formation of a collective electronic oscillation. Each component will correspond to a vibration pattern by expanding this motion with a Fourier transform. This quantized electronic collective oscillation is called a plasmon, but it has the more descriptive name of plasmon polariton, which describes the coupling between the electrons and the electromagnetic field. Within the local approximation, the excitation of the external electric field **E** in the Drude model is only a function of time and has no spatial dependence, so it corresponds to the **k**=0 component in the Fourier space. All electrons oscillate with the same phase, and the electron cloud oscillates "parallel" with respect to the ion background as a whole. Therefore, ω_p is the plasmon resonance frequency in the long-wavelength limit. One can also recognize that **k**=0 is the eigenfrequency of the free oscillation of the electron cloud.

The electron density inside various metals is very different. Eq. (22) shows that this results in a large difference in plasmon frequencies. For most metals, the electron density is $n_0 \sim 10^{22} - 10^{23}$ cm^{-3}, corresponding to $\hbar\omega_\mathrm{p}$ ~5–15 eV. According to the type of metal and the corresponding operating band, plasmon materials can be roughly divided into two categories: traditional metals and new materials. Traditional materials primarily refer to alkali metals (Li, Na, K, Rb, and Cs) and noble metals (Au, Ag, Cu, Al, *etc.*); novel materials including doped semiconductors [147], transparent conductors [148], carbon-based materials (such as graphene and carbon nanotubes) [149], as well as topological insulators [150].

The plasmon resonance characteristics are extensively modified in metallic nanostructures. Two distinct cases are described here, each being applicable for enhancement of perovskite device performance. These two cases are: (1) propagating surface plasmon polariton along the interface between a nano-dimension thick metal film and a dielectric, and (2) localized surface plasmons as localized charge oscillations at the metallic surface in a 3D metallic nanostructure. Both these surface plasmon modes produce significantly enhanced electromagnetic field at the metallic surface which has been utilized for enhancement of the perovskite's optical response. These two types of surface plasmons are described in the subsections below.

4.2. Surface plasmon polaritons (SPPs)

As shown in Fig. 13a, at a 2D infinite interface between a metal and its surrounding medium, Maxwell's equations can be decomposed into two mutually independent equations. Their solutions correspond to the TE (s-polarized) and TM (p-polarized) electromagnetic modes. The defined wave propagates along the x axis, and the z axis is perpendicular to the interface. For the TE mode, the electric field vector is polarized along the y direction, *i.e.*, $E_x = E_z = 0$. According to the boundary conditions, the polarization charge distribution on the surface, $\sigma_{\mathrm{p}}=(E_{\mathrm{z,d}} - E_{\mathrm{z,m}}) = 0$, where the subscripts i = d and m are used to indicate the dielectric medium and the metal, respectively. This means that TE waves cannot be associated with surface charge density, *i.e.*, they cannot be surface waves. The magnetic field in the TM mode is polarized along the y direction, and the dispersion relation for the propagating surface plasmon TM mode is given as

$$k_{sp} \equiv k_0 \sqrt{\frac{\varepsilon_d \varepsilon_m}{\varepsilon_d + \varepsilon_m}}, \tag{24}$$

$$k_{z,d} \equiv k_0 \sqrt{\frac{\varepsilon_d^2}{\varepsilon_d + \varepsilon_m}}, \tag{25}$$

$$k_{z,m} \equiv k_0 \sqrt{\frac{\varepsilon_m^2}{\varepsilon_d + \varepsilon_m}}, \tag{26}$$

Where k_{sp} is the wavevector of the surface plasmon mode, and $k_0 = \omega/c$ is the propagation constant in a vacuum. The solution in Eq. (24) shows that there is a propagating surface wave when the frequency is chosen so that the dielectric constant of the metal satisfies $\mathrm{Re}\,(\varepsilon_m) < -\varepsilon_d < 0$, with being the dielectric constant of the dielectric medium on top of the metal surface. Under these conditions from equations (24–26) we deduce that $\mathrm{Re}(k_{sp}) > k_0\sqrt{\varepsilon_d}$. This means that the mode propagates parallel to the interface along the x direction, its wavelength is less than the wavelength of light in the dielectric medium, and its electromagnetic field intensity along both sides of the interface (in the z or -z directions) is evanescent. This mode is called a surface plasmon polariton (SPP) and it is a propagating or non-localized surface wave. The particular frequency where $\mathrm{Re}\,(\varepsilon_m) = -\varepsilon_d$ is called the surface plasmon (resonance) frequency ω_{sp}, corresponding to $\mathrm{Re}\,(\varepsilon_m) = -\varepsilon_d$. Fig. 13a illustrates that the surface plasmon charge density and electromagnetic field distribution represent a coupled mode, in which the electromagnetic wave and the surface electron in the metal oscillate collectively. Due to losses, mainly from the metal, the electromagnetic field is attenuated during propagation. The characteristic length L_{sp} is defined as the propagation distance corresponding to an attenuation of the electromagnetic wave power by e^{-1}, *i.e.* $L_{sp} = 1/2\mathrm{Im}(k_{sp})$. For most metals in the visible range, the SPPs have a propagation length of approximately 1 to 10 μm.

Substituting the Drude model (ignoring damping) for the dielectric constant into the dispersion relation, we obtain the dispersion curve of the SPP, as shown in Fig. 13b. One can see from the figure that the dispersion curve of a surface plasmon polariton is on the right side of the dispersion curve of light in the surrounding medium, suggesting that its propagation phase constant $\beta = \mathrm{Re}(k_{sp})$ is always greater than the propagation constant $k_0\sqrt{\varepsilon_d}$, and its momentum is larger than the momentum of light in the dielectric. Therefore, momentum (phase) matching is required to couple light into the SPP, which is commonly done with a high index prism.

4.3. Localized surface plasmon resonance

Now we consider the optical properties of 3D metallic nanostructures, such as spherical nanoparticles (Fig. 13c), whose sizes are much smaller than the wavelength of light in the medium. The valence electrons on the metal particles will oscillate and be driven by the frequency of the light from the electromagnetic fields. When the frequency is equal to the eigenfrequency of the collective valence electron oscillation, light will be strongly absorbed or scattered. The mode is generally referred to as a localized surface plasmon resonance (LSPR) mode. At the surface plasmon frequency, the dielectric constant from the free electron model is substituted into the LSP resonance condition $\mathrm{Re}\,(\varepsilon_m) = -2\varepsilon_d$, and the resonance frequency can be obtained [21]:

$$\omega_{sp} = \frac{\omega_p}{\sqrt{\varepsilon_\infty + 2\varepsilon_d}}. \tag{27}$$

Unlike SPP, which propagates along flat and large-sized metal interfaces, LSPR is associated with bound plasmonic electrons in nanovoids or particles much smaller than the incident wavelength. SPPs have a continuous dispersion relationship and therefore exist over a wide frequency range. However, LSPR exists only within a limited frequency range due to the additional constraints imposed by the nanoparticle's boundary conditions. LSPR can be coupled directly with the propagating light, whereas SPP requires that momentum matching conditions, more commonly called phase matching conditions, be met, when coupling to an incident light wave. The LSPR spectral position of the frequency resonance is determined by the size, shape, structure, and composition of the nanoparticles, as well as by the dielectric function of the metal and that of surrounding medium [152]. LSPR spectrum can be readily shifted from the ultraviolet towards the mid-IR spectrum by chemically changing the metal or by changing the size and shape (triangular or hemispherical) of the same metal nanostructures. Fig. 14a and b summarize the spectral range of localized surface plasmon resonance in different materials. The operating wavelengths in traditional noble metals (Al, Au, and Ag) primarily cover the visible and near-infrared regions, while the operating wavelengths in transparent conductors, graphene and doped semiconductors primarily cover the near-infrared and mid-infrared regions [153].

In anisotropic metallic nanostructures, nondegenerate LSPR modes can be excited at different light wavelengths. For example, in a gold nanorod with a circular cross-section, there are two resonances: transverse (doubly degenerate) and

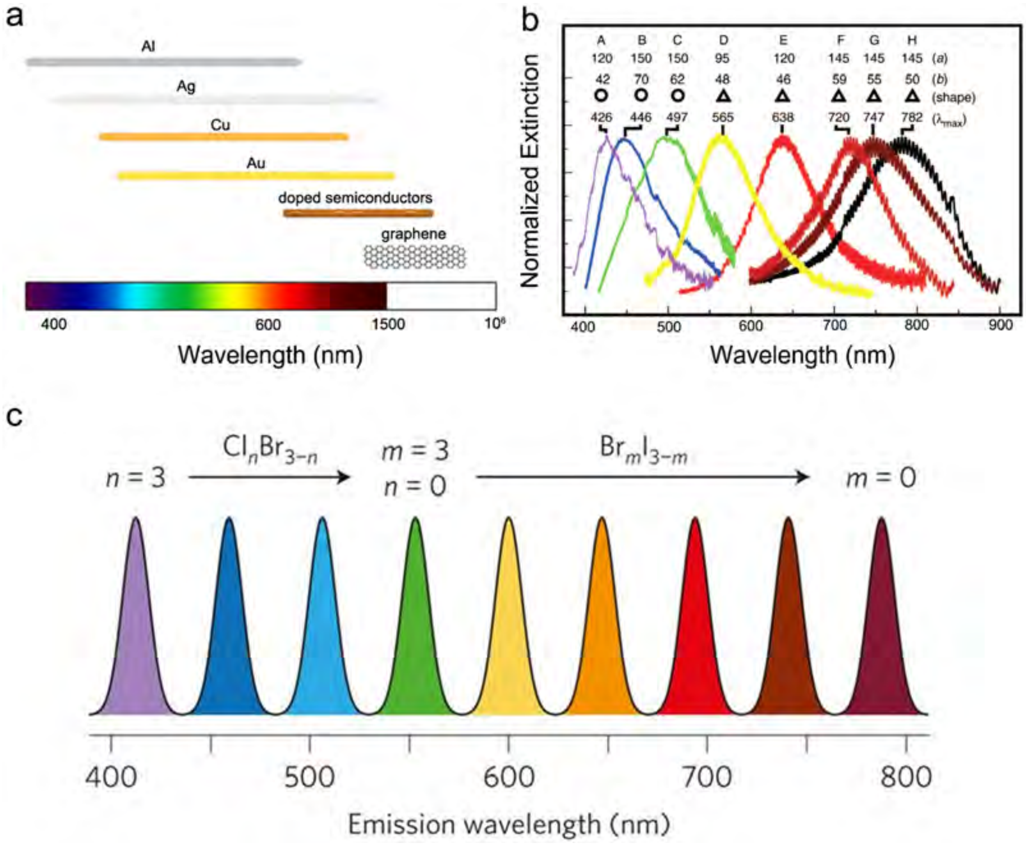

Fig. 14. (a) Approximate wavelength ranges where Ag, Au, Cu doped semiconductors and graphene have been well-characterized and are established to support plasmonic modes; (b) Size- and shape-tunable localized surface plasmon resonance spectra of various Ag nanoparticles (labeled A–H) fabricated by NSL. The wavelength of maximum extinction is changed by varying the axial ratio of in-plane width a and out-of-plane height b of the nanoparticles [154]. Copyright 2005, the Materials Research Society. (c) Wavelength tunable PL emission of perovskites with composition engineering [4]. Copyright 2016, Springer Nature.

longitudinal LSPR. The transverse resonance describes the excitation, when the electric field is polarized across the circular cross section, while the longitudinal LSPR, describes the excitation, where the electric field is polarized along the nanorod symmetry axis. The transverse LSPR wavelength is weakly sensitive to changes in the length and the width of the nanorod, but the longitudinal LSPR wavelength is strongly dependent on the length to width aspect ratio of the nanorods, and thus offers an opportunity for wide tunability of the LSPR.

It is worth noting that once the peak position λ_{max} is tuned, the half bandwidth of the LSPR does not change significantly [154]. The LSPR tunability can be used to enhance the performance in applications of perovskites in which the operating wavelengths can be tailored through controlled adjustments of the perovskite and its formulation (Fig. 14c). Core/shell nanoparticles also add a further control to move the LSP resonance across a wide band of wavelengths [21,155].

4.4. Plasmonic cavities

In order to reduce the cavity volume such that it is below the diffraction limit and simultaneously increase the coupling strength, concepts beyond those from traditional dielectric cavities must be provided. From the previous subsection, one can see that a surface plasmon polariton has several characteristics. First, its effective wavelength is smaller than the wavelength of light. Second, when the local surface is irradiated, the plasmonic resonance can enhance the electromagnetic field in the near field interfacial region. Third, the nature of the surface plasmon depends on the chemical nature of the metal as well as on the physical parameters of the nanostructure and the surrounding medium. Various plasmonic nanocavities are constructed using noble metal wires, grooves, antennas and dimers (Fig. 15). Sites with small radii of curvature along the edge of the plasmonic cavity, such as very small bulges or depressions, and gaps in multi-particle aggregates, can possess electromagnetically enhanced fields called "hot spots". Due to the effect of electromagnetic coupling, aggregates of metal nanoparticles produce an additional electromagnetic enhancement, which is much larger than the enhancement from individual particles under suitable excitation conditions.

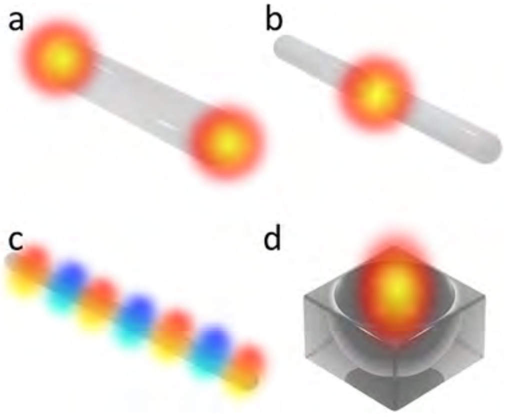

Fig. 15. Plasmonic cavity (a) plasmon antenna with hot spots, representing strong local electric fields, at the ends; (b) plasmon gap with a strong local field "hot spot" due to charge build up on each side of the gap; (c) trapped standing wave-type surface plasmon polariton cavities; (d) collapsed plasmon structures with localized modes [156].

For example, nanoparticle dimers show the strongest electromagnetic coupling effect, when the incident electric field polarization direction is parallel to the symmetry axis of the dimer. For orthogonal polarizations the interaction is generally weak. In this particular geometry the plasmonic cavity has the properties of a dipole nanoantenna with two segments separated by a gap. The electromagnetic field in the dimer nanoantenna becomes tightly constrained to the intermediate nodes of the two dipoles, thus producing a high field hot spot with a diameter of several tens of nanometers. Light can be squeezed into a tighter volume within the gap between the two nanoantennas by changing the shape of the dipole rod, which is lower than the conventional diffraction limit, with hot spot diameter being less than 10 nm.

A plasmonic cavity has large loss compared with a dielectric cavity. A typical plasmonic cavity has a quality factor that is much lower than that of a dielectric cavity. In spite of large Ohmic losses, most of the loss is essentially radiative, when the plasmonic cavity only supports the basic radiation mode, as is the case with dipole nanoantennas. In addition to their high emissivity, a plasmonic nanocavity shows additional advantages over a dielectric cavity. First, it is easier to manufacture; for instance, plasmonic cavities can be fabricatedcolloidal nanoparticles combined with various placement and patterning methods. Second, a plasmonic cavity with nanometer dimensions is smaller than a dielectric cavity. Third, plasmonic enhancement is generally more accessible within the mode volume, because the enhancement zone is located at the metal interface. Finally, the low-quality factor of a plasmonic cavity means it reacts very quickly to changes in the system, which facilitates rapid turn on and turn off times.

4.5. Interaction of perovskites with a plasmonic cavity

Metallic nanostructure and perovskites exhibit a variety of charge or energy exchange phenomena under photoexcitation. These are described below.

4.5.1. Far field scattering effect

Metallic nanostructures are capable of attenuating radiation due to resonant scattering and absorption, which is strongly dependent on particle size. The extinction coefficient of nanoparticles larger than 50 nm is primarily due to LSPR resonant scattering, while nanoparticles smaller than 30 nm only exhibit LSPR absorption.

Light incident on a plasmonic cavity having a sufficiently high reflectivity is scattered into the far field, which may be an order of magnitude larger than the physical cross section of the plasmonic cavity, depending on the geometry and material properties of the cavity. The far-field scattered light can eventually be reabsorbed by perovskites at distances of a few hundred nanometers, thereby capturing light energy for higher efficiency. Photons scattered from each nanostructure may also encounter multiple scattering from distant plasmonic cavities, ultimately increasing the total light energy captured within the perovskite (Fig. 16a). Furthermore, by adjusting the LSPR to a wavelength complementary to perovskite absorption, the plasmonic cavity can be designed to assist in capturing photons that are not efficiently absorbed by the perovskite.

We can understand the scattering property of the plasmonic cavities by applying the Mie scattering theory. The Mie theory is an analytical solution of Maxwell's equations for spherical nanoparticles, describing the extinction behavior of metal nanoparticles excited by an incident electric field. For a metal nanosphere of radius a embedded in a dielectric medium, the dielectric constants of the metal and the dielectric medium are given by the ε_m and ε_d, respectively, and the scattering cross section (σ_{scat}) is given by :

$$\sigma_{\text{scat}} = \frac{8\pi}{3}\left(\frac{2\pi}{\lambda}\right)^4 \varepsilon_d^2 \mathrm{a}^6 \left|\frac{\varepsilon_m - \varepsilon_d}{\varepsilon_m + 2\varepsilon_d}\right|^2, \tag{28}$$

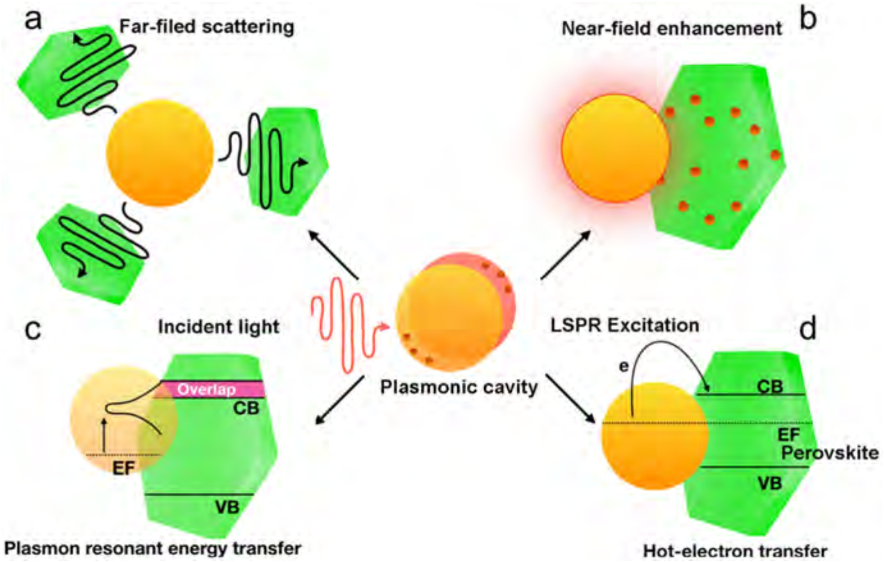

Fig. 16. Schematic illustration of LSPR enhancement mechanisms in metal-halide perovskites utilizing a plasmonic cavity: (a) far-field scattering, (b) near-field coupling, (c) hot-electron transfer, and (d) plasmon resonant energy transfer.

Since σ_{scat} is proportional to a^6, plasmonic cavities with size >30 nm are more suitable for coupling far-field scattered light into perovskite materials, thereby enhancing light trapping. As the size of the plasmonic cavity increases, light scattering increases and the amount of light absorption decreases [157]. When the diameter of the spherical Au nanoparticles is 90 nm, the amount of absorbed and scattered light is equal, indicating that the nanoparticle size can be adjusted to achieve the desired absorption and scattering intensity to maximize the energy utilization of the incident light [158,159].

Due to the polarization enhancement in the plasmonic cavity and ability to polarize incident light, the shape and size effect of the plasmonic cavity structure can also be used to control far-field scattered light. In addition, light scattering depends on the type of the elements in the plasmonic cavity, where Ag has a stronger far-field scattering effect due to its lower Ohmic losses compared to Au. The fundamental differences in the optical behavior of Au and Ag have been widely exploited; for instance, Ag has shown enhanced carrier generation. Finally, the far field effect can be adjusted by changing the dielectric constant of the medium surrounding the plasmonic cavity. As the dielectric constant increases, there is a red shift in λ_p of the LSPR frequency in the plasmonic cavity; the red shift can be visualized by considering quasi-static metal nanoparticles within the Drude approximation:

$$\lambda_p = \lambda_{p,b}\sqrt{2\varepsilon_d + 1} \tag{29}$$

where $\lambda_{p,b}$ is the volume plasmon wavelength. In addition, the sensitivity of the scattering cross section to the dielectric constant can be understood from the Mie theory, Eq. (28) is recast as:

$$\sigma_{scat} = \frac{3}{2\pi}\left(\frac{2\pi}{\lambda}\right)^4 \varepsilon_d^2 V^2 \frac{(\varepsilon_1 - \varepsilon_d)^2 + (\varepsilon_2)^2}{(\varepsilon_1 + 2\varepsilon_d)^2 + (\varepsilon_2)^2}, \tag{30}$$

where V is the nanoparticle volume and $\varepsilon_{\rm m} = \varepsilon_1 + i\varepsilon_2$. This equation shows that σ_{scat} scales with ε_d^2. When the scattered photon travels longer than the thickness of the perovskite on the upper surface of the plasmonic cavity, the electric field completely penetrates the perovskite film.

In the case of spherical nanoparticles, the Mie theory shows that relatively small particles will produce more scattering along the propagation direction, while larger particles scatter more in the backward direction. In addition, far-field scattering is related to the relative position of the plasmonic cavity with respect to the perovskite. For example, a smaller plasmonic cavity can be placed on the top of the perovskite layer to scatter the optical path of the incident light at an acute angle (<90 degrees), thereby increasing the chance of absorption. In contrast, a larger plasmonic cavity placed on the bottom surface of the perovskite will scatter light back into the perovskite film to recycle the light not absorbed by the first pass through the perovskite. Regardless of the scattering direction, multiple scattering processes are expected to improve the utilization of incident light.

By using scattering on both sides of the perovskite, unabsorbed photons can be repeatedly reflected back and forth within the perovskite until they are absorbed. Essentially, a plasmonic cavity is like many smaller cavities. Some photons that initially pass through the composite plasmonic-perovskite material without being absorbed by the perovskite can be scattered through the metal nanoparticles and pass through the system multiple times, thereby increasing the absorption of incident light by the perovskite [160]. One such instantiation of the photon recycling strategy uses films consisting of dense Ag nanoparticles.

4.5.2. Near-field enhancement

LSPR excited in a plasmonic cavity are confined near the nanostructure and cannot propagate like an SPP in a plane. Therefore, limited oscillation of electrons creates a highly localized electric field on the surface of the nanoparticle, as illustrated in Fig. 16b. The interaction between the plasmonic cavity and incident light results in a locally enhanced electromagnetic field, defined as the "near field" in the immediate vicinity of the nanostructure. Precious metal nanostructures integrated in perovskite devices are used as nanoscale concentrators to focus incident light onto metal surfaces within small mode volumes. These fields are typically several orders of magnitude stronger than the incident light field. Therefore, a plasmonic cavity can be used as a secondary light source to concentrate the light energy, and thereby the total light absorbed by the device. The electromagnetic near-field attenuation of the plasmon resonance decay is proportional to r^6, where r is the distance of the perovskite film from the plasmonic cavity. It typically extends <50 nm from the surface of the nanostructure. Since this length is usually shorter than the size of the plasmonic cavity, the perovskite must be present within the field attenuation length.

Similar to far-field scattering, the near-field intensity produced by LSPR is determined by the structure, morphology, and composition of the plasmonic cavity. Non-spherical plasmonic cavities with sharp features like nanorods, nanocubes and triangles produce a stronger near-field intensity distribution due to the lightning rod effect, resulting in a high concentration of charge at the edges and corners of the nanoparticles. Colloidal precious metal nanoparticles are the most popular system for LSPR. Since general nanoparticles shapes have no analytic solutions, finite difference time domain (FDTD) algorithms are used to simulate the effect of nanostructure morphology and composition on the local electromagnetic field strength in the plasmonic cavity. A higher near-field enhancement efficiency is observed, when the perovskite device is integrated with a non-spherical plasmonic cavity [161].

4.5.3. Energy transfer from a plasmonic cavity to perovskite

In addition to light trapping using plasmonic enhanced scattering, a plasmonic nanostructure cavity can also enhance the solar-energy-conversion efficiency by generating electron—hole pairs in a semiconductor using transfer of excitation energy from the metal to the semiconductor, when the absorption bands of semiconductors are overlapped with the resonance scattering bands of metal particles. This process is known as plasmon resonance energy transfer (PRET) and is initiated by LSPR (Fig. 16c) [162]. In a system exhibiting PRET, the plasmonic cavity acts as a donor, transferring energy to the perovskite acceptor. The transferred LSPR electric dipole creates an electron–hole pair inside the acceptor.

Several mechanisms have been proposed for exciting electromagnetic field-induced charge separation in the metal to transfer energy to the semiconductor medium. One involves direct electron transfer (DET) occurring from the plasmonic metal to the conduction band of the semiconductor, when they are in direct contact. This process depends on the alignment of the band levels of the semiconductor and Fermi level of the plasmonic metal. Thus electrons or holes can be transferred from the metal into the semiconductor at energies below the band gap, if the electronic energy levels are matched.

In another mechanism, the plasmon-mediated local electromagnetic field (LEMF) couples radiative energy to assist in the local generation of electron–hole pairs in the semiconductor. More recently, it has been proposed that the electromagnetic field mediated energy transfer can take the form of a resonant energy transfer (RET) process which directly excites electron–hole pairs in the semiconductor through nonradiative relaxation of the localized surface plasmon dipole [163]. This PRET process in the near field, is similar to Förster resonance energy transfer (FRET) discussed below in which an excited semiconductor emitter transfers energy to another medium (a semiconductor or a plasmonic medium). The PRET due to nonradiative coupling with the band edge states, is able to generate electron–hole pairs in the semiconductor at energies both above and below the band gap.

PRET is not affected by any insulating interlayer between the plasmonic medium and the semiconducting medium. PRET occurs as long as the perovskite is located in the near field of the plasmonic cavity and there is spectral overlap between the LSPR and the semiconductor absorption band. The plasmonic enhancement via PRET in a composite structure containing both a metallic nanostructure and a perovskite is determined by the morphology and the composition of the plasmonic cavity as well as by the distance between the perovskite domain and the plasmonic cavity. Photo-excited plasmonic nanostructures produce strong electric fields, orders of magnitude higher than the field of the incident photons [164,165]. Thus, LSPR transfers energy to the perovskite, generating electron–hole pairs, while the intense electric field effectively prevents the recombination of electron–hole pairs.

The evidence for PRET has been confirmed in photocatalysis experiments using TiO_2 nanoparticles. LSPR in a plasmonic cavity can transfer its amplified incident optical field energy to nearby TiO_2 nanoparticles, thereby promoting the rate of electron–hole pair generation. Moreover, the PRET from the plasmonic cavity to TiO_2 does not require direct contact [163]. PRET is achieved by coupling the LSPR's energy to the plasmonic cavity with the forbidden band of N-doped TiO_2. The mechanism of PRET can also be applied to perovskite solar cells to enhance the efficiency of electron–hole pair generation.

4.5.4. Energy transfer from perovskite to plasmonic cavity

Förster resonance energy transfer (FRET) is the mechanism of optical excitation energy transfer from an absorbing semiconductor nanoparticle (donor) to another domain (*e.g.* another semiconductor nanoparticle or a plasmonic cavity, called the acceptor). FRET is sometimes also called fluorescence resonant energy transfer. FRET can involve metal nanoparticles in two ways. First, it can transfer excitation energy from the donor nonradiatively to a metal nanoparticle. Second, FRET between a donor and an acceptor pair can be assisted by nearby metal nanoparticles [166,167]. Semiconductors store light energy in the form of electron–hole pairs. The stored energy can be lost non-radiatively via direct FRET to a metal nanoparticle, which results in decreased photoelectric performance. The transfer rate, efficiency, and energy range of FRET depend on the relative emission position (overlap region) between the perovskite fluorescence emission spectrum and the absorption spectrum of the metal nanoparticles [168]. A larger overlap between the fluorescence peak of the semiconductor and the plasmon resonance absorption peak in the plasmonic cavity, results in stronger FRET [166,169]. The non-radiative energy loss efficiency η is the primary loss mechanism in semiconductors (such as perovskites) after the introduction of a plasmonic cavity. One can approximate the FRET efficiency as $\eta = R_0^6/(R_0^6+d^6)$, where d is the distance between the perovskite boundary and the plasmonic cavity, and R_0 is the Förster radius, which is taken as 5 nm.

The interaction between photogenerated excitons in a semiconductor nanoparticle and surface plasmons in a neighboring metallic nanoparticle can result in enhanced exciton emission from the acceptor. The enhancement of this plasmonically mediated FRET between a donor and an acceptor is derived from the enhancement of electric fields inside the nanoscale assembly. Plasmonic enhancement of FRET between a donor and an acceptor can occur without excitation of real plasmons (*i.e.*, the process can be mediated by virtual plasmons).

FRET in plasmonic cavity-perovskite composites will often compete with PRET, which drains excited carriers from perovskites. The PRET efficiency depends on the LSPR dephasing time; a slower plasmonic dephasing time (10 fs) compared to the semiconductor dephasing time (5 fs) results in a dominant PRET energy transfer, whereas a longer semiconductor dephasing time results in the dominance of FRET. The PRET efficiency is a function of the metallic nanostructure–semiconductor separation distance, PRET is highest in the near field of the metal nanostructures [170].

4.5.5. Charge transfer between the plasmonic cavity and perovskites

In addition to PRET and FRET, charge transfer also plays a key role in perovskites and related plasmonic cavities. There are two possible mechanisms for charge transfer between the perovskite and a metal that is in direct contact.

a. Electrons transfer from the perovskite to the metal due to the difference in Fermi levels; this results in Schottky barrier formation at the interface.
   When the work function of the metal is larger than that of an n-type perovskite, *i.e.*, the Fermi surface of the metal is lower than that of the perovskite, the electrons flow from the perovskite to the metal until their Fermi levels are equal. This can occur without any light induced DET discussed above. This is beneficial to promote separation of electron–holes and improve the photoelectric efficiency [171].
b. Metal–electron transfer due to LSPR.
   Since the conduction band energy in perovskites is usually lower than the LSPR level of metal nanoparticles, photoexcited LSPR electrons (energy 2–3 eV) will transition to the perovskite conduction band or a defect level (Fig. 16d) [164,172]. This also contributes to plasmon resonance energy decay [173]. It should be noted that transfer of electrons caused by LSPR to perovskites increases the number of electrons in the perovskite and is beneficial in photodetection. However, the injected electrons recombine with holes in the perovskite before transported without external assistance, when a large number of electrons are injected into the perovskite. In addition, loss of electrons in metals also destroys the electron acceptor properties of the metal. Only n-type perovskites produce electron–hole pairs under proper ultraviolet light excitation. Due to the Schottky barrier and band bending, there is a space charge region at the interface between the metal and the perovskite. Electrons that are excited or transition to the conduction band at or near the space charge region, cannot cross this region, but instead are driven into the perovskite, and the corresponding holes migrate to the Fermi level in the metal. Charge transfer promotes electron conduction in the perovskite valence band and transfer of holes in the metal, separating electron–hole pairs effectively [157,174,175].
   Unlike the limitation where PRET is not balanced by the Fermi level, hot electron transfer (HET) requires that the Fermi level in the metal be aligned with the semiconductor conduction band. Electron injection from the metal to the perovskite occurs within sub-picosecond time scales. Electron injection in the perovskite leads to the following effects. First, the injection of electrons increases the number of electrons in the perovskite conduction band. Second, electron injection from the metal leaves holes in the metal valence band. Finally, injected electrons transition from the perovskite conduction band to the valence band and recombine with holes in the valence band, thus reducing the number of holes [163,164,176,177].

4.5.6. Local thermal effects

Plasmon absorption caused by the electron–phonon interaction, is a non-radiative process, which in small particles (Au <20 nm, Ag <40 nm), can cause extreme temperature changes in the particles excited using high energy pulses [178]. This local heating effect promotes thermal decomposition of organic matter in the vicinity of the particles. It may also cause decomposition of small molecules in organic–inorganic perovskites and destroy their photostability. Small noble metal nanoparticles on a substrate (such as TiO_2) can convert the absorbed energy into lattice vibrations within picoseconds. Unlike conventional heat transfer, heat transfer from small metal nanoparticles to a substrate is prohibited, because the particle size is close to the phonon mean free path in the substrate [179,180]. Therefore, the localized thermal effects do not result in significant heat transfer to the substrate.

From the above discussion, we know that a plasmonic cavity will significantly enhance the visible light response in a wide bandgap perovskite ($MAPbCl_3$, $FAPbCl_3$, *etc.*), when it exists in a composite photoelectric material. When the incident light

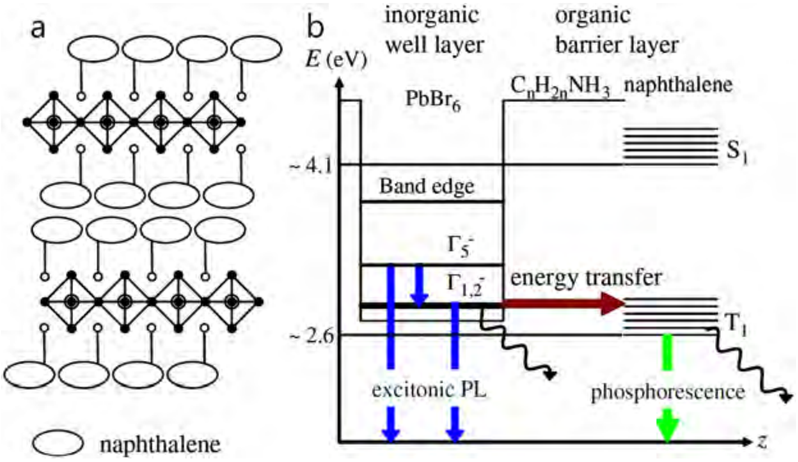

Fig. 17. (a) Schematic of the crystal structure of naphthalene incorporated 2D hybrid perovskite ($NAPbBr_4$). (b) Energy diagram and energy transfer dynamics of $NAPbBr_4$ [187]. Copyright 2008, the American Physical Society.

frequency is the same as the eigenfrequency of the plasmonic cavity, a strong, local electromagnetic field is generated on the surface of the metal nanoparticles that is several orders of magnitude higher than the intensity of the incident photoelectric field. This localized electromagnetic field strongly excites surrounding matter [181]. This means that the LSPR can effectively amplify the electromagnetic field of frequency-matched incident light [182].

5. Low dimensional metal-halide perovskites with π-conjugated organic cation

In the primary form of 3D metal-halide perovskites, ABX_3, the radius of the organic cation (A) is restricted by its steric constraints between cubic lattices of BX_6 octahedra. Thus, the function of cation A is also limited to only a structural role. However, when bulkier organic cations participate in the perovskite composition, the 3D structure of perovskites is divided into lower dimensional structures providing the potential for the photonic/optoelectronic communication between a metal-halide layer and a judiciously selected photoactive organic cation. Among the low dimensional structures, Ruddlesden–Popper 2D perovskite, consisting of well-defined 3D perovskite layers ($n = 1, 2, 3\ldots$) intercalated with bulky organic cation layer, has extra tunability in their band gap according to the number of 3D layers [183–186]. Consequently, Ruddlesden–Popper 2D perovskite incorporating various π-conjugated organic cations as an energy donor/acceptor or a charge transporting channel, can provide wide versatility to perovskite devices.

Energy transfer between the metal-halide layer and a π-conjugated organic cation by Förster or Dexter mechanism has been reported. Mitzi et al. reported proactive examples of the preparation of 2D lead halide perovskites incorporating a photoactive oligothiophene cation (5,5'''bis(aminoethyl)-2,2':5',2'':5'',2'''-quaterthiophene (AEQT)) and studied their optical properties [188]. They did not observe any evidence of the inorganic layer excitonic transition in the photoluminescence (PL) spectra for the AEQT containing perovskites, but they did observe strong PL of AEQT with the $PbCl_6$ and a PL decrease with substitution of Cl by heavier halogen atom, which was attributed to an interaction between the AEQT and lead halides by tuning energy level of lead halide layer. In a separate study, they successfully demonstrated electroluminescence at AEQT fluorescence wavelength from organic–inorganic LED (OILED) devices employing $(AEQT)PbCl_4$ perovskite as the emission layer [189].

Ema et al. reported a highly efficient triplet–triplet Dexter energy transfer between $PbBr_6$ and organic cations containing naphthyl group (Fig. 17) [187]. They demonstrated energy transfer from Wannier excitons of the metal-halide layer to the triplet state of naphthalene-linked ammonium (NA) cation in organic–inorganic hybrid perovskites ($NAPbBr_4$) by the time-resolved evolution of the excitonic PL intensities for the hybrid perovskites. An exponential decrease of the PL lifetime with a decrease in the length of the spacer between naphthalene and ammonium proved a Dexter energy transfer. Using the same mechanism, Papavassiliou et al. observed the phosphorescence band of naphthalene from the Ruddlesden–Popper 2D perovskite of (CH_3NH_3)(1-naphthylmethyl ammonium)$_2Pb_2Cl_7$ [190]. Recently, Jemli et al. reported energy transfer from a photoactive organic cation to the metal-halide layer [191]. They demonstrated a reinforcement of absorption capability of 2D perovskite by organic chromophore sensitization. To sensitize (phenylethyl ammonium)$_2PbBr_4$(PEPB), they doped 2,3-naphthalimide-ethylammonium (NAAB) into the perovskite as "collecting antenna" for light. By 10% NAAB doping, the excitonic PL of PEPB was improved up to 4.2 fold with a shift of its excitation band close to NAAB absorption band.

Another potential of π-conjugated organic cations is in their charge transporting capability. Highly ordered stacking of π-conjugated organic chromophores between metal-halide layers gives rise to the overlap of the wave function of π-electron, which can promote charge carrier mobility in perovskite devices. Kikuchi et al. incorporated a fullerene ammonium derivative, *N*-methyl-2-(4-aminophenyl)-fulleropyrrolidine (AmFP), into lead iodide perovskite [192]. They

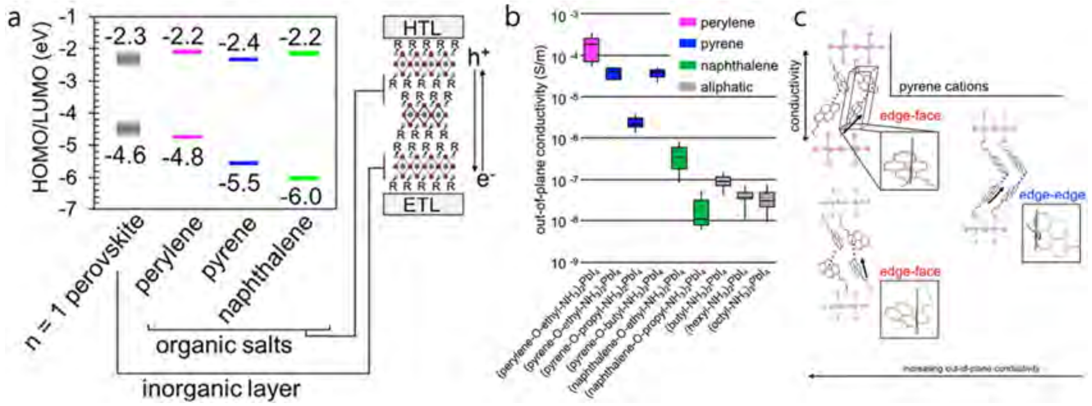

Fig. 18. (a) Energy level of typical 2D perovskite (gray) with values specific to (butyl-NH_3)$_2$PbI_4 as compared to the energy levels of the π-conjugated organic ammonium iodide salts of interest. (b) The conductivity of nine different $n = 1$ layered perovskites. (c) Crystal structure of $n = 1$ layered (pyrene-O-alkyl-NH_3)PbI_4 perovskite with various alkyl length [194]. Copyright 2018, the American Chemical Society.

observed exciton emission peak shifting to lower energy with an increase in the rate of AmFP, indicating lower exciton binding energy and easier charge separation. Era et al. incorporated hole transporting carbazole linked ammonium cation (CBzCn) into a lead bromide perovskite [193]. They successfully prepared 2D CBzCnPbBr_4 perovskite and achieved three orders of magnitude larger electric conductivity than that of the polyvinylcarbazole (CBz) film due to high order π-stacking.

Recently, a significant improvement of out-of-plane conductivity and photovoltaic performance in perovskite with the π-conjugated organic cation in 2D perovskite has been reported. (Fig. 18) [194]. Passarelli et al. prepared $n = 1$ layered 2D perovskite containing aromatic groups (perylene, pyrene, and naphthalene) and spacers (ethyl, propyl, and butyl) through an ether bond. The trend of conductivity reflected the better alignment of energy levels between the aromatic group and the metal halide layer. However, they observed a considerable difference, depending on the spacers in the same aromatic group without any trend. They could find the origin of the issue from the packing mode of the aromatic groups. The aromatic groups exhibit an edge-to-face type π-stacking interaction in higher conductivity perovskites, whereas in the lower conductivity perovskites, they reveal an edge-to-edge stacking. The highly conductive 2D perovskite led to one order of magnitude higher power conversion efficiency for $n = 1$ layered perovskite than the previous record.

6. Applications of perovskite photonic structures

Light and electron transitions are coupled via nanostructures that can enhance the desired optical emission or absorption properties. Strategies to improve photonic or optoelectronic device performance by resonance nanostructures (cavities, nanoparticles, and photonic crystals) have been amply discussed in prior sections. Recently metasurface structures are added to the research literature [195–198]. A metasurface is a subwavelength thick nanostructured interface with the specifically tailored arrangement of building blocks that produces a resonant coupling between electric and/or magnetic components of the incident electromagnetic fields in a manner not manifested in naturally occurring media. Addition of holographic metasurface structures holds potential or further improvements in device performance through control of both electronic material properties and photonic emission or absorption properties on the nanoscale.

Nanoimprint lithography has been used high index dielectric materials to fabricate metasurfaces with periodic 1D surface gratings designed to enhance the PL by a factor of eight at room temperature [196]. Further improvements of the same design concept demonstrated that perovskite materials could be shaped by nanoimprint lithography in 2D nanorods; the nanorods were shaped to control their electric and magnetic Mie resonances to enhance linear and nonlinear PL by 270 times [198].

Tiguntseva et al. reported a 50% enhancement of photoluminescence intensity from a perovskite layer with silicon nanoparticles, but they found a 200% enhancement for a nanoimprinted metasurface with silicon nanoparticles on top [199].

In the following subsections specific photonic and optoelectronic devices are treated that incorporate the nanostructures and hybrid techniques already discussed.

6.1. Photodetectors

The most intriguing features of perovskites are their high sensitivity to visible light and their high photovoltage, which are the basic parameters required for efficient solar-to-electric energy conversion. These excellent features of perovskites have been greatly explored in the photodetector. Metal halide perovskites, with the outstanding features, such as strong light absorption [3], modest charge-carrier mobility [73], balanced large exciton binding energy [200] and long diffusion lengths [12], can be fabricated with processing by solution methods. Such fabricated photo-detection devices show enhanced performance characteristics [201–204].

However, the stability of these photodetector devices is poor especially when exposed to humid environments [205]. To address this issue, photodetectors based on all-inorganic perovskites [206,207] or using better quality films, have been proposed to improve the stability of the photodetectors [208]. Constructing perovskites heterostructured with other materials is an alternative way to enhance the performance of the devices [203,209].

In addition to the material processing protocols mentioned above, coupling plasmonics into the perovskite-based photodetector can further improve the performance, which has been demonstrated before in photodetectors based on ZnO [210], InGaN [211], and InAs [212]. It is well recognized that the typical plasmonic peaks of the metal such as Au and Ag can be tuned throughout the entire visible region [213,214] by using their anisotropic form or a core–shell structure to provide an opportunity to well match with the light absorbance of perovskite. Dong et al. reported the first enhanced inorganic perovskite photodetectors by benefiting from the remarkable near-field enhancement due to the synergetic effect between a preferred-orientation film and plasmonic Au nanocrystals (Fig. 19a) [47]. These results were discussed further regarding results from finite-difference time-domain simulations. Sun et al. also demonstrated a plasmonically coupled perovskite-graphene hybrid photodetector with high responsivity enhancement (Fig. 19b) [215]. The plasmonic effect was introduced by the gold nanoparticles with a plasmonic peak localized at 530 nm. Due to the ultra-small thickness of graphene, this plasmonic effect can be concentrated around the perovskite, thus further functioning as a light-enricher. As a result, a fast photo-response of approximately 1.5 s was observed and was attributed to the interfacial effect of enhanced light-harvesting in the perovskite and the short diffusion length of photo-induced carriers in graphene. A purely perovskite-based photodetector is restricted to a narrow spectral bandwidth that mainly lies in the UV to visible wavelength range because of the perovskites' relatively large band gaps (1−2 eV) in perovskites. To extend the response of photodetection in near-infrared wavelengths, Wang et al. integrated a layer of uniformly distributed Au nanorods into vertically structured perovskite photoconductive photodetectors (Fig. 19c) [216]. It is worth noting that Au nanorods can exhibit a stronger electromagnetic field under illumination. More importantly, the longitudinal plasmon resonance wavelength can be readily extended in the IR by tuning their aspect ratio. Furthermore, Fang and colleagues successfully fabricated a perovskite-based photodetector with high photo-responsivity in the near-infrared range by introducing an array of Au nanosquares and SiO_2 spacer on an Au film plasmonic-functionalized substrate (Fig. 19d), where the favorable attributes of LSPR are fully utilized [46]. In this case, with an appropriate periodic structure, the enhanced localized electric field is dramatically larger than that of the randomly distributed metal nanoparticles. These prior results offer a promising strategy to enhance light–matter interactions in perovskite-based photodetectors. However, the fact that the enhanced field will be gradually attenuated due to the loss in the metal material should be of great concern.

In addition to using LSPR for enhancing photoresponse, SPR can concentrate and manage light by compensating the needed momentum. Suppressed recombination of photo-generated carriers can provide additional opportunities to enhance the performances of perovskite photodetectors. However, the enhancement is modest because the conditions used to excite SPP waves are rigorous. Some essential parameters of photodetectors (*e.g.*, their ultrasmall dimensions for photodetection in the sub-wavelength region, wavelength selectivity, response speed, and sensitivity) must meet the requirements of practical applications. Inspired by this point, a more plasmonic metal such as Ag, bimetals and plasmonic structures like gratings, antennas, waveguides, and microcavities can be used to construct the plasmonically-enhanced perovskite photodetectors with excellent performance. As mentioned above, although some plasmonic metals combined with the perovskite-based photodetectors have been explored, photodetectors enhanced by plasmonic structures are still limited until now, and they should be further researched systematically.

Alternatively, high-speed metal–semiconductor–metal detectors can be easily integrated into optical receivers. Also, the optical near fields can be concentrated within a sub-wavelength volume with the assistance of resonant antennas, and their optical properties can be tuned by controlling the size and shape of the antennas [217]. The sensitivity can be greatly enhanced in a nanometer-scale photodetector that combines resonant antennas with perovskites. The antenna resonance and detection wavelength can become versatile due to the tunability of the antenna resonance and the band-gaps. A specially-designed metal grating structure is another choice for launching SPPs along the desired direction, which can cooperate with perovskites to construct narrowband photodetectors with high-sensitivity. For example, patterned metal gratings can operate as an efficient and tunable coupler, enabling a narrower spectral response [218]. Here, the resonances can be dynamically tuned over a broad regime by controlling the inter-slit distance, making photodetectors with wavelength-selective detection. Combined with the virtues of a perovskite, high-performance photodetectors for light detection of particular wavelengths can be fabricated based on the grating geometry.

In addition to antennas and metal gratings, the introduction of optical microcavities into photodetector devices is considered as an alternative approach to improve detection performance. As discussed in Section 3, optical micro-cavities can effectively increase the absorption efficiency via resonant recirculation. For example, photodetectors with the wavelength selectivity and high responsivity can be fabricated by integrating a perovskite with a DBR microcavity, as shown in Fig. 19e. The wavelength selectivity of the proposed photodetector can be attributed to field enhancement in the cavity, where the field is only enhanced at the design wavelength while other wavelengths are suppressed [219]. Embedding the perovskite in the perfect metamaterial absorber can enhance light absorption. In Fig. 19f, both the forcefully localized electromagnetic resonance and light recycling contribute to enhanced light absorption. The introduction of a perfect absorber can greatly enhance the behaviors of the photodetectors, not only by suppressing reflection loss but also by combining both microcavity and plasmonic electron–light coupling. Of course, there are many optional SPR technologies that can be used to enhance the performance of the perovskite photodetector.

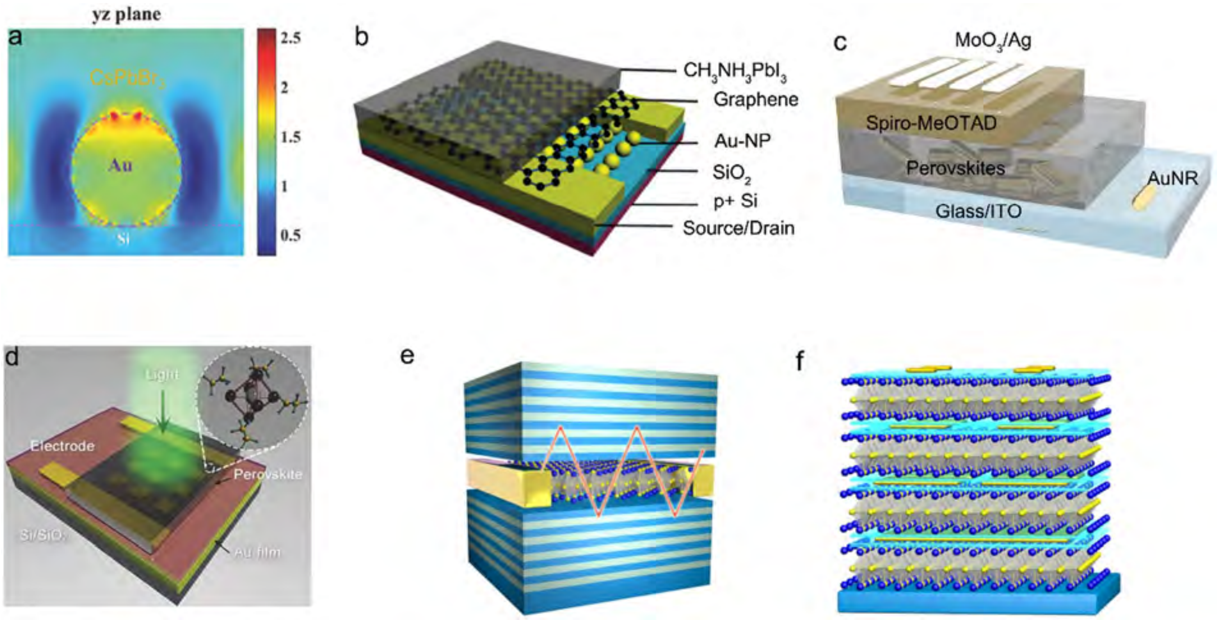

Fig. 19. (a) Finite-difference time-domain (FDTD) simulation of plasmon resonance enhancement of preferred-orientation film and Au nanocrystals at a resonant wavelength of 532 nm [47]. Copyright 2016, Wiley. (b) Schematic of a plasmonic-enhanced perovskite-graphene hybrid photodetector [215]. Copyright 2016, the Royal Society of Chemistry. (c) Device configuration of a $CH_3NH_3PbI_3$-AuNR hybrid photodetector [216]. Copyright 2018, Wiley. (d) Schematic of the perovskite photodetector on the plasmonic substrate [46]. Copyright 2018, Wiley. (e) Schematic model of a perovskite microcavity photodetector. (f) Schematic drawings of the hybrid perovskite-metamaterial photodetector.

6.2. Solar cells

As an emerging light absorber for efficient solar cells, hybrid perovskite semiconductors have received considerable interest in various structures. To improve the performance of perovskite-based solar cells, it is crucial to enhance the optoelectronic properties of the perovskite films and the interfacial charge transfer between the perovskite and the carrier transfer layers.

It is crucial to develop growth processes for the deposition of perovskite films with excellent crystallinity and coverage. To accomplish this issue, it is important to understand the mechanism for film growth. The deposition process can be differentiated into 2 phases — the nucleation phase and the crystallization phase. In the nucleation phase, a seed layer, consisting of a uniformly distributed nucleation sites over the entire substrate, is formed. In the crystallization phase, large perovskite crystals are formed over the seed layer. To accomplish high crystallinity films, a rapid nucleation step is facilitated to ensure uniform deposition of nucleation sites and to prevent pre-mature crystallization that typically leads to coalescence of large crystallites in the early stage resulting in rough morphology and high density of pinholes. This is followed by a slow crystallization step to ensure the formation of large crystals. A number of growth processes had been reported by various groups that meet such requirements for the growth of high-quality perovskite films. In particular, three deposition techniques that have successfully produced devices with efficiency >20% are summarized below:

(i) Solvent engineering technique: An anti-solvent such as toluene or chlorobenzene, is used to induce a supersaturation condition that results in the precipitation of the precursors. Chemical reaction between the precursors is retarded by CH_3NH_3I-PbI_2-DMSO intermediary phase. At the final stage, the residual DMSO is removed by thermal annealing, resulting in perovskite films with high crystallinity and uniform grain distribution [220].

(ii) Vacuum-flash Assisted Solution Process (VASP): A low vacuum is utilized to establish the supersaturation condition for the precursor film to facilitate the uniform deposition of nucleation sites. This is followed by a thermal annealing step to initiate a chemical reaction between the solutes [221].

(iii) Cryo-controlled deposition technique: A supersaturation condition is established by dipping precursor film in liquid nitrogen which freezes the film and ensures that no chemical reaction takes place pre-maturely. This is followed by the blow-drying step that gradually raises the temperature of the film above the melting point of the solvent. A supersaturation condition is established resulting in the uniform precipitation of the precursors on the substrate. No chemical reaction will take place at this stage due to the low temperature of the film. The blow-drying process serves to extract the excess solvent and chemical reaction between the precursors is initiated with a thermal annealing process. This technique is effective in decoupling the nucleation and crystallization phase with a champion optical power conversion efficiency of 21.4% in the fabricated solar cells [222].

Optical management is also essential to further enhance the performance. Plasmonic effects can effectively enhance the light absorption in the active layer via incorporating metal nanoparticles into perovskite solar cells. Three primary mechanisms have been proposed to describe the absorption enhancement using metal nanoparticles: near-field electric field enhancement [223], light scattering [224] and sensitization [225]. Snaith and colleagues attributed the enhanced photocurrent in the perovskite solar cells with incorporated core–shell Au@SiO$_2$ nanoparticles, to the reduced exciton binding energy [66]. Furthermore, Snaith's team incorporated core–shell Ag@TiO$_2$ nanoparticles in organic–inorganic perovskite solar cells and observed a significant enhancement stemming from the antenna's role of the harnessing highly polarizable metallic nanoparticles to promote more efficient reemitted light [226]. In addition, using silicon nanoparticles to enhance the light harvesting properties and then improve the efficiency of perovskite solar cells is of strategic interest [227,228]. These dielectric nanoparticles are highly Mie-resonant, and work to trap the light of a range of wavelengths close to the cell active layer. Moreover, as they cannot absorb light, they will not heat up, and are also chemically inert, and so will not interact with other parts of the cells, ensuring overall stability. Another strategy was reported by Mali et al., who demonstrated plasmonic-enhanced charge generation in perovskite solar cells with an improved photovoltaic performance by embedding Au in TiO$_2$ nanofibers [229]. The enhancement mechanism shown in Fig. 20a contributes to the reinforcement of light absorption and limited charge recombination in the Au@TiO$_2$ electrodes, thus acting as a Schottky barrier herein. In this case, three mechanisms are occurring simultaneously: electrons transfer from the LUMO in the perovskite to the CB in TiO$_{2;}$ electrons rapidly transport from Au to the CB in TiO$_2$ due to the increased Fermi level increase in Au, producing photocurrent; electrons generated by LSPR diffusing from Au to the CB in TiO$_2$ to enhance the photocurrent. However, unexpected efficiency losses will be induced by the intrinsic losses in the visible region in metals. Therefore, overcoming these negative effects remains an important issue. Huang and colleagues synchronously incorporated Au@TiO$_2$ core–shell nanoparticles into the TiO$_2$ film and the perovskite layer [230]. They developed an efficient plasmonic composite structure to enhance the perovskite solar cells performance. The addition of Au@TiO$_2$ nanospheres increased the rate of exciton generation and the probability of exciton dissociation, enhancing charge separation/transfer and facilitating carrier transport in the device. However, there are several challenges for the practical applications of plasmonic structures in perovskite-based solar cells. The first one is the presence of parasitic absorption in the plasmonic nanoparticles, which competes with useful absorption in the perovskite material. Another drawback comes from that embedded plasmonic nanostructures can act as non-radiative recombination centers of the carriers, resulting in a reduction in device open-circuit voltage as well as current. Approaches have been applied to resolve the issues mentioned above, *i.e.*, choose an appropriate plasmonic material with specific shape and size can be used to manipulate the relative amount of parasitic absorption [231]. Meanwhile, including a small insulating barrier in the form of a ligand or dielectric shell around the plasmonic nanostructure can suppress recombination effect, but can also reduce the evanescent spatial field overlap with the photovoltaic absorber, thereby limiting the potential for absorption enhancement [230].

It is well known that, besides the plasmonic noble metal nanostructures, fabrication of photonic cavities is an alternative optical management method. Compared with the narrowband response of the plasmonic noble metal nanostructures, broadband enhancement can be achieved by using various photonic cavities, especially those with 3D periodic microstructure. Besides, the quality and thickness of the perovskite should play a crucial role in enhancing the photovoltaic performance, especially regarding the enhancement of external quantum efficiency. Increasing the thickness of the perovskite film can somehow maintain the external quantum efficiency in the region of 500–800 nm, but charge collection efficiency is sacrificed, and the large abnormal *J-V* hysteresis is observed as a result. Consequently, Long et al. demonstrated another absorption enhancement approach by using a periodic structure to improve plasmonic light harvesting and hole collection, rather than increasing the thickness [232]. They combined a F–P interferometer and SPR in a single cavity, which can effectively enhance the light absorption. In addition, a quasi-periodic microstructured composite hole transporting material can also increase hole conductivity. The highest efficiency (17.7%) of the perovskite solar cells (Fig. 20b) with an ultrathin perovskite layer (240 nm) was demonstrated due to the optical and electronic enhancements.

Some novel plasmonic designs can also be used to improve the performance of perovskite solar cells. Plasmonic tandem geometries may be the first choice to increase light confinement when designing perovskite-based solar cells, where each metal layer with a different plasmonic nanostructure can interact with the corresponding perovskite layer with different band gap tuned by composition engineering [37]. In this case, every plasmonic layer can confine light of a different wavelength from the solar spectrum in the corresponding perovskite layer (Fig. 20c). Perovskite-based quantum dots are another candidate to form the absorbing layer that can couple with the SPPs, and yield improved light absorption in perovskite quantum-dot solar cells, without increasing the quantum-dot layer thickness (Fig. 20d). Moreover, the light trap in this structure is insensitive to the angle of incidence, which allows this perovskite quantum-dot solar cells to absorb indirect solar radiation. Similar to the design of a nanometer-scale perovskite photodetector, plasmonic antennas (axial heterostructure, coaxial holes in a metal film and so on) could be used to engineer a nanoscale perovskite solar cell (Fig. 20e and 20f). Meanwhile, combined optical management through plasmonic noble metal nanostructures and light cavities can effectively enhance the perovskite solar cells performance.

For the commercialization of the perovskite solar cells, a significant scientific issue is not only the efficiency but also its stability. Lack of stability of perovskite solar cell is mainly attributed to the high water solubility of the materials in perovskite, which leads to degradation under high humidity. The suggested strategies for improving the stability are the Ruddlesden–Popper 2D perovskites, dividing 3D hydrophilic nanolayers by 2D hydrophobic nanolayer [234,235] and introducing organic crosslinkers, to connect interfaces of perovskite grain to grain or perovskite layer to charge transporting layer [236]. In this

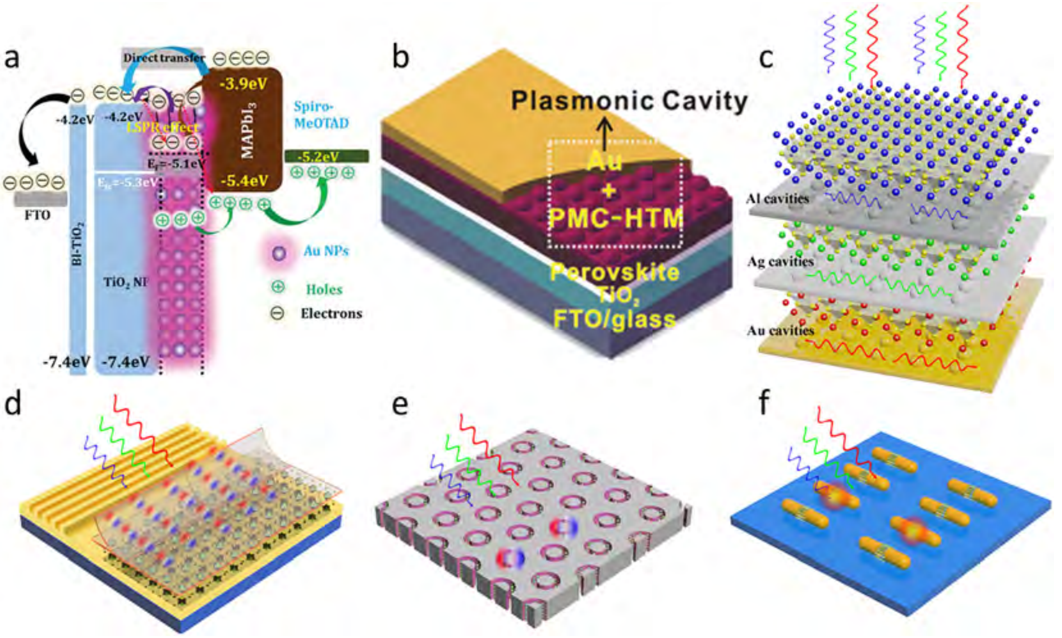

Fig. 20. (a) The efficiency enhancement mechanism of the gold nanoparticle-embedded TiO_2 nanofibers enabling plasmonic perovskite solar cells [229]. Copyright 2016, the Royal Society of Chemistry. (b) Device configuration of an efficient perovskite solar cell employing a periodic structure of a composite hole conductor [232]. Copyright 2016, the Royal Society of Chemistry. (c) Schematic of a plasmonics-perovskite tandem solar cell. (d–f) Schematic of perovskite based solar cells coupled with plasmonic antennas.

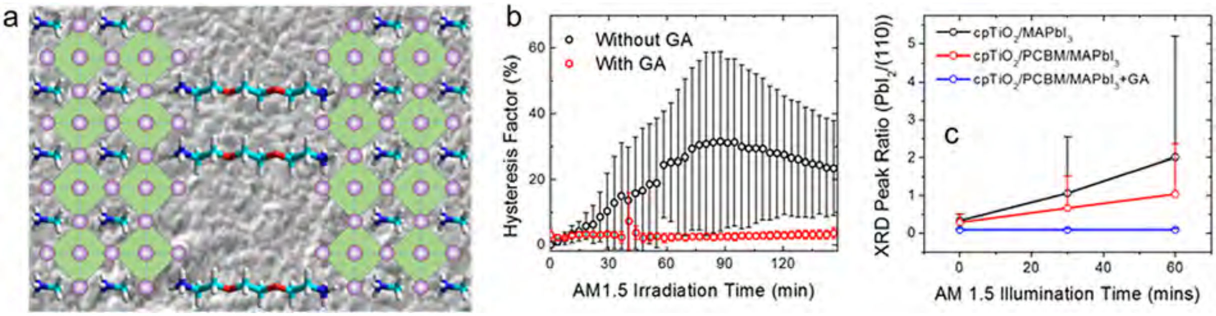

Fig. 21. (a) Chemical structure and morphology of $CH_3NH_3PbI_3$ perovskite with 2,2′-(ethylenedioxy)bis(ethylammonium iodide) (GA) (b) Time-dependent change in hysteresis between forward and reverse scans under continuous AM1.5G illumination. (c) XRD peak area ratio of PbI_2 to perovskite (110) of the three devices before and after continuous illumination of AM1.5G for 30 or 60 min [233]. Copyright 2018, Elsevier.

last strategy introduced by us, an organic crosslinker, 2,2’-(ethylenedioxy)bis(ethylammonium iodide) (GA) is incorporated as a dopant into $CH_3NH_3PbI_3$ perovskite. We observed significant improvements in stability and performance of perovskite solar cell (Fig. 21) [233]. The two ammonium groups of GA allowed it to serve as a crosslinker in the structure, bridging grain boundaries of perovskite nanocrystals. In a planar heterojunction solar cell, the power conversion efficiency of the cell with ~0.1% GA in the perovskite layer was slightly exceeding that of the glycol-free device, but most importantly, the typical hysteresis in perovskite solar cell was completely suppressed with the GA. The GA substantially improved the chemical stability of perovskite under continuous AM1.5 G illumination at ambient conditions.

6.3. Light-emitting diodes and display

Since Round and Losev reported the first prototype of an illumination device based on electroluminescence from inorganic carborundum (SiC) in 1907, light-emitting diodes (LED) based on various nanomaterials are rapidly developing with a growing commercial market [237]. Organometallic halide perovskites possess high photoluminescence quantum efficiency (PLQE), superior electronic properties, and unique band structures, making perovskite materials suitable for high-performance, low-cost, large-area, and lightweight LEDs. We will address the application of perovskites for LEDs applications in this section. Zeng and co-workers demonstrated the first perovskite-based LEDs (PeLEDs) based on $CsPbX_3$ quantum dots in 2015 [238]. Following that the past years have witnessed rapid improvement in the performance of PeLEDs in terms of external quantum efficiencies and device stability [239–241]. Although a dominant breakthrough enabling the commercialization of PeLEDs is yet to be realized, continuous technical improvements on perovskite synthesis and device fabrication are steadily approaching this goal. Presently, the primary factors hindering the development of PeLEDs arise from two issues. First, defect states in the perovskite active layer and interlayer surface lead to trap states mediated nonradiative processes, which reduce the probability of carrier injection and radiative recombination. Second, the operational stability of PeLEDs is a crucial concern in making them durable and reliable. In order to further improve the EQE and device stability, a new exciton recombination pathway must be formed by coupling LSPs and excitons while integrating a novel nanocavity in PeLEDs to increase the exciton recombination ratio [242]. In the following subsections, we will discuss PeLEDs structures, their related photophysics, and efforts focused on improving the PeLEDs.

6.3.1. PeLEDs device structure

Traditional LEDs rely on direct band gap semiconductors [243–245], such as GaN or $In_xGa_{1-x}N$. The key parameters that serve as a figure of merit to judge a material's suitability for light emitting are the PLQY, which is the ratio of the number of emitted photons to absorbed photons. Specifically, in an LED, the radiant efficiency (RE) defined by the electrical to optical energy conversion efficiency, is given as:

The external quantum efficiency (EQE) is the ratio of emitted photons to the number of electrons injected into the device, is the proportion of electrons injected into the active emitter layer to the number of electrons passing through the device, the internal quantum efficiency (IQE) is the proportion of radiative electron–hole recombination in the emitter layer, is the proportion of excited photons in the emitter layer to the total number of injected photons, and the luminous efficacy (LE) is the ratio of emitted light (L) to injected electrical energy (IV) by the source.

Among these parameters, the most significant figure of merit is the EQE for LEDs, which directly measures how efficiently the device converts electrons to photons. In the past five years, perovskites have gained tremendous PLQY improvements. Perovskite thin films formed from solutions are the most promising materials among all solution-processed semiconductors. In addition to 3D solution-processed thin films, other synthesis methods for lower dimensionality perovskites structures (perovskite QDs, perovskite nanoplatelets, nanoparticles, *etc.*) have been utilized to maximize PLQY values arising from their binding energies, increased oscillator strengths, and remarkable quantum confinement effect [43].

In principle, there are four essential components in a complete PeLEDs device architecture: a front transparent electrode (*e.g.*, FTO, ITO, and graphene, *etc.*), an electron-transporting layer (ETL) (*e.g.*, ZnO or TiO_2), a hole-transporting layer (HTL) (PEDOT:PSS and spiro-MeOTAD as the most frequently materials), and a back electrode. The PeLED architecture may be generalized as ETL/perovskite/HTL and HTL/perovskite/ETL, illustrated as Fig. 22a, with the generated light transmitting through the HTL and transparent electrode for the former and the ETL for the latter. In general, PeLEDs can be summarized as structures depicted in Fig. 22b, both carriers including holes and electrons recombine in the perovskite active layer. Band alignment and construction of these four components intrinsically defines the performance of PeLEDs. Carriers injected through the electrode should be efficiently transported to the emitter, and proper interfacial conditions must be used to suppress electrical and optical losses of injected carriers.

Following this line of thoughts, much effort has focused on obtaining high efficiency, bright, and stable PeLEDs. R. Friend and co-workers initially reported a bright LED based on a solution-processed perovskites in 2014 [242]. This green LED used a $CH_3NH_3PbI_{3-x}Cl_x$ thin film as the light emitter, which was sandwiched between larger band gap TiO_2 and poly (9,9'-dioctyl-fluorene) layers, exhibiting an appreciable quantum efficiency of 0.4% (Fig. 22c). Since then, both solution-processed perovskites and nanostructure perovskites crystals have been employed as the emitter in PeLEDs.

Referring to solution-processed thin film PeLEDs, various protocols have been used to improve film quality and uniformity, including altering the crystallization rates and controlling nucleation conditions. An SOCP/$CH_3NH_3PbBr_3$/TPBi/LiF/Al device configuration was reported to obtain and EQE of 8.53% due to reduced grain sizes and decreased Pb atomic lattice defects [246].

As described in the previous section, nanostructured low dimensional perovskites nanocrystals exhibit high PLQY, and PeLEDs with perovskite nanostructures employ these unique advantages. Yuan et al. and Wang et al. obtained devices with near-infrared EQEs of 8.8% and 11.7%, respectively [247,248]. More recently, Xiao et al. also reported an EQE of 10.4% in hybrid perovskites nanostructures [249] combined with nanocrystal pinning and 2D perovskites. Thanks to improvements in composition and phase modulation in quasi-2D perovskites, You and co-workers reported efficient green PeLEDs with glass/ITO/PEDOT:PSS/$PEA_2(FAPbBr_3)_{n-1}PbBr_4$/TPBi/LiF/Al configuration and an EQE of 14.2%, to the best of our knowledge, this is the highest EQE value presently reported as Fig. 22d [18].

6.3.2. PeLEDs photophysics

While PeLEDs devices have shown rapid development, research into the mechanism influencing the optoelectronic performance of perovskites continues. A thorough understanding of the carrier dynamics processes, including carrier injection, transport, and recombination, would be significant for future development in this field. Perovskites are the ambipolar materials that possess long and balanced charge-carrier diffusion lengths, which makes it a promising useful material for LED.

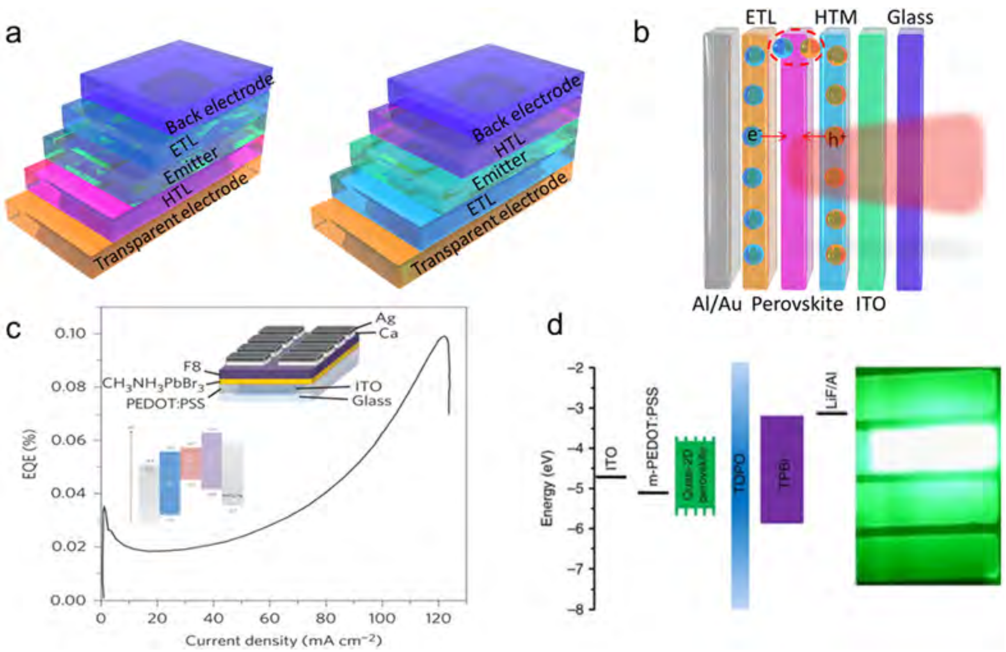

Fig. 22. (a) Schematic diagrams of the light emitting diodes. (b) Basic configurations of perovskites LED. (c) External quantum efficiency (EQE) versus current density of the green PeLED. Inset: Green PeLED device structure [242]. Copyright 2014, Springer Nature. (d) Efficient green light PeLED configuration based on confined 2D perovskite as active layer [18]. Copyright 2018, Springer Nature.

6.3.3. *Surface plasmonic coupling on PeLEDs*

Although a great deal of effort has focused on increasing the quantum conversion efficiency in PeLEDs via dimensionality confinement, surface modification, and polymer blending, the performance of PeLEDs still need to be further improved compared to transitional LEDs. To create a pathway for the radiative recombination and reduce energy loss from the non-radiative process for maximizing the internal quantum efficiency (IQE), the coupling between excitons and surface plasmons was proposed. For example, Zhao and co-workers demonstrated highly localized lasing from perovskite lasers based on silver nanowires embedded in a $CH_3NH_3PbBr_3$ perovskite microcrystal cavity [250]. In this work, the SPPs can be excited and propagate in silver nanowires, and the perovskite microcrystals function as the gain medium and a high-Q resonant cavity, generating a low-threshold laser. Thus, the coupling is equal to the laser output that can be tuned with the controllable perovskite resonant modes. Chen and co-workers proposed a composition of $CsPbBr_3$ all-inorganic perovskite and Ag plasmonic nanorods, as shown Fig. 23a [251], to show that the luminance and efficiency of these PeLEDs increased by 42% and 43.3%, respectively, which can be attributed to the near-field effect induced by Ag nanorods, which increases the spontaneous emission rate. Therefore, a maximum EQE of 0.43% was reported in this plasmonic PeLED structure. Following this study, organic–inorganic $CH_3NH_3PbBr_3$ were used to incorporate the plasmonic Au nanoparticles (AuNPs) (Fig. 23b) [252]. They reported a 109% enhancement in the maximum luminance and 97% enhancement in maximum EQE. Such enhancements are caused by coupling between excitons in the high-quality $CH_3NH_3PbBr_3$ perovskite and SPR in the AuNPs. High-efficiency plasmonic PeLEDs can support a maximum EQE of ∼1.83%. According to this line of thought, Shan and co-workers proposed a coaxial core/shell heterojunction architecture (Au/p-NiO/$CsPbBr_3$ QDs/MgZnO/AuNPs/n-ZnO/n^+-GaN) to apply in LSPR enhanced PeLEDs, as shown in Fig. 23c [41]. Due to the increased spontaneous emission rate and improved IQE resulting from coupling between excitons and LSPR, the maximum EQE of the obtained plasmonic PeLEDs increased up to ∼4.626%. In addition, the devices exhibited substantially improved stability against water and oxygen degradation. To effectively control the electrode quenching and improve the performance of PeLEDs, Chen and co-workers introduced AuNPs into the interface between PEDOT:PSS and $CsPbBr_3$ as in Fig. 23d, to form a plasmonic PeLED [253]. The generated LSPR could contribute to the hole transport. As a result, the maximum luminance enhancement and maximum EQE enhancement of the obtained plasmonic PeLEDs were ∼226% and ∼86%, respectively. In summary, coupling between excitons in high-quality perovskite crystals and SP in a metal structure is an effective pathway to enhance the performance of LEDs.

6.3.4. *Nanocavity integrated van der waals heterostructure light-emitting tunneling diode*

Aside from coupling between excitons and SPR for the optimal LED performance, an alternative approach involves assembling a novel nanocavity enhanced light-emitting tunneling diode. The idea, depicted in Fig. 24a origins from recent breakthroughs in organic LEDs, where a plasmonic nanocavity organic LEDs was proposed by Chou's group [254]. A metallic-mesh electrode with a subwavelength hole-array was used as a plasmonic cavity, and electron and hole transport layers

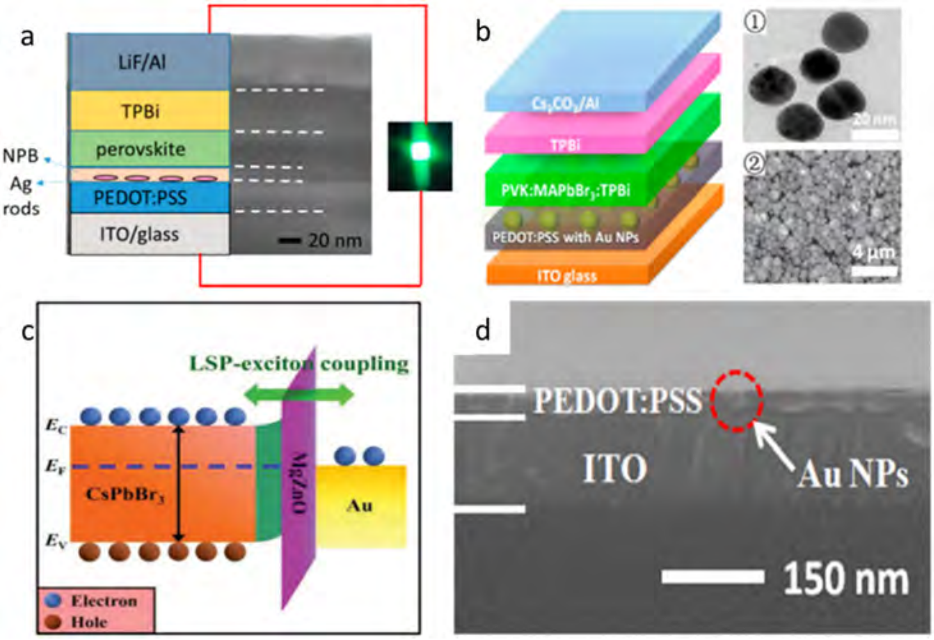

Fig. 23. (a) Schematic diagram and TEM image of Ag-$CsPbBr_3$ system [251]. Copyright 2017, the American Chemical Society. (b) The device structure of the plasmonic perovskite LEDs based on PEDOT:PSS layer incorporating Au NPs coupling with $MAPbBr_3$ [252]. Copyright 2017, the American Chemical Society. (c) Band alignment of the Au/MgZnO/$CsPbBr_3$ heterostructures [41]. Copyright 2017, Wiley. (d) Cross-section SEM image of the Au NP modified PEDOT:PSS layer [253]. Copyright 2018, IOP.

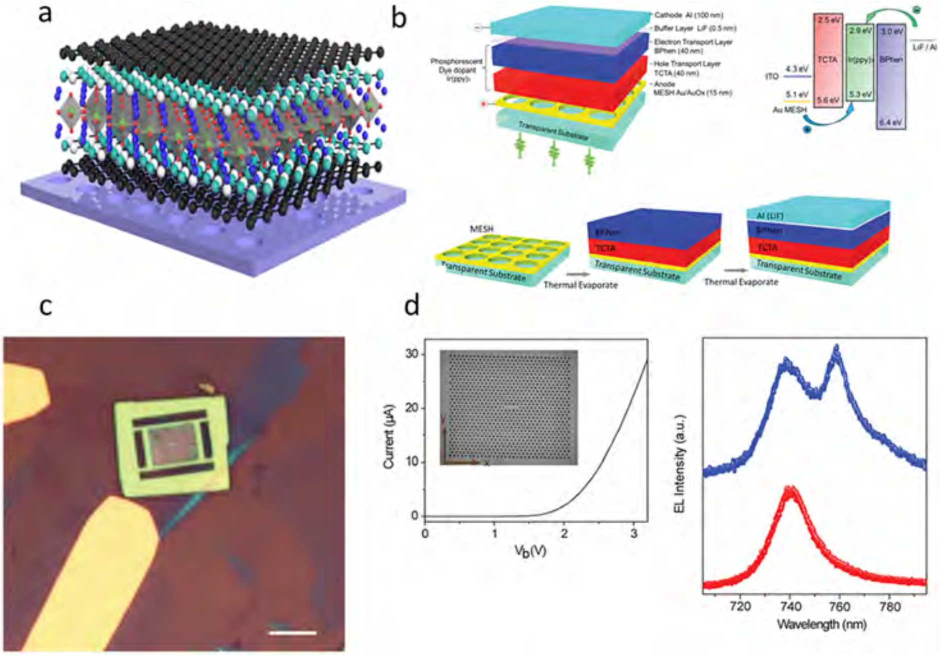

Fig. 24. (a) Schematics of Nanocavity integrated van der Waals and perovskites heterostructure LED. (b) The schematic diagrams of Plasmonic nanocavity enhanced OLED: The structure from top: a top (Au) metallic-mesh electrode with subwavelength hole-array (MESH), a back electrode (LiF/Al), and in between thin layers of green phosphorescent organic host–guest materials: BPhen and TCTA (both Ir(ppy)3 dope [254]. Copyright 2014, Wiley. (c) Optic image of nano-cavity integrated van der Waals heterostructure light-emitting tunneling diode based on WSe_2 [255]. Copyright 2017, the American Chemical Society. (d) I–V characteristics of the light emitting heterostructure. Inset: Scanning electron microscopy image of the photonic crystal cavity. EL measured from (blue dots) and away (red dots) from the cavity area with $V_b = 2$ V [255]. Copyright 2017, the American Chemical Society.

were composited as Fig. 24b. This nanocavity configuration exhibited improved performance compared to transitional LEDs without nanocavities, including a 1.57-fold EQE increase and 2.5-fold ambient light absorption efficiency increase. Majumdar et al. fabricated a van der Waals heterostructure nanocavity for LEDs by integrating a photonic crystal cavity on top of the vertically assembled WSe_2 device. The optic image defines the proper stacking of this van der Waals stacking structures shown in Fig. 24c [255], they observed a factor 4 increase in electroluminescence, which shows that nanocavity structure is a promising LED platform (Fig. 24d). Very recently, high-quality white organic LEDs were demonstrated by integrating a nano-hole array and a half-spherical lens, which exhibits a maximum EQE of 78% [256]. Similar design concepts can be employed for PeLEDs.

6.4. Nanolasers

In addition to photovoltaics and LEDs, laser is another significant device where perovskites can provide an active gain medium. Since the invention of semiconductor solid-state laser in the mid-20th century, lasers have been widely used in a variety of fields including bioimaging, micro machining, communication and spectroscopy [257–260]. With the exceptional optic properties such as large absorption coefficient, low defect density and long carrier lifetimes, perovskite is viewed as an excellent candidate for fabricating high-performance laser. The first realization of ultralow threshold room-temperature (RT) amplified spontaneous emission and lasing from $CH_3NH_3PbX_3$ ($X = Cl^-$, Br^-, and I^-) polycrystalline thin films in early 2014 [79], amidst the solar-cell efficiency race, launched a new light-emission direction for 3D perovskites. This can be traced to the tantalizing possibility of realizing electrically driven lasing by harnessing the long-range ambipolar charge-transport properties of $CH_3NH_3PbI_3$. In this subsection, we will review the notable work on perovskites-based nanolasers with different cavities.

Perovskites have been demonstrated as a good gain medium in nanolasers [79,261]. However, on account of the poor crystallinity and pinning hole in 3D perovskite thin films, too high lasing thresholds were still the big problems in these researches. To solve this problem, Zhu et al. used a low-temperature solution processing for the growth of high-quality single-crystal lead halide perovskites ($CH_3NH_3PbX_3$, X=Cl, Br, I) nanowires (NWs) [29]. The corresponding nanolaser device exhibits a very low lasing threshold ca. (220 nJ cm^{-2}) and high-quality factors (Q) ca. 3600. The results establishing room temperature lasing from single crystal perovskite NW, played an important role in the development of perovskite nanolasers. Liu's group designed high quality hexagonal-periodical $CH_3NH_3PbI_3$nanoplatelet arrays on boron nitride using a bottom-up scalable patterning strategy [262]. The photoluminescence intensity of the heterostructure increased sharply beyond the pump fluence threshold (9.6 μw cm^{-2}) which directly proved the signature of lasing. By utilizing the whispering-gallery (W-G) mode of this optical cavity (Fig. 25a), they obtained a high Q ca. 1210. Moreover, in this report, single mode lasing selectivity can also be obtained by changing the size of the nanoplatelet or breaking the structural symmetry of the cavity through designing of these patterns. Following this thought of the line in shape engineering of perovskites, a cube-corner pyramid cavity of the $CH_3NH_3PbBr_3$ was further discussed by the same group (Fig. 25b), and a special F–P mode was employed in this study to interpret the light confinement in the cavity [114]. Combining with a thin layer of Ag film, the threshold can be obtained as 26 μJ cm^{-2}, accompanied by room temperature lasing with a threshold of ca. 75 μJ cm^{-2}.

Besides the W-G and F–P cavities, another optical cavity of perovskite such as distributed feedback (DFB) cavity designed by Riede and Snaith (shown as Fig. 26a), also showed great potentials in modulating the emission properties of perovskite [130]. The DFB cavity was fabricated by an improved strategy of evaporating perovskite onto a nanoimprinted polymer resist, the vertical and horizontal morphology of the structure is shown in Fig. 26b and 26c. The optical feedback was provided by Bragg scattering from an interference grating built either directly into the active medium or within the vicinity of the whole resonator by periodically alternating the refractive index. Thus, the emission between 770 and 793 nm can be simply tuned by varying the grating periodicity. It is the first time a feasible 2D patterned perovskite structure was obtained, and the structure revealed great potential in telecommunication application due to the broad and continuous tunability of emission from 1.1 to 3.1 eV.

Utilizing a 2D photonic crystal cavity, Nurmikko et al. prepared a photonic crystal laser of $CH_3NH_3PbI_3$ (Fig. 26d), demonstrating the high degree of temporally and spatially coherent lasing where by well-defined directional emission is achieved near 788 nm wavelength at optical pumping energy density threshold of $68.5 \pm 3.0 \mu Jcm^{-2}$ [36]. The measured power conversion efficiency and differential quantum efficiency of the perovskite photonic crystal laser are $13.8 \pm 0.8\%$ and $35.8 \pm 5.4\%$, respectively. This report gives proof-of-concept scalable production of a 2D arrayed perovskite microlaser.

Making use of the architectures such as optical cavity to tune the properties of lases is a common method. The surface plasmon resonance (SPR) effect is another very efficient modulation method for the nanolasers. Recently, Shang et al. constructed an $Ag/SiO_2/CH_3NH_3PbI_3$ NWs hybrid-geometry nanolaser, combining both the advantages of surface plasmon polaritons (confinement below the diffraction limit) and high gain properties of the perovskite [108]. Thus, the plasmonic NW laser not only exhibited a promising prospect in deep sub-wavelength regime together with ultrafast lasing dynamics for perovskite, but also showed low threshold operation. Based on this report, a similar structure of $Au/SiO_2/CH_3NH_3PbX_3$nanosheet (X=Cl, Br, I) were studied by Huang et al. [263]. The schematics and characterization of the structure are illustrated as Fig. 27a, b, and c, by observing the intensity and spectrum variation of the photoluminescence of the structure on the perovskite nanosheet under different Au/SiO_2 substrate (Fig. 27d). They show that the resonances within this hybrid plasmonic nanolaser can be influenced by the shape and size of the bottom Au patterns. As a result, by patterning the substrate into Au disks and Au strips, the circular hybrid plasmonic nanolaser and the uniform plasmonic

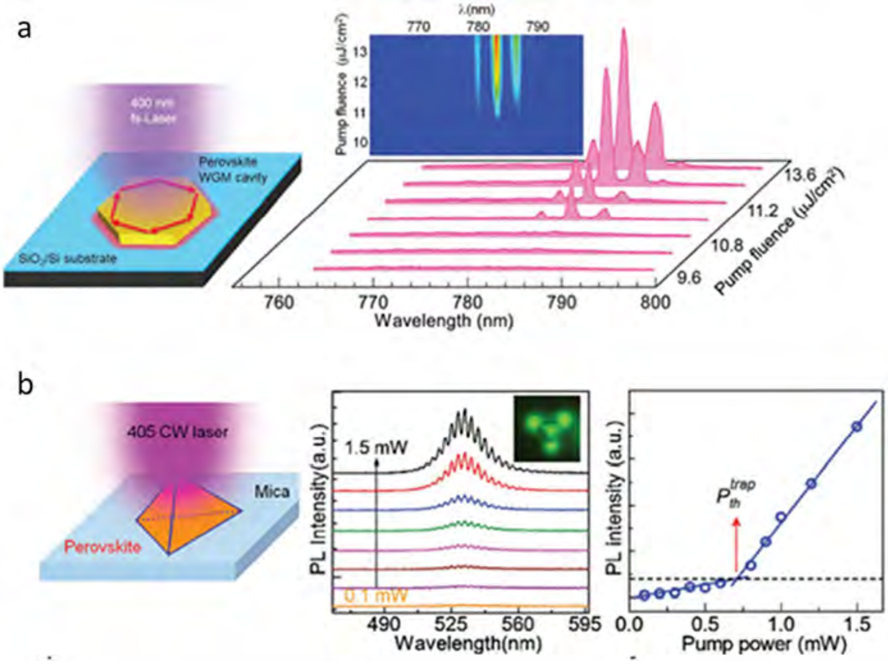

Fig. 25. (a) Schematic of $CH_3NH_3PbI_3$ platelet on silicon substrate pumped by 400 nm laser excitation (≈50 fs, 1 kHz). Emission spectra at different pump fluences recorded at around the lasing threshold. Inset is the 2D pseudo color plot of emission spectra under different pump fluences (P). A broad SPE (spontaneous emission) is observed below the threshold (≈10 μJ cm^{-2}), and narrow lasing peaks can be seen above the threshold [262]. Copyright 2016, Wiley. (b) Schematic configuration of a typical cube-corner $CH_3NH_3PbBr_3$ pyramid on mica substrate pumped by a 405 nm solid laser excitation. μ-PL spectra of a cube-corner $CH_3NH_3PbBr_3$ pyramid under different excitation powers, clearly showing surface-emitting coherent light emission. The inset shows the photoluminescence emission image of the triangular pyramid at 1.5 mW [114]. Copyright 2018, Wiley.

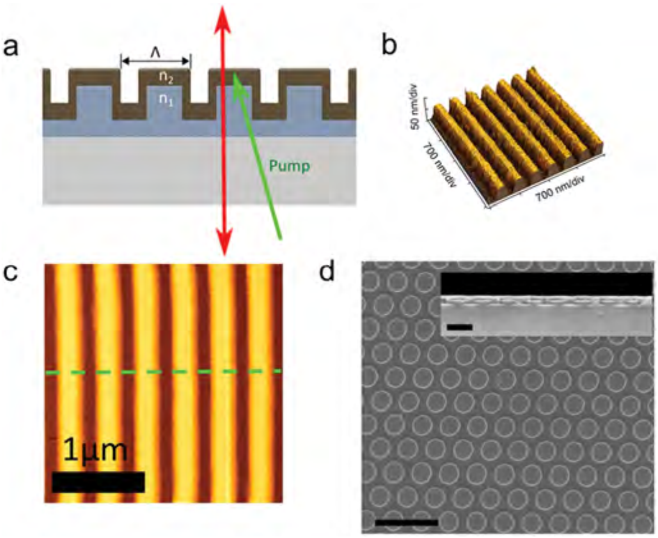

Fig. 26. (a) Schematic diagram of a DFB cavity with a glass/patterned polymer resist/perovskite structure. Upon optical pumping, the DFB structure responds with surface emission in the case of second order Bragg scattering. Atomic force microscopy (AFM) images of the patterned polymer resist in (b) 3D and (c) 2D [130]. Copyright 2016, Wiley. (d) Plan view SEM image of 2D PhC showing the uniformity of the nanostructured pattern. The scale bar is 1 μm. Inset shows cross-sectional SEM image of perovskite film on 2D PhC pattern. The film deposits conformally with perovskite grains filling spaces between PhC nanopillars with subsequent surface planarization. The scale bar is 400 nm [36]. Copyright 2016, the American Chemical Society.

nanolaser array are achieved. Although in this paper, the structure of Au on the SiO_2 substrate is not a continuous film but a discrete array. It put forward the crucial point that a hybrid plasmonic nanolaser can be precisely controlled by the

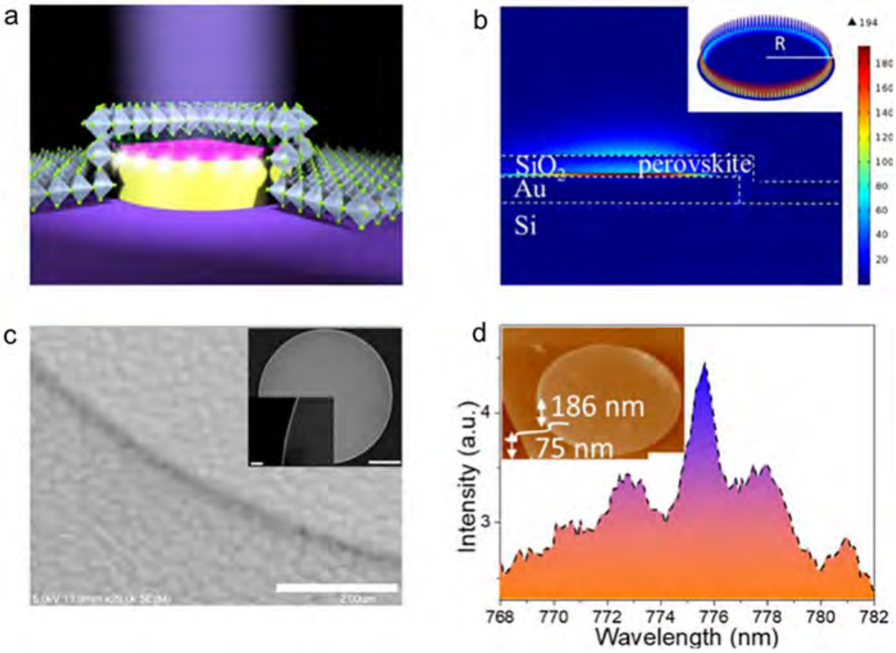

Fig. 27. (a) The schematic picture of perovskite nanosheets covered on the Au/SiO_2 disk. (b) The numerically calculated mode confinement within the hybrid plasmonic nanolaser in cross-section. Here the light is confined along the boundary of Au pattern. Inset shows the 3D field pattern reconstructed with the Azimuthal number m. (c) The SEM image of perovskite plates covered on Au/SiO_2 disks. Scale bar: 2 μm. Inset shows the SEM image (scale bar: 5 μm) and the high-resolution magnification image of Au/SiO_2 disk. Scale bar: 500 nm. (d) Emission spectrum of the perovskite microplates on Au/SiO_2 disk above threshold. Inset: AFM image of perovskite plates covered on Au/SiO_2 disks. Scale bar: 5 μm [263]. Copyright 2018, the American Chemical Society.

shape and size of the bottom patterns instead of the top perovskite layer. Qu and Song designed a core–shell Au/dual-mesoporous silica/embedding perovskite quantum dots (QDs), which can support resonant surface plasmon–polaritons (SPPs), overlapping both spatially and spectrally with resonances in the $CsPbBr_3$ QDs [264]. The outcoupling between SP oscillations and photonics modes within a wavelength range completely overcomes the loss derived from localized surface plasmons, and finally contributes to a novel application of two-photon-pumped nanolasers.

Whether coupling with photonic crystal cavity or plasmonic cavity, the perovskite-based laser has already made significant achievements in high performance nanolasers. In 2014, Belarouci and co-workers put forward a novel strategy of assembling plasmonic–photonic hybrid cavity coupled nanolasers in conventional semiconductor InAsP system [265]. They created a hybrid photonic–plasmonic nanocavity that exploits the coupling between the LSPR of a bowtie antenna and a photonic mode provided by an active photonic crystal structure. The working principle combines the light harvesting ability of the high-Q dielectric microcavity with the extraordinary confining properties of the plasmonic element. Through optical characterization and simulation, this hybrid mode was proved to preserve the spectral feature of the photonic crystal mode and allows for laser emission at room temperature together with a strong reduction in mode volume induced by the presence of the plasmonic building block. Although presently it is still challenging to successfully achieve perovskite-based nanolaser coupling with photonic crystal–plasmonic hybrid cavity (proposed illustration in Fig. 28) due to the limitation in the fabrication and top-down patterning technique on perovskite, we believe this hybrid cavity will provide a promising platform in the near future for novel high-performance perovskites nanolasers.

6.5. Waveguides and light modulators

A waveguide is a device that can guide, propagate and transfer electromagnetic waves, which requires energy loss be minimized. Generally, two kinds of optical waveguides are usually considered, *i.e.*, the silica-based passive waveguide and a luminescent material based active waveguide. Due to the high PLQY efficiency, large Stokes shift and chemically tunable light emission, perovskites are undoubtedly considered as an outstanding candidate for the fabrication of high-performance active waveguides. In 2016, Wang et al. designed an active waveguide based on polycrystalline perovskite microwires, with a small propagation loss of about 0.30 dB μm^{-1} (Fig. 29a) [28]. Composition engineering with different halogen elements enables the channeling of different colors in the waveguide. In addition, in a highly-uniform monocrystalline perovskite nanowire, the optical field is well-confined inside the cavity, further creating a WGM waveguide. It is noteworthy that the corresponding propagation loss is estimated to be roughly 0.04 dB μm^{-1} for a propagation distance of 100 μm, which is much better than that in polycrystalline perovskite nanowires and other traditional semiconductor nanowires (Fig. 29b) [27]. Interestingly,

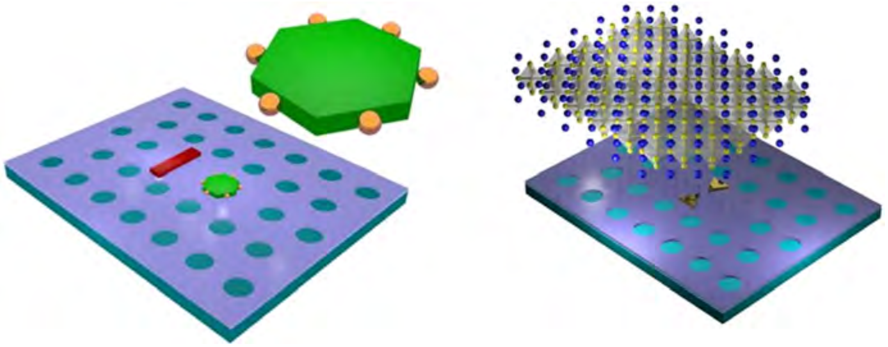

Fig. 28. Schematic diagram of perovskite plasmonic–photonic crystal hybrid cavity coupled nanolasers.

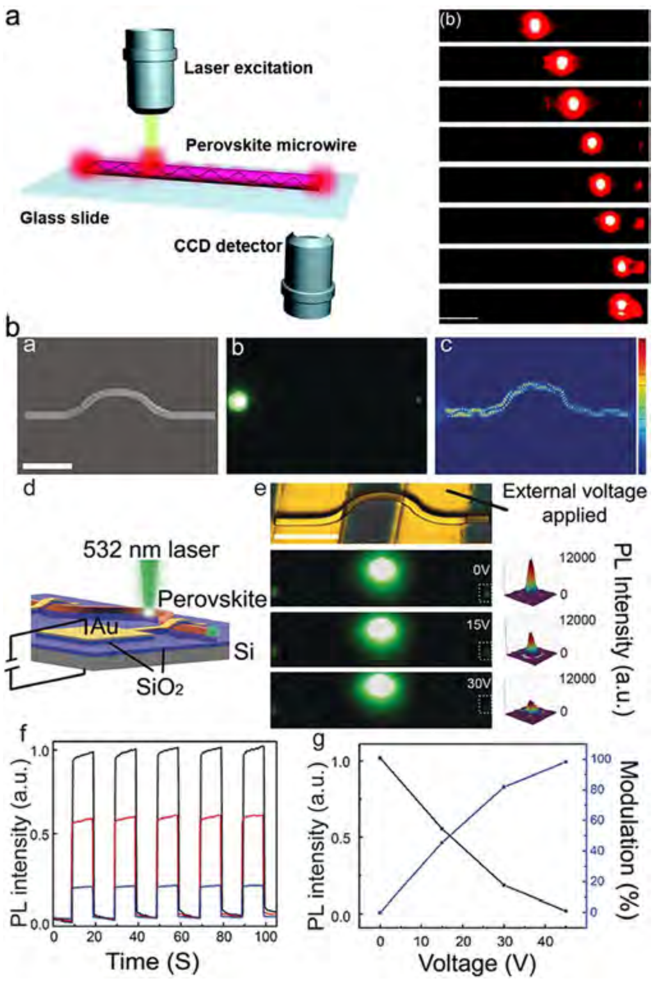

Fig. 29. (a) Schematic and a set of dark-field images of polycrystalline perovskite nanowire based waveguide [28]. Copyright 2016, the Royal Society of Chemistry. (b) Electro-optical modulator devices using an arc waveguide [27]. Copyright 2017, Wiley.

the out-coupled light intensity from the nanowires (both polycrystalline and monocrystalline perovskite) can be effectively modulated by applying an external electric field, thus behaving as a light intensity modulator, which provides an opportunity for applications in micro/nanoscale photonic circuits. The electro-optic modulation mechanism in perovskites (so-called active mode) differs from that in traditional semiconductors such as GaAs, $LiNbO_3$ (passive mode). The electro-optic effect

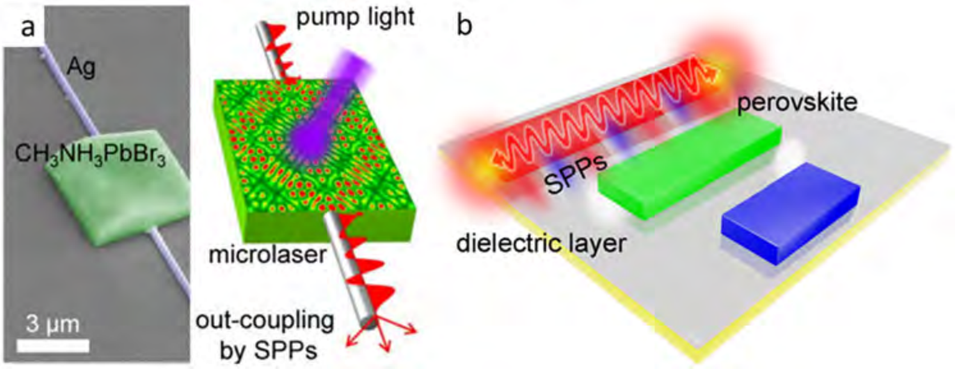

Fig. 30. (a) SEM image and schematic illustration of an embedded dielectric/metal heterostructure for the plasmonic output of a dielectric laser [250]. Copyright 2016, the American Chemical Society. (b) Schematic of the hybrid optical waveguide, consisting of a perovskite nanowire separated from a metal surface by a nanoscale dielectric gap.

in GaAs/$LiNbO_3$ is the change in the refractive index, and by extension the phase of the coherent optical field, resulting from the application of a voltage. By contrast, in the perovskite-based intensity modulators, a feasible exciton splitting at room temperature caused by their low exciton binding energy and ion migration upon applying an electric field are key factors in the phenomenon of PL emission modulation [27]. Reversible ions migration in perovskites also affects the reflective index, quantum efficiency, light-harvesting, and photoelectric properties [266].

Coupling a plasmon and a cavity into a perovskite-based waveguides yields novel optical modulators due to the multiple interactions between SP and perovskite. Zhao and his colleagues showed nanoscale output from a dielectric laser via photo-plasmon coupling in rationally designed $CH_3NH_3PbBr_3$/Ag hybrid heterostructure [250]. In this structure, $CH_3NH_3PbBr_3$ functions as a high-Q cavity and a perfect gain medium for low-threshold lasing, while the embedded Ag NWs produces lasing modes efficiently in the form of SPs. Combining the advantages of the optical gain and the SP effects, the resonant modes of the perovskite micro-cavities (*e.g.*, F–P mode and W-G mode) can be efficiently utilized in modulating the laser output (Fig. 30a). Moreover, through a simple solution-processed precipitation method, Wang et al. prepared a waveguide connected perovskite microdisks [267]. The total internal reflection at the joint is broken, and unidirectional lasing emission from the perovskite microdisk was reported for the first time. Unlike the conventional polygon shaped microdisks with multiple directional outputs in free space, the unidirectional output is well confined within the waveguide.

Recent research exhibits significant potential for perovskite-based waveguides, but there is still much work to be done. Undoubtedly, we can obtain some insights from prior research reports based on traditional semiconductor waveguides. For instance, Zhang and co-workers reported a hybrid optical waveguide consisting of a dielectric nanowire separated from a metal surface by a nanoscale dielectric gap [268]. Effective sub-wavelength transmission in non-metallic regions is allowed in this structure due to 'capacitor-like' energy storage, driven from the coupling between the plasmonic and the waveguide modes across the gap. In this way, SPPs can travel over long distances (40–150 μm) with strong mode confinement (ranging from $\lambda/400$ to $\lambda/40$), enabling integration of high gain semiconductor materials and plasmonics. This integration could lead to the implementation of waveguide loss compensation techniques. In this regard, perovskite as a high gain material can completely replace GaAs [268], which could also facilitate low-loss deep-subwavelength light transport (Fig. 30b). In addition, chemically tunable light emission from the perovskite should provide greater choices for controlled deep-subwavelength light transfer, which may serve as effective building blocks for micro-/nanoscale photonic circuits.

6.6. *Nonlinear photonics devices*

As an outstanding optical material, organic–inorganic hybrid and all-inorganic perovskites have shown great potential in many fields, as was mentioned above. Until now, most optical applications of these materials discussed so far, utilize linear optical interactions. However, perovskites also exhibit promising nonlinear optical properties [269–272]. Sargent's group firstly reported two-photon absorption (TPA) in a $CH_3NH_3PbBr_3$ single crystal, and found that the nonlinear absorption coefficient is around 8.6 cm GW^{-1}(Fig. 31) [269]. In the same year, Wang et al. studied the TPA properties of the all-inorganic perovskite $CsPbBr_3$, and they observed strong nonlinear absorption and emission, with TPA cross-section as high as 1.2×10^5 GM and nonlinear absorption coefficient of around 0.097 cm GW^{-1} [271]. Subsequent studies by Wei et al. further demonstrated that the PL spectrum related with this TPA process shows a linear blue-shift (around 0.32 meV K^{-1}) below the temperature of 220 K [273]. At higher temperatures, PL peak remained nearly unchanged and showed temperature-independent chromaticity up to 380 K. Under the appropriate optical excitation, TPA-induced lasing action can also be observed in perovskites, *e.g.*, periodic peaks around 546 nm were observed from $CH_3NH_3PbBr_3$ microwires under excitation at 800 nm [274]. The Q-factors of two-photon pumped micro-lasers were ∼682, and the corresponding thresholds were

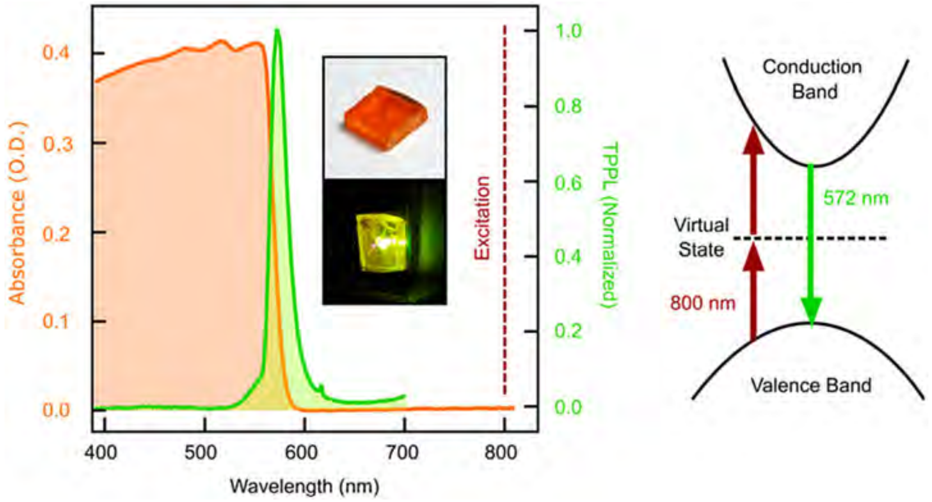

Fig. 31. Linear optical absorbance (left axis) and normalized two-photon-induced photoluminescence (TPPL, right axis) as a function of wavelength for a single $CH_3NH_3PbBr_3$ crystal). Schematic figures showing two-photon absorption of 800 nm light and up conversion to produce 572 nm photoluminescence [269]. Copyright 2015, the American Chemical Society.

ca. 674 μJ cm^{-2}, both of which are comparable to conventional whispering-gallery modes in two-dimensional polygon micro-plates. Moreover, perovskites are useful in many other important nonlinear optical applications, including stimulated emission pumped by three-[275,276], five- and even six-photon absorption [277,278], saturable absorption for mode-locking ytterbium fiber lasers [279], and the Rashba effect [280].

In spite of the demonstrated nonlinear optical properties of perovskites, some unresolved issues still existed. For example, the TPA threshold is obviously higher than that of single-photon absorption. Coupling between SPR and a perovskite optical cavity are effective for further improving the nonlinear optical properties of perovskites. To demonstrate this, a device consisting of disordered gold nanorods (NRs) underneath a $CsPbBr_3$ film was successfully designed by Liu et al. [281]. In this structure, the enhanced scattering cross section due to the far-field effect of the gold NRs greatly increased the emission transition rate of excitons in $CsPbBr_3$, which finally results in low-threshold lasing (ca. 0.65 mJ cm^{-2}).

1D microwires (MWs) and 2D square microplates (MPs) of $CH_3NH_3PbBr_3$ synthesized in a controlled way by Zhang et al. also exhibited large two-photon emission efficiency, followed by low-threshold two-photon pumped lasing as shown in Fig. 32 [104]. Moreover, when the $CH_3NH_3PbBr_3$ NWs were pumped uniformly with a near-infrared pulse laser beam (900 nm, 150 fs), bright up-converted green emission (545 nm) at the ends of the NWs was observed, indicating a strong TPA-induced PL property similar to the FP-type microcavity effect. Similar experiments focused on improving the TPA-induced PL were also conducted in a 2D perovskite microsphere hybrid dielectric structure, shown in Fig. 33a-c [282]. Interestingly, the microspheres in a hybrid dielectric structure can concentrate pumped laser light in a specific area with a radius of ca. 0.3 μm. An optical intensity enhancement factor can be defined as $F_E = I_f/I_0$, where I_f and I_0 are the average optical intensities in the focal spot area for the hybrid dielectric structure and the bare perovskite, respectively. The optical intensity enhancement factor in the microsphere/hybrid dielectric structure was found to be $F_E = 4.7$. Moreover, TPA-induced PL detection efficiency was also improved in this structure, originating from the emission coupled into the microsphere that was subsequently redirected to the objective. The detection efficiency enhancement factor is calculated to be ca. $F_E = 4.3$. As emerging hot research, there are still many interesting points regarding coupling between SPR, optical cavity and nonlinear perovskites that should be studied further.

To improve nonlinear photon conversion, a plasmonic cavity will greatly enhancement. Second-harmonic generation (SHG) and third-harmonic generation (THG) properties of the perovskite structure have also been studied. Yang and co-workers reported that a sub-20 nm wide Au grating produced 7000-fold SHG enhancement for single-layer TMDs [283]. Because it is a one-dimensional grating, the lateral gap plasmon is selectively excited to dynamically control the SHG amplitude only under the special rotating laser polarization. Changing the one-dimensional grating to a coaxial grating will achieve a uniform excitation SHG without polarization dependence, as shown in Fig. 33d. Aouani et al. put forward a new strategy of third-harmonic-upconversion enhancement from a single semiconductor nanoparticle coupled to a plasmonic cavity [284]. They introduced and experimentally emphasized the feasibility of a nanoscale up-conversion system based on a single nonlinear nanoparticle decorated in a plasmon cavity. The composite cavities provide up to 10^6 times enhancement of the nonlinear up-conversion efficiency compared to that for isolated nanoparticles. Although the plasmon cavities they introduce have narrowband resonances, tunable third harmonic upconversion nanosystems can be realized by implementing perovskite nanomaterials in the gap of a broadband plasmon cavity design (Fig. 33e).

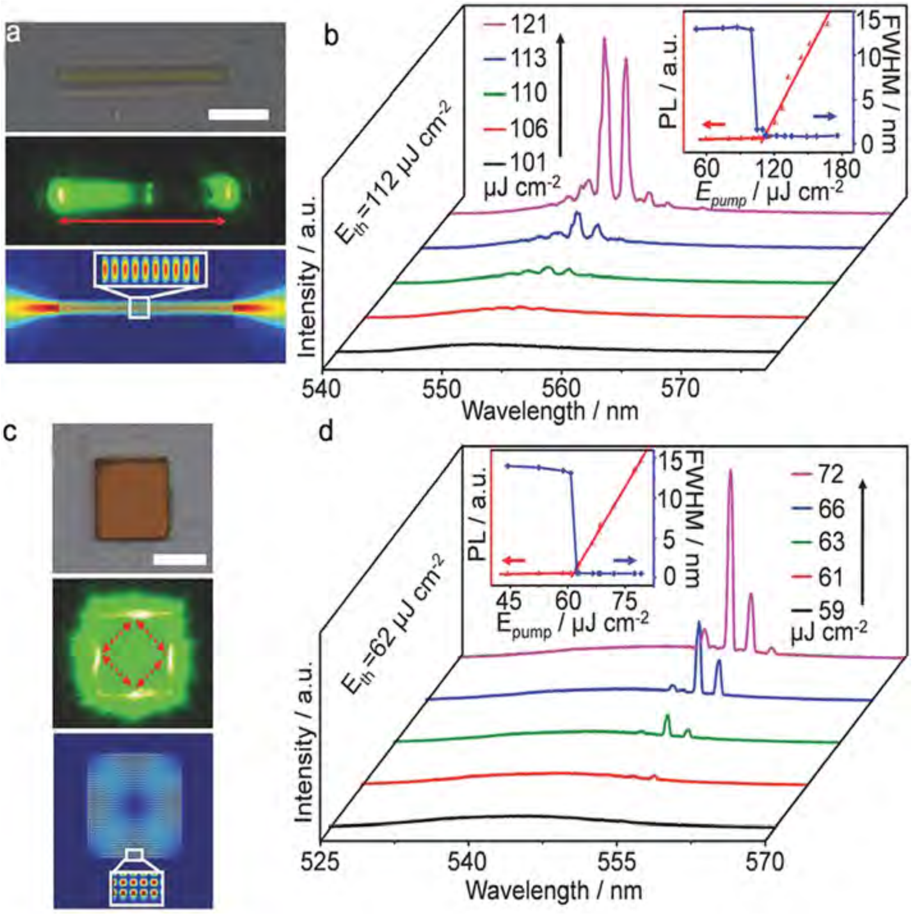

Fig. 32. Two-photon pumped perovskite microcavity lasers. (a) Bright-field (up) and PL(middle) images of a single wire (L = 13.9 μm) above the thresholds excited uniformly with a pulsed laser (900 nm). Scale bar is 5 μm. Bottom: simulated 2D normalized electric field ($\lambda = 553$ nm, n = 2.19), defining a FP standing-wave cavity mode. (b) Power dependence profiles of the PL intensities (red) and FWHM (blue) of the wire around the mode peak 552.9 nm. (c), Bright-field (up) and PL (middle) images of a single plate (L = 6.5 μm) above the thresholds excited uniformly with a pulsed laser (900 nm). Scale bar is 5 μm. Bottom: simulated 2Dnormalized electric field ($\lambda = 552$ nm, n = 2.19), showing a WGM traveling-wave cavity mode. (d) Power dependence profiles of PL intensities (red) and FWHM (blue) of the plate around the mode peak 552.3 nm [104]. Copyright 2016, Wiley.

7. Conclusions and outlook

7.1. Conclusions

In the past few years, there has been tremendous progress in understanding the chemistry of metal-halide perovskites and their applications mainly in thin-film solar cells. The significance of photonics and optoelectronics in low-dimensional perovskites has already been recognized for nanophotonics applications. However, the nanostructured perovskite materials integrated with optical cavities still remain to be an intriguing yet less-investigated topic.

In this review, we have comprehensively summarized recent advances in the fabrication of nanostructured perovskite media and provided a critical discussion of the combination of a variety of photonic cavities with the intrinsic optical properties of perovskites. Specifically, the unique optical properties of metal-halide perovskites are discussed, showing ultralong carrier lifetime, tunable exciton binding energy, outstanding nonlinear optical gain, *etc*. These optical advantages compared with conventional semiconductors, make halide perovskites a competitive optical media for their integration with optical cavities.

The methods of engineering the interactions between perovskites and various cavities have been reviewed in terms of photonic resonances and plasmonic enhancement. Among these two kinds of optical coupling, photonic resonant cavities are commonly employed to modulate the optical path through the perovskite media and thus the density of optical states. However, the plasmonic effect on perovskites generally works not only through light scattering, but also by inducing a local or nonlocal electric field from localized surface plasmonic resonances (LSPRs) or propagating surface plasmon polaritons (SPPs), which could, therefore, influence the carrier recombination and relaxation dynamics in perovskite semiconductors.

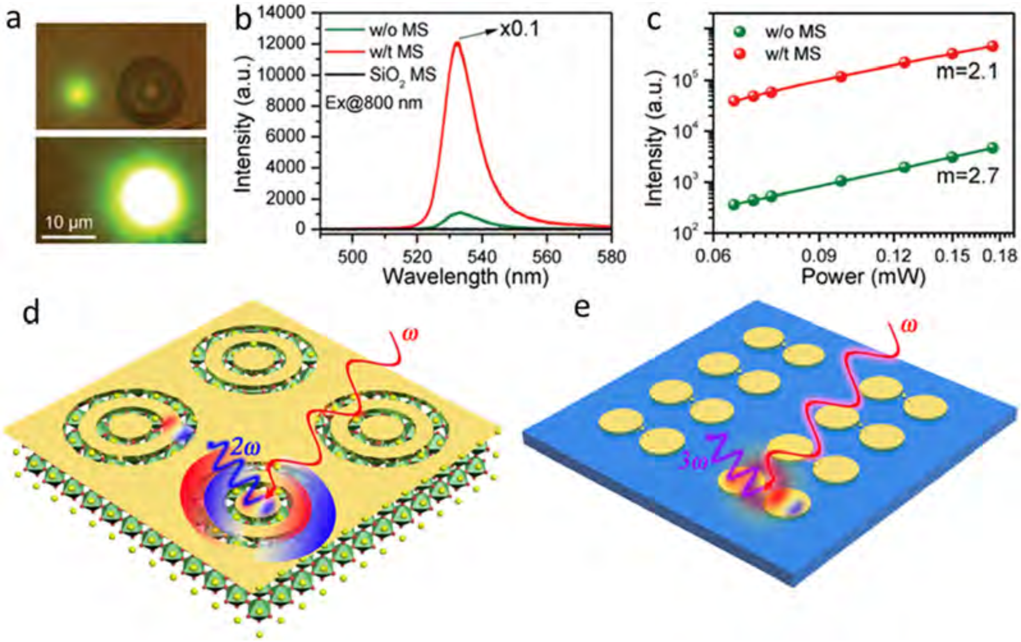

Fig. 33. (a) TPL images of the perovskite flake without (top panel) and with (bottom panel) SiO_2 microsphere under an excitation power of 0.1 mW, respectively. (b) TPL spectra for a bare perovskite flake (w/o MS, green curve) and a perovskite-microsphere hybrid dielectric structure (w/t MS, red curve). The SiO_2 microsphere shows no emission within this waveband (black curve). (c) Double-logarithmic representation of the power-dependent TPL intensity for the bare perovskite flake (without MS, green dots) and perovskite-microsphere hybrid dielectric structure (w/t MS, red dots) [282]. Copyright 2018, Wiley. (d) coaxial plasmon grating uniform excitation SHG without polarization dependence on perovskites. (e) third-harmonic-upconversion enhancement from perovskite nanoparticles coupled to plasmonic cavities.

We conclude that the nanostructured hybrid perovskite media and their optical cavities provide a feasible strategy to tune the optical properties of perovskites and their excitation dynamics, so as to realize enhanced light–matter interactions towards various optoelectronic and photonic applications based on perovskites. The optoelectronic devices based on perovskite photonic structures exhibit band-tunable light detection in photodetectors, improving light absorption in solar cells and enhancing light emission in light-emitting diodes and displays. Similarly, the nanostructured perovskite photonic devices demonstrate potentials in achieving stimulated emission with low threshold in nanolasers, controllable light guiding and propagation in waveguides and modulators, as well as for high gain in nonlinear optical devices.

7.2. Outlook

This section describes existing challenges that need to be addressed to advance the applications of perovskites. It concludes with subjective discussions of new opportunities for perovskite science and technology.

Challenges to address

For practical applications of perovskite photonic structures, the critical issues in metal-halide perovskites themselves need to be addressed properly, such as stability and toxicity. The tunability of the optical bandgap of halide perovskites relies on the composition substitution, which inevitably incurs halide segregation upon light illumination or ion migration under the action of an electric field. This would affect the local defect levels and local optical properties in perovskite crystals. Especially for organic–inorganic hybrid perovskites (*e.g.*, methylammonium lead iodide perovskite) having unprecedented optical and electrical properties, the material instability and severe ion migration are always criticized as a bottleneck. Recently, 2D organic–inorganic hybrid perovskites have shown suppressed ion migration and enhanced stability despite relatively low power conversion efficiency. Fully inorganic perovskites exhibit superior stability, as expected, without significant ion migration, but again their physical performance is not comparable to 3D organic–inorganic hybrid perovskites. We believe that partial substitution of 3D hybrid perovskites with inorganic cations and long-chain organic molecules provides a solution to simultaneously attain stabilized bandgap, high efficiency, and long lifetime.

The toxicity issue seems more intractable, since the lead element is much indispensable for the ultrahigh absorption coefficient, which enables the power conversion efficiency of perovskite solar cells to exceed conventional silicon cells. Several lead-free perovskite solar cells have shown poor device performance in both efficiency and stability. Partial substitution of lead with other metals yielded relatively high-performance perovskite solar cells, but lead is still there. Nevertheless, the understanding of lead halide perovskites may lead to potential alternatives in the form of the perovskite structure. Fortunately, high optical absorption is merely one parameter, yet not always required in photonic applications. For instance, perovskite materials with moderate light absorption properties can be applied in waveguides and optical modulators. Application of passive perovskite waveguides, even does not need the capability of light absorption, only designed geometry. In this regard, lead-free perovskites with appropriate optical constant and bandgap could find their distinctive use in photonic devices.

Perovskite coupled optical cavities require low loss in terms of both photons and electrons, along with sustainable output. For the perovskite coupled photonic cavity, defect-free geometries particularly at the surfaces and edges are quite important for sufficient photon recycling in F–P and WGM cavities. The optical constant of halide perovskites can also be tuned by compositional engineering for maximal total internal reflection, while maintaining the emission color. In addition, highly confined light in the nanoscale perovskite layers produces light concentration and heat, affecting the stability of both perovskite crystals and their photonic performance. Therefore, the design of geometrically suitable and highly efficient photonic cavities is needed to realize enhanced light trapping or low-threshold lasing at minimal pumping light intensity.

For the perovskite coupled plasmonic cavity, electron loss channels from perovskite to metallic nanostructures, and unwanted light scattering loss need to be suppressed. Suitable dielectric materials should be inserted with optimal spacing between perovskite and plasmonic structures in order to minimize the charge trapping in metallic nanostructures while retaining the plasmonic field. Another aspect regarding perovskite-plasmonic cavity is that the plasmonic resonance usually has a limited wavelength range, which may not match the broadband light response of perovskites. How to achieve broadband plasmonic enhancement should be one of the research focuses on perovskite-plasmonic cavities. Apart from the metallic nanostructure induced plasmonic enhancement for a perovskite cavity, achieving intrinsic plasmonic resonance in perovskite nanocrystals, which has not been explored in perovskite research so far, should also be one interesting future research direction. Similar to the near infrared plasmonic resonance in metal oxides, sulfides and phosphides, we envision that perovskite nanocrystals with designed composition would also exhibit plasmonic resonance due to heavily doping, which may bring new opportunities for perovskite plasmonics as discussed below.

The requirements for device integration of perovskite photonic structures further involve stability under relevant electron or photon injection conditions. While the lifetime of thin-film perovskite optoelectronic devices is being gradually extended, there are additional mechanisms of device degradation including both nanostructured perovskites and their interfaces that require in-depth investigation. In addition, the nanofabrication of the perovskite photonic structures and devices should be damage-free to the perovskites, low-loss upon cavity integration and scalable for real-life manufacturing. We anticipate our understanding and perspectives of the nanostructured perovskite media and their optical cavities would lead to a revolutionary platform of enhanced light–matter interaction for perovskite photonics and optoelectronics.

New opportunities

1. Multiscale modeling and materials informatics guided design of perovskites

Modeling guided design can play a major role in the development of new generation perovskites, which are a truly multivariate system, by optimizing the composition, structure and interfaces for specific photonic or optoelectronic function. A new direction is integration of multiscale modeling combined with the emerging approach of materials informatics. Multiscale modeling, in which the 2014 Nobel prize was awarded, refers to applying different degrees of sophistication in treating interactions at different length and time scales [285]. As depicted in Fig. 34, local interactions involving 100–1000 atoms in a heterogeneous media are treated purely quantum mechanically (QM), beyond which QM becomes computationally very demanding and hence not practical. Thus the region at longer length scale can be treated using molecular mechanics (MM) with parametrized interactions such as atom–atom pair-wise interactions, electrostatic multipole interactions, charge transfer interactions *etc.* As the active mesoscopic medium (such as a nanoparticle) may be embedded in a dielectric host medium (solvent, plastic or glass), this region is treated purely classically by considering it as a dielectric polarizable continuum. A recent development is the Capacitance Molecular Mechanics (CMM) as an extension of the QM/MM approach by introducing a capacitance—polarization force field, for embedding metal surfaces and/or nanostructures in complex environments. In the CMM approach, the heterogeneous MM part is split into metallic and non-metallic parts, assuming a capacitance—polarization model for the electrostatics and polarization of the metallic part (resistance and inductance) and distributed charges for the non-metallic part. Then the optical response is obtained by using the response methodology based on density matrix-based time-dependent density functional theory (TDDFT) in the time domain. The corresponding dipole response in the frequency domain (optical absorption) can be retrieved using the Fourier transformation.

Materials informatics is an emerging field, inspired by bioinformatics, that involves computational, statistical, and machine learning methods to accelerate the discovery and optimization of materials composition, structure and dynamics in a multivariate system in order to achieve optimized desired property. It combines conventional and high-throughput experimentation with conventional and high-throughput computational studies in a machine learning or data analytics framework, utilizing empirical data, physically–chemically based modeling, and statistical modeling or statistical inference to create insights in to materials design that would not be achieved by conventional means. Materials informatics also covers the design of experiments (both physical and computational) to yield maximum information content toward a specified objective, and automation of the process of conducting a sequence of experiments. A combination of multiscale modeling and multifaceted materials informatics yields a powerful tool for achieving the discovery of new perovskite materials with otherwise unavailable combinations of properties and for accelerating the commercialization of new materials or existing material in new application.

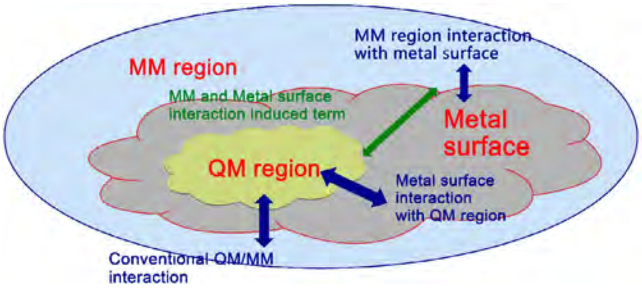

Fig. 34. Coupling of theory levels in multiscale modeling.

2. Epsilon near zero perovskite media

Epsilon near zero materials refer to those in which the real part of the dielectric permittivity, $Re\{\varepsilon\}$, can be tuned across its zero value. Under the right circumstances, this epsilon-near-zero (ENZ) host medium produces gigantic local fields that substantially enhance light–matter interactions. As nonlinear optical effects are depended on higher orders of local friend, the enhancement of nonlinear optical interactions is many fold. Light–matter interactions in epsilon near zero materials is a topic of considerable interest worldwide [286]. Perovskites can be designed by using multiscale modeling and materials informatics, guiding to select appropriate constituents, composition and photonic structure to achieve epsilon near zero in a prescribed spectral window. This aspect of perovskites is virtually unexplored.

3. Semiconductor plasmonics-perovskites

A new area of plasmonics is Plasmonic semiconductors which have free charges such as holes or electrons that in a nanostructure can give rise to plasmonic resonances. These free charges can be readily introduced in a binary or ternary semiconductor by using a nonstoichiometric composition, an example being $Cu_{2-x}S$. As the wavelength of the plasmon resonance is dependent on the concentration of free carries, an advantage of using semiconductor plasmonics is that its wavelength can be compositionally tuned in a binary or ternary semiconductor. It has been shown that in the case of copper sulphide/selenide semiconductor this plasmon resonance can be tuned across 1250 nm in the IR [287]. Perovskites can also be made plasmonic or it can be conjugated to a semiconductor plasmonic structure where the composition tuning of plasmonic band can be used for selective enhancement of photonic properties.

4. Perovskite sensors

Perovskites with their photonic and optoelectronic properties offer unique opportunities for sensing. This application of perovskite media has remained unexplored. A perovskite with photonic structures can serve as an excellent photonic sensor where analyte binding can affect its photonic properties such as optical resonances, fluorescence life time, photonic cavity resonances, *etc*. Perovskites with enhanced optoelectronic properties (photodetectors, LEDs, and solar cells), can serve as an electronic sensor, utilizing a change in their optoelectronic properties for sensing. One can envision gas sensing for environmental monitoring as well as biosensing for in-vitro diagnostics.

Another promising direction is the use of perovskites as sensitive and low-cost hard radiation detectors which offer broad applications in many fields, including medical diagnosis, industrial non-destructive testing, and homeland security. Recently, there have been several reports that perovskites with the high atomic number of Pb can be considered as potential detecting materials that exhibit excellent properties, such as large hard radiation attenuation coefficient, high carrier drift length per unit electric field, and low-cost of fabrication. Hard radiation detectors based on both solution-processed polycrystalline perovskite film and perovskite bulk single crystals have been successfully demonstrated to convert high-energy radiation photons into electrical signals [288–293]. Very recently, Chen et al. described experimental investigation on a series of all-inorganic perovskite nanocrystals-based scintillators that are capable of converting small doses of absorbed X-ray photons into multi-color visible light [294]. These scintillators are different from bulk inorganic scintillators, with the advantages of solution-processability at a relatively low temperature and tunable emission across the visible spectrum by varying the anionic component during synthesis. One promising direction is to use perovskite nanomaterials and nanostructure for realizing flexible and wearable imaging devices with high sensitivity.

5. Perovskite quantum applications

Another emerging promising direction is the application of perovskites for single photon emission and for spintronics, with applications in quantum information processing including quantum key distribution, quantum networks, and photonic quantum computing. Candidate materials with large spin–orbit interactions are of particular interest. Their electrons can be excited with spin-polarized light, which transfers angular momentum and thus builds up spin accumulation, leading to electron occupation in spin-polarized states in the materials. Furthermore, the excited spin-polarized states can be converted into spin-polarized photoluminescence. The investigation of spintronic properties in perovskites has been reported only recently. Perovskites have been demonstrated to exhibit strong spin–orbit coupling [295], spin-dependent optical selection rules [296] and large Rashba splitting [297,298], as well as significant magneto-photocurrent, magneto-electroluminescence and magneto-photoluminescence responses [299,300]. Long et al. demonstrated that spin polarization in perovskites could be controlled through chemical design as well as by magnetic field [301]. They obtained both spin-polarized photon absorption and spin-polarized photoluminescence in reduced-dimensional chiral perovskites through combined strategies of chirality transfer and energy funneling.

A single quantum emitter is also a necessary element for quantum optics and quantum information technologies [302]. For practical applications, compact as well as scalable single-photon sources, which can operate at room temperature, are highly desirable. Recently, Park et al. demonstrated that $CsPbX_3$-based perovskite QDs could serve as room-temperature sources of single photons [303]. Specifically, they observed that emission from individual QDs exhibits strong photon antibunching under both CW and pulsed excitation with time-zero two-photon correlations of $\sim$6% on average.

A scalable integration of quantum devices into integrated quantum networks has so far proven to be rather challenging due to the incompatibility of materials, growth processes, miniaturization, as well as integration of various quantum components with existing mature Si, SiN and CMOS platforms. Considering the facile synthetic techniques of perovskite nanostructures, we can expect to realize the perovskite on-chip integration or fabrication of all perovskite-based on-chip photonic circuits.

Acknowledgments

This study was supported by the Science and Technology Development Fund, China (Nos. 007/2017/A1 and 132/2017/A3), Macao SAR, China, the National Natural Science Foundation of China (NSFC) (61435010, 51702219, 61875138, 51601131), and the Science and Technology Innovation Commission of Shenzhen, China (JCYJ20170818093453105, JCYJ20180206121837007). Financial support at Buffalo by the Air Force Office of Scientific Research, USA, Grant #FA9550-18-1-0042, is also acknowledged. Valuable technical information from Professors Mark Swihart and Alexander Baev at Buffalo is also acknowledged. JWH was supported by U.S. Army RDECOM Acquisition Grant No. W911NF-15-1-0178. This review is dedicated to our co-author, Professor Joseph W. Haus, who unexpectedly passed away on January 11, 2019.

References

[1] M. Gratzel, The light and shade of perovskite solar cells, Nature Mater. 13 (2014) 838–842.
[2] M.A. Green, A. Ho-Baillie, H.J. Snaith, The emergence of perovskite solar cells, Nat. Photon. 8 (2014) 506–514.
[3] G.C. Xing, N. Mathews, S.Y. Sun, S.S. Lim, Y.M. Lam, M. Gratzel, S. Mhaisalkar, T.C. Sum, Long-range balanced electron- and hole-transport lengths in organic-inorganic $CH_3NH_3PbI_3$, Science 342 (2013) 344–347.
[4] B.R. Sutherland, E.H. Sargent, Perovskite photonic sources, Nat. Photon. 10 (2016) 295–302.
[5] G.E. Eperon, S.D. Stranks, C. Menelaou, M.B. Johnston, L.M. Herz, H.J. Snaith, Formamidinium lead trihalide: a broadly tunable perovskite for efficient planar heterojunction solar cells, Energy Environ. Sci. 7 (2014) 982–988.
[6] L.T. Dou, A.B. Wong, Y. Yu, M.L. Lai, N. Kornienko, S.W. Eaton, A. Fu, C.G. Bischak, J. Ma, T.N. Ding, N.S. Ginsberg, L.W. Wang, A.P. Alivisatos, P.D. Yang, Atomically thin two-dimensional organic–inorganic hybrid perovskites, Science 349 (2015) 1518–1521.
[7] J.Y. Liu, Y.Z. Xue, Z.Y. Wang, Z.Q. Xu, C.X. Zheng, B. Weber, J.C. Song, Y.S. Wang, Y.R. Lu, Y.P. Zhang, Q.L. Bao, Two-dimensional $CH_3NH_3PbI_3$ perovskite: Synthesis and optoelectronic application, ACS Nano 10 (2016) 3536–3542.
[8] A. Ng, Z.W. Ren, Q. Shen, S.H. Cheung, H.C. Gokkaya, S.K. So, A.B. Djurisic, Y.Y. Wan, X.J. Wu, C. Surya, Crystal engineering for low defect density and high efficiency hybrid chemical vapor deposition grown perovskite solar cells, ACS Appl. Mater. Interfaces 8 (2016) 32805–32814.
[9] C.C. Stoumpos, C.D. Malliakas, M.G. Kanatzidis, Semiconducting tin and lead iodide perovskites with organic cations: Phase transitions, high mobilities, and near-infrared photoluminescent properties, Inorg. Chem. 52 (2013) 9019–9038.
[10] X.Y. Chin, D. Cortecchia, J. Yin, A. Bruno, C. Soci, Lead iodide perovskite light-emitting field-effect transistor, Nature Commun. 6 (2015) 7383.
[11] F. Li, C. Ma, H. Wang, W.J. Hu, W.L. Yu, A.D. Sheikh, T. Wu, Ambipolar solution-processed hybrid perovskite phototransistors, Nature Commun. 6 (2015) 8238.
[12] Q.F. Dong, Y.J. Fang, Y.C. Shao, P. Mulligan, J. Qiu, L. Cao, J.S. Huang, Electron–hole diffusion lengths $>$175 um in solution-grown $CH_3NH_3PbI_3$ single crystals, Science 347 (2015) 967–970.
[13] S.D. Stranks, G.E. Eperon, G. Grancini, C. Menelaou, M.J.P. Alcocer, T. Leijtens, L.M. Herz, A. Petrozza, H.J. Snaith, Electron-hole diffusion lengths exceeding 1 micrometer in an organometal trihalide perovskite absorber, Science 342 (2013) 341–344.
[14] Q.D. Ou, Y.P. Zhang, Z.Y. Wang, J.A. Yuwono, R.B. Wang, Z.G. Dai, W. Li, C.X. Zheng, Z.Q. Xu, X. Qi, S. Duhm, N.V. Medhekar, H. Zhang, Q.L. Bao, Strong depletion in hybrid perovskite p-n junctions induced by local electronic doping, Adv. Mater. 30 (2018) 1705792.
[15] J.P. Correa-Baena, A. Abate, M. Saliba, W. Tress, T.J. Jacobsson, M. Gratzel, A. Hagfeldt, The rapid evolution of highly efficient perovskite solar cells, Energy Environ. Sci. 10 (2017) 710–727.
[16] A. Kojima, K. Teshima, Y. Shirai, T. Miyasaka, Organometal halide perovskites as visible-light sensitizers for photovoltaic cells, J. Am. Chem. Soc. 131 (2009) 6050–6051.
[17] Y. Zhang, B. Cao, B. Zhang, X. Qi, C. Pan, The production of nitrogen-doped graphene from mixed amine plus ethanol flames, Thin Solid Films 520 (2012) 6850–6855.
[18] X.L. Yang, X.W. Zhang, J.X. Deng, Z.M. Chu, Q. Jiang, J.H. Meng, P.Y. Wang, L.Q. Zhang, Z.G. Yin, J.B. You, Efficient green light-emitting diodes based on quasi-two-dimensional composition and phase engineered perovskite with surface passivation, Nature Commun. 9 (2018) 570.
[19] J. Feng, C. Gong, H. Gao, W. Wen, Y. Gong, X. Jiang, B. Zhang, Y. Wu, Y. Wu, H. Fu, L. Jiang, X. Zhang, Single-crystalline layered metal-halide perovskite nanowires for ultrasensitive photodetectors, Nat. Electron. 1 (2018) 404–410.
[20] P.N. Prasad, Nanophotonics, Wiley, 2004.
[21] J.W. Haus, Fundamentals and Applications of Nanophotonics, Elsevier, Science, 2016.
[22] S. Makarov, A. Furasova, E. Tiguntseva, A. Hemmetter, A. Berestennikov, A. Pushkarev, A. Zakhidov, Y. Kivshar, Halide-perovskite resonant nanophotonics, Adv. Opt. Mater. 7 (2019) 1800784.
[23] C.X. Huo, B. Cai, Z. Yuan, B.W. Ma, H.B. Zeng, Two-dimensional metal halide perovskites: Theory, synthesis, and optoelectronics, Small Methods 1 (2017) 1600018.

[24] E.Z. Shi, Y. Gao, B.P. Finkenauer, Akriti, A.H. Coffey, L.T. Dou, Two-dimensional halide perovskite nanomaterials and heterostructures, Chem. Soc. Rev. 47 (2018) 6046–6072.
[25] L. Polavarapu, B. Nickel, J. Feldmann, A.S. Urban, Advances in quantum-confined perovskite nanocrystals for optoelectronics, Adv. Energy Mater. 7 (2017) 1700267.
[26] X. Qi, Y.P. Zhang, Q.D. Ou, S.T. Ha, C.W. Qiu, H. Zhang, Y.B. Cheng, Q.H. Xiong, Q.L. Bao, Photonics and optoelectronics of 2d metal-halide perovskites, Small 14 (2018) 1800682.
[27] W.X. Mao, J.L. Zheng, Y.P. Zhang, A.S.R. Chesman, Q.D. Ou, J. Hicks, F. Li, Z.Y. Wang, B. Graystone, T.D.M. Bell, M.U. Rothmann, N.W. Duffy, L. Spiccia, Y.B. Cheng, Q.L. Bao, U. Bach, Controlled growth of monocrystalline organo-lead halide perovskite and its application in photonic devices, Angew. Chem., Int. Ed. Engl. 56 (2017) 12486–12491.
[28] Z.Y. Wang, J.Y. Liu, Z.Q. Xu, Y.Z. Xue, L.C. Jiang, J.C. Song, F.Z. Huang, Y.S. Wang, Y.L. Zhong, Y.P. Zhang, Y.B. Cheng, Q.L. Bao, Wavelength-tunable waveguides based on polycrystalline organic–inorganic perovskite microwires, Nanoscale 8 (2016) 6258–6264.
[29] H.M. Zhu, Y.P. Fu, F. Meng, X.X. Wu, Z.Z. Gong, Q. Ding, M.V. Gustafsson, M.T. Trinh, S. Jin, X.Y. Zhu, Lead halide perovskite nanowire lasers with low lasing thresholds and high quality factors, Nature Mater. 14 (2015) 636–642.
[30] Q. Zhang, S.T. Ha, X.F. Liu, T.C. Sum, Q.H. Xiong, Room-temperature near-infrared high-q perovskite whispering-gallery planar nano lasers, Nano Lett. 14 (2014) 5995–6001.
[31] J.G. Feng, X.X. Yan, Y.F. Zhang, X.D. Wang, Y.C. Wu, B. Su, H.B. Fu, L. Jiang, Liquid knife to fabricate patterning single-crystalline perovskite microplates toward high-performance laser arrays, Adv. Mater. 28 (2016) 3732–3741.
[32] Y. Wang, P. Wang, X. Zhou, C. Li, H.Z. Li, X.T. Hu, F.Y. Li, X.P. Liu, M.Z. Li, Y.L. Song, Diffraction-grated perovskite induced highly efficient solar cells through nanophotonic light trapping, Adv. Energy Mater. 8 (2018) 1702960.
[33] J. Mao, W.E.I. Sha, H. Zhang, X.G. Ren, J.Q. Zhuang, V.A.L. Roy, K.S. Wong, W.C.H. Choy, Novel direct nanopatterning approach to fabricate periodically nanostructured perovskite for optoelectronic applications, Adv. Funct. Mater. 27 (2017) 1606525.
[34] R. Su, C. Diederichs, J. Wang, T.C.H. Liew, J.X. Zhao, S. Liu, W.G. Xu, Z.H. Chen, Q.H. Xiong, Room-temperature polariton lasing in all-inorganic perovskite nanoplatelets, Nano Lett. 17 (2017) 3982–3988.
[35] Y.F. Jia, R.A. Kerner, A.J. Grede, B.P. Rand, N.C. Giebink, Continuous-wave lasing in an organic–inorganic lead halide perovskite semiconductor, Nat. Photon. 11 (2017) 784–788.
[36] S.T. Chen, K. Roh, J. Lee, W.K. Chong, Y. Lu, N. Mathews, T.C. Sum, A. Nurmikko, A photonic crystal laser from solution based organo-lead iodide perovskite thin films, ACS Nano 10 (2016) 3959–3967.
[37] H.A. Atwater, A. Polman, Plasmonics for improved photovoltaic devices, Nature Mater. 9 (2010) 205–213.
[38] W. Qiao, W.B. Huang, Y.H. Liu, X.M. Li, L.S. Chen, J.X. Tang, Toward scalable flexible nanomanufacturing for photonic structures and devices, Adv. Mater. 28 (2016) 10353–10380.
[39] J.C. Song, L. Zhang, Y.Z. Xue, Q.Y.S. Wu, F. Xia, C. Zhang, Y.L. Zhong, Y.P. Zhang, J.H. Teng, M. Premaratne, C.W. Qiu, Q.L. Bao, Efficient excitation of multiple plasmonic modes on three-dimensional graphene: An unexplored dimension, ACS Photon. 3 (2016) 1986–1992.
[40] G. Kakavelakis, K. Petridis, E. Kymakis, Recent advances in plasmonic metal and rare-earth-element upconversion nanoparticle doped perovskite solar cells, J. Mater. Chem. A 5 (2017) 21604–21624.
[41] Z.F. Shi, Y. Li, S. Li, X.J. Li, D. Wu, T.T. Xu, Y.T. Tian, Y.S. Chen, Y.T. Zhang, B.L. Zhang, C.X. Shan, G.T. Du, Localized surface plasmon enhanced all-inorganic perovskite quantum dot light-emitting diodes based on coaxial core/shell heterojunction architecture, Adv. Funct. Mater. 28 (2018) 1707031.
[42] Q.Y. Shang, S. Zhang, Z. Liu, J. Chen, P.F. Yang, C. Li, W. Li, Y.F. Zhang, Q.H. Xiong, X.F. Liu, Q. Zhang, Surface plasmon enhanced strong exciton-photon coupling in hybrid inorganic-organic perovskite nanowires, Nano Lett. 18 (2018) 3335–3343.
[43] Y.P. Zhang, J.Y. Liu, Z.Y. Wang, Y.Z. Xue, Q.D. Ou, L. Polavarapu, J.L. Zheng, X. Qi, Q.L. Bao, Synthesis, properties, and optical applications of low-dimensional perovskites, Chem. Commun. 52 (2016) 13637–13655.
[44] J. Cui, C. Chen, J.B. Han, K. Cao, W.J. Zhang, Y. Shen, M.K. Wang, Surface plasmon resonance effect in inverted perovskite solar cells, Adv. Sci. 3 (2016) 1500312.
[45] A. Molle, J. Goldberger, M. Houssa, Y. Xu, S.C. Zhang, D. Akinwande, Buckled two-dimensional xene sheets, Nature Mater. 16 (2017) 163–169.
[46] B.W. Du, W.Q. Yang, Q. Jiang, H.Y. Shan, D.Y. Luo, B.W. Li, W.C. Tang, F. Lin, B. Shen, Q.H. Gong, X. Zhu, R. Zhu, Z.Y. Fang, Plasmonic-functionalized broadband perovskite photodetector, Adv. Opt. Mater. 6 (2018) 1701271.
[47] Y. Dong, Y. Gu, Y. Zou, J. Song, L. Xu, J. Li, F. Xue, X. Li, H. Zeng, Improving all-inorganic perovskite photodetectors by preferred orientation and plasmonic effect, Small 12 (2016) 5622–5632.
[48] S.S. Meng, Y.Q. Li, J.X. Tang, Theoretical perspective to light outcoupling and management in perovskite light-emitting diodes, Org. Electron. 61 (2018) 351–358.
[49] I. Borriello, G. Cantele, D. Ninno, Ab initio investigation of hybrid organic–inorganic perovskites based on tin halides, Phys. Rev. B 77 (2008) 235214.
[50] G. Murtaza, I. Ahmad, First principle study of the structural and optoelectronic properties of cubic perovskites $CsPbM_3$ (M=Cl, Br, I), Physica B 406 (2011) 3222–3229.
[51] Z. Xiao, Y. Yan, Progress in theoretical study of metal halide perovskite solar cell materials, Adv. Energy Mater. 7 (2017) 1701136.
[52] E. Mosconi, A. Amat, M.K. Nazeeruddin, M. Gratzel, F. De Angelis, First-principles modeling of mixed halide organometal perovskites for photovoltaic applications, J. Phys. Chem. C 117 (2013) 13902–13913.
[53] C. Kim, T.D. Huan, S. Krishnan, R. Ramprasad, A hybrid organic–inorganic perovskite dataset, Sci. Data 4 (2017) 170057.
[54] Q.A. Akkerman, V. D'Innocenzo, S. Accornero, A. Scarpellini, A. Petrozza, M. Prato, L. Manna, Tuning the optical properties of cesium lead halide perovskite nanocrystals by anion exchange reactions, J. Am. Chem. Soc. 137 (2015) 10276–10281.
[55] M.R. Filip, G.E. Eperon, H.J. Snaith, F. Giustino, Steric engineering of metal-halide perovskites with tunable optical band gaps, Nature Commun. 5 (2014) 5757.
[56] F. Hao, C.C. Stoumpos, D.H. Cao, R.P.H. Chang, M.G. Kanatzidis, Lead-free solid-state organic–inorganic halide perovskite solar cells, Nat. Photon. 8 (2014) 489–494.
[57] N.K. Noel, S.D. Stranks, A. Abate, C. Wehrenfennig, S. Guarnera, A.A. Haghighirad, A. Sadhanala, G.E. Eperon, S.K. Pathak, M.B. Johnston, A. Petrozza, L.M. Herz, H.J. Snaith, Lead-free organic–inorganic tin halide perovskites for photovoltaic applications, Energy Environ. Sci. 7 (2014) 3061–3068.
[58] A. Filippetti, A. Mattoni, Hybrid perovskites for photovoltaics: Insights from first principles, Phys. Rev. B 89 (2014) 125203.
[59] I.B. Koutselas, L. Ducasse, G.C. Papavassiliou, Electronic properties of three- and low-dimensional semiconducting materials with Pb halide and Sn halide units, J. Phys.: Condens. Matter 8 (1996) 1217–1227.
[60] M. Hirasawa, T. Ishihara, T. Goto, K. Uchida, N. Miura, Magnetoabsorption of the lowest exciton in perovskite-type compound $(CH_3NH_3)PbI_3$, Physica B 201 (1994) 427–430.
[61] K. Tanaka, T. Takahashi, T. Ban, T. Kondo, K. Uchida, N. Miura, Comparative study on the excitons in lead-halide-based perovskite-type crystals $CH_3NH_3PbBr_3CH_3NH_3PbI_3$, Solid State Commun. 127 (2003) 619–623.
[62] T. Ishihara, Optical-properties of PBI-based perovskite structures, J. Luminescence 60–1 (1994) 269–274.
[63] S.Y. Sun, T. Salim, N. Mathews, M. Duchamp, C. Boothroyd, G.C. Xing, T.C. Sum, Y.M. Lam, The origin of high efficiency in low-temperature solution-processable bilayer organometal halide hybrid solar cells, Energy Environ. Sci. 7 (2014) 399–407.

[64] T.J. Savenije, C.S. Ponseca, L. Kunneman, M. Abdellah, K.B. Zheng, Y.X. Tian, Q.S. Zhu, S.E. Canton, I.G. Scheblykin, T. Pullerits, A. Yartsev, V. Sundstrom, Thermally activated exciton dissociation and recombination control the carrier dynamics in organometal halide perovskite, J. Phys. Chem. Lett. 5 (2014) 2189–2194.

[65] V. D'Innocenzo, G. Grancini, M.J.P. Alcocer, A.R.S. Kandada, S.D. Stranks, M.M. Lee, G. Lanzani, H.J. Snaith, A. Petrozza, Excitons versus free charges in organo-lead tri-halide perovskites, Nature Commun. 5 (2014) 3586.

[66] W. Zhang, M. Saliba, S.D. Stranks, Y. Sun, X. Shi, U. Wiesner, H.J. Snaith, Enhancement of perovskite-based solar cells employing core-shell metal nanoparticles, Nano Lett. 13 (2013) 4505–4510.

[67] Y. Yamada, T. Nakamura, M. Endo, A. Wakamiya, Y. Kanemitsu, Photoelectronic responses in solution-processed perovskite $CH_3NH_3PbI_3$ solar cells studied by photoluminescence and photoabsorption spectroscopy, IEEE J. Photovoltaics 5 (2015) 401–405.

[68] Q.Q. Lin, A. Armin, R.C.R. Nagiri, P.L. Burn, P. Meredith, Electro-optics of perovskite solar cells, Nat. Photon. 9 (2015) 106–112.

[69] K.M. Ip, C.R. Wang, Q. Li, S.K. Hark, Excitons and surface luminescence of CdS nanoribbons, Appl. Phys. Lett. 84 (2004) 795–797.

[70] M. Hirasawa, T. Ishihara, T. Goto, Exciton features in 0-dimensional, 2-dimensional, and 3-dimensional networks of PBI_6 4- octahedra, J. Phys. Soc. Japan 63 (1994) 3870–3879.

[71] C.S. Ponseca, T.J. Savenije, M. Abdellah, K.B. Zheng, A. Yartsev, T. Pascher, T. Harlang, P. Chabera, T. Pullerits, A. Stepanov, J.P. Wolf, V. Sundstrom, Organometal halide perovskite solar cell materials rationalized: Ultrafast charge generation, high and microsecond-long balanced mobilities, and slow recombination, J. Am. Chem. Soc. 136 (2014) 5189–5192.

[72] A. Marchioro, J. Teuscher, D. Friedrich, M. Kunst, R. van de Krol, T. Moehl, M. Gratzel, J.E. Moser, Unravelling the mechanism of photoinduced charge transfer processes in lead iodide perovskite solar cells, Nat. Photon. 8 (2014) 250–255.

[73] C. Wehrenfennig, G.E. Eperon, M.B. Johnston, H.J. Snaith, L.M. Herz, High charge Carrier mobilities and lifetimes in organolead trihalide perovskites, Adv. Mater. 26 (2014) 1584–1589.

[74] C. Wehrenfennig, M.Z. Liu, H.J. Snaith, M.B. Johnston, L.M. Herz, Charge-carrier dynamics in vapour-deposited films of the organolead halide perovskite $CH_3NH_3PbI_3$-xClx, Energy Environ. Sci. 7 (2014) 2269–2275.

[75] J.S. Manser, P.V. Kamat, Band filling with free charge carriers in organonietal halide perovskites, Nat. Photon. 8 (2014) 737–743.

[76] M. Saba, M. Cadelano, D. Marongiu, F.P. Chen, V. Sarritzu, N. Sestu, C. Figus, M. Aresti, R. Piras, A.G. Lehmann, C. Cannas, A. Musinu, F. Quochi, A. Mura, G. Bongiovanni, Correlated electron–hole plasma in organometal perovskites, Nature Commun. 5 (2014) 5049.

[77] Y. Yamada, T. Nakamura, M. Endo, A. Wakamiya, Y. Kanemitsu, Photocarrier recombination dynamics in perovskite $CH_3NH_3PbI_3$ for solar cell applications, J. Am. Chem. Soc. 136 (2014) 11610–11613.

[78] S.D. Stranks, V.M. Burlakov, T. Leijtens, J.M. Ball, A. Goriely, H.J. Snaith, Recombination kinetics in organic-inorganic perovskites: Excitons, free charge, and subgap states, Phys. Rev. A 2 (2014) 034007.

[79] G.C. Xing, N. Mathews, S.S. Lim, N. Yantara, X.F. Liu, D. Sabba, M. Gratzel, S. Mhaisalkar, T.C. Sum, Low-temperature solution-processed wavelength-tunable perovskites for lasing, Nature Mater. 13 (2014) 476–480.

[80] X. Gong, O. Voznyy, A. Jain, W. Liu, R. Sabatini, Z. Piontkowski, G. Walters, G. Bappi, S. Nokhrin, O. Bushuyev, M. Yuan, R. Comin, D. McCamant, S.O. Kelley, E.H. Sargent, Electron–phonon interaction in efficient perovskite blue emitters, Nature Mater. 17 (2018) 550–556.

[81] N.K. Noel, A. Abate, S.D. Stranks, E.S. Parrott, V.M. Burlakov, A. Goriely, H.J. Snaith, Enhanced photoluminescence and solar cell performance via lewis base passivation of organic inorganic lead halide perovskites, ACS Nano 8 (2014) 9815–9821.

[82] S. Mehraeen, V. Coropceanu, J.L. Bredas, Role of band states and trap states in the electrical properties of organic semiconductors: Hopping versus mobility edge model, Phys. Rev. B 87 (2013) 195209.

[83] K. Willa, R. Hausermann, T. Mathis, A. Facchetti, Z. Chen, B. Batlogg, From organic single crystals to solution processed thin-films: Charge transport and trapping with varying degree of order, J. Appl. Phys. 113 (2013) 133707.

[84] M. Graetzel, R.A.J. Janssen, D.B. Mitzi, E.H. Sargent, Materials interface engineering for solution-processed photovoltaics, Nature 488 (2012) 304–312.

[85] M. De Bastiani, V. D'Innocenzo, S.D. Stranks, H.J. Snaith, A. Petrozza, Role of the crystallization substrate on the photoluminescence properties of organo-lead mixed halides perovskites, APL Mater. 2 (2014) 3623.

[86] K.K. Bass, R.E. McAnally, S.L. Zhou, P.I. Djurovich, M.E. Thompson, B.C. Melot, Influence of moisture on the preparation, crystal structure, and photophysical properties of organohalide perovskites, Chem. Commun. 50 (2014) 15819–15822.

[87] J.B. You, Y.M. Yang, Z.R. Hong, T.B. Song, L. Meng, Y.S. Liu, C.Y. Jiang, H.P. Zhou, W.H. Chang, G. Li, Y. Yang, Moisture assisted perovskite film growth for high performance solar cells, Appl. Phys. Lett. 105 (2014) 183902.

[88] M. Pope, C.E. Swenberg, Electronic Processes in Organic Crystals and Polymers, Oxford University Press, 1999.

[89] R. Kubo, Statistical-mechanical theory of irreversible processes. 1. General theory and simple applications to magnetic and conduction problems, J. Phys. Soc. Japan 12 (1957) 570–586.

[90] P.C. Martin, J. Schwinger, Theory of many-particle systems. 1, Phys. Rev. 115 (1959) 1342–1373.

[91] H. Oga, A. Saeki, Y. Ogomi, S. Hayase, S. Seki, Improved understanding of the electronic and energetic landscapes of perovskite solar cells: High local charge carrier mobility, reduced recombination, and extremely shallow traps, J. Am. Chem. Soc. 136 (2014) 13818–13825.

[92] M.M. Lee, J. Teuscher, T. Miyasaka, T.N. Murakami, H.J. Snaith, Efficient hybrid solar cells based on meso-superstructured organometal halide perovskites, Science 338 (2012) 643–647.

[93] J. Burschka, N. Pellet, S.J. Moon, R. Humphry-Baker, P. Gao, M.K. Nazeeruddin, M. Gratzel, Sequential deposition as a route to high-performance perovskite-sensitized solar cells, Nature 499 (2013) 316.

[94] H.P. Zhou, Q. Chen, G. Li, S. Luo, T.B. Song, H.S. Duan, Z.R. Hong, J.B. You, Y.S. Liu, Y. Yang, Interface engineering of highly efficient perovskite solar cells, Science 345 (2014) 542–546.

[95] L. Etgar, P. Gao, Z.S. Xue, Q. Peng, A.K. Chandiran, B. Liu, M.K. Nazeeruddin, M. Gratzel, Mesoscopic $CH_3NH_3PbI_3/TiO_2$ heterojunction solar cells, J. Am. Chem. Soc. 134 (2012) 17396–17399.

[96] H. Yu, F. Wang, F.Y. Xie, W.W. Li, J. Chen, N. Zhao, The role of chlorine in the formation process of $CH_3NH_3PbI_3$-xCl(x) perovskite, Adv. Funct. Mater. 24 (2014) 7102–7108.

[97] P.W. Liang, C.C. Chueh, X.K. Xin, F. Zuo, S.T. Williams, C.Y. Liao, A.K.Y. Jen, High-performance planar-heterojunction solar cells based on ternary halide large-band-gap perovskites, Adv. Energy Mater. 5 (2015) 1400960.

[98] S. Bai, Z.W. Wu, X.J. Wu, Y.Z. Jin, N. Zhao, Z.H. Chen, Q.Q. Mei, X.Z. Wang, Z. Ye, T.Y. Song, R.Y. Liu, S.T. Lee, B.Q. Sun, High-performance planar heterojunction perovskite solar cells: Preserving long charge carrier diffusion lengths and interfacial engineering, Nano Res. 7 (2014) 1749–1758.

[99] E.Y. Tiguntseva, D.G. Baranov, A.P. Pushkarev, B. Munkhbat, F. Komissarenko, M. Franckevičius, A.A. Zakhidov, T. Shegai, Y.S. Kivshar, S.V. Makarov, Tunable hybrid Fano resonances in halide perovskite nanoparticles, Nano Lett. 18 (2018) 5522–5529.

[100] E.Y. Tiguntseva, G.P. Zograf, F.E. Komissarenko, D.A. Zuev, A.A. Zakhidov, S.V. Makarov, Y.S. Kivshar, Light-emitting halide perovskite nanoantennas, Nano Lett. 18 (2018) 1185–1190.

[101] C. Zou, C. Dong, J. Cui, F. Sun, Y. Yang, X. Wu, Z. Han, G. Guo, Whispering gallery mode optical microresonators:fundamentals and applications, Sci. Sin. Phys. Mech. Astronom. 42 (2012) 1155–1175.

[102] H.H. Fang, R. Ding, S.Y. Lu, Y.D. Yang, Q.D. Chen, J. Feng, Y.Z. Huang, H.B. Sun, Whispering-gallery mode lasing from patterned molecular single-crystalline microcavity array, Laser Photon. Rev. 7 (2013) 281–288.

[103] F. Chen, C.X. Xu, Q.Y. Xu, Z. Zhu, F.F. Qin, A.G. Manohari, Y.Z. Zhu, Lasing mode evolution and regulation of the perovskite $CH_3NH_3PbBr_3$, J. Mater. Chem. C 5 (2017) 9238–9241.

[104] W. Zhang, L. Peng, J. Liu, A.W. Tang, J.S. Hu, J.N.A. Yao, Y.S. Zhao, Controlling the Cavity structures of two-photon-pumped perovskite microlasers, Adv. Mater. 28 (2016) 4040–4046.

[105] H. Bahsoun, T. Chervy, A. Thomas, K. Borjesson, M. Hertzog, J. George, E. Devaux, C. Genet, J.A. Hutchison, T.W. Ebbesen, Electronic light-matter strong coupling in nanofluidic Fabry–Perot cavities, ACS Photon. 5 (2018) 225–232.

[106] K.Y. Wang, Z.Y. Gu, S. Liu, W.Z. Sun, N. Zhang, S.M. Xiao, Q.H. Song, High-density and uniform lead halide perovskite nanolaser array on silicon, J. Phys. Chem. Lett. 7 (2016) 2549–2555.

[107] H. Zhang, Y. Wu, Q. Liao, Z. Zhang, Y. Liu, Q. Gao, P. Liu, M. Li, J. Yao, H. Fu, A two-dimensional ruddlesden–popper perovskite nanowire laser array based on ultrafast light-harvesting quantum wells, Angew. Chem., Int. Ed. Engl. 57 (2018) 7748–7752.

[108] Y. Mi, Z. Liu, Q. Shang, X. Niu, J. Shi, S. Zhang, J. Chen, W. Du, Z. Wu, R. Wang, X. Qiu, X. Hu, Q. Zhang, T. Wu, X. Liu, Fabry-Pérot oscillation and room temperature lasing in perovskite cube-corner pyramid Cavities, Small 14 (2018) 1703136.

[109] Y.P. Fu, H.M. Zhu, A.W. Schrader, D. Liang, Q. Ding, P. Joshi, L. Hwang, X.Y. Zhu, S. Jin, Nanowire lasers of formamidinium lead halide perovskites and their stabilized alloys with improved stability, Nano Lett. 16 (2016) 1000–1008.

[110] S.W. Eaton, M.L. Lai, N.A. Gibson, A.B. Wong, L.T. Dou, J. Ma, L.W. Wang, S.R. Leone, P.D. Yang, Lasing in robust cesium lead halide perovskite nanowires, Proc. Natl. Acad. Sci. 113 (2016) 1993–1998.

[111] J. Xing, X.F. Liu, Q. Zhang, S.T. Ha, Y.W. Yuan, C. Shen, T.C. Sum, Q.H. Xiong, Vapor phase synthesis of organometal halide perovskite nanowires for tunable room-temperature nanolasers, Nano Lett. 15 (2015) 4571–4577.

[112] S. Gradecak, F. Qian, Y. Li, H.G. Park, C.M. Lieber, Gan nanowire lasers with low lasing thresholds, Appl. Phys. Lett. 87 (2005) 173111.

[113] H. Zhou, S.P. Yuan, X.X. Wang, T. Xu, X. Wang, H.L. Li, W.H. Zheng, P. Fang, Y.Y. Li, L.T. Sun, A.L. Pan, Vapor growth and tunable lasing of band gap engineered cesium lead halide perovskite micro/nanorods with triangular cross section, ACS Nano 11 (2017) 1189–1195.

[114] Y. Mi, Z.X. Liu, Q.Y. Shang, X.X. Niu, J. Shi, S. Zhang, J. Chen, W.N. Du, Z.Y. Wu, R. Wang, X.H. Qiu, X.Y. Hu, Q. Zhang, T. Wu, X.F. Liu, Fabry–Perot oscillation and room temperature lasing in perovskite cube-corner pyramid cavities, Small 14 (2018) 1703136.

[115] X.X. He, P. Liu, H.H. Zhang, Q. Liao, J.N. Yao, H.B. Fu, Patterning multicolored microdisk laser arrays of cesium lead halide perovskite, Adv. Mater. 29 (2017) 1604510.

[116] J.G. Feng, X.Y. Jiang, X.X. Yan, Y.C. Wu, B. Su, H.B. Fu, J.N. Yao, L. Jiang, Capillary-bridge lithography for patterning organic crystals toward mode-tunable microlaser arrays, Adv. Mater. 29 (2017) 1603652.

[117] R. Chen, B. Ling, X.W. Sun, H.D. Sun, Room temperature excitonic whispering gallery mode lasing from high-quality hexagonal ZnO microdisks, Adv. Mater. 23 (2011) 2199.

[118] A.K. Bhowmik, Polygonal optical cavities, Appl. Opt. 39 (2000) 3071–3075.

[119] C. Czekalla, T. Nobis, A. Rahm, B.Q. Cao, J. Zuniga-Perez, C. Sturm, R. Schmidt-Grund, M. Lorenz, M. Grundmann, Whispering gallery modes in zinc oxide micro- and nanowires, Phys. Status Solidi b 247 (2010) 1282–1293.

[120] M. Grundmann, C.P. Dietrich, Whispering gallery modes in deformed hexagonal resonators, Phys. Status Solidi b 249 (2012) 871–879.

[121] F. Sasaki, H. Mochizuki, Y. Zhou, Y. Sonoda, R. Azumi, Optical pumped lasing in solution processed perovskite semiconducting materials: Self-assembled microdisk lasing, Japan J. Appl. Phys. 55 (2016) 04ES02.

[122] A. Rosenberg, M.W. Carter, J.A. Casey, M. Kim, R.T. Holm, R.L. Henry, C.R. Eddy, V.A. Shamamian, K. Bussmann, S. Shi, D.W. Prather, Guided resonances in asymmetrical GaN photonic crystal slabs observed in the visible spectrum, Opt. Express 13 (2005) 6564–6571.

[123] S. Tomljenovic-Hanic, C.M. de Sterke, M.J. Steel, B.J. Eggleton, Y. Tanaka, S. Noda, High-Q cavities in multilayer photonic crystal slabs, Opt. Express 15 (2007) 17248–17253.

[124] O. Kilic, S. Kim, W. Suh, Y.A. Peter, A.S. Sudbo, M.F. Yanik, S.H. Fan, O. Solgaard, Photonic crystal slabs demonstrating strong broadband suppression of transmission in the presence of disorders, Opt. Lett. 29 (2004) 2782–2784.

[125] G.C. Xing, M.H. Kumar, W.K. Chong, X.F. Liu, Y. Cai, H. Ding, M. Asta, M. Gratzel, S. Mhaisalkar, N. Mathews, T.C. Sum, Solution-processed tin-based perovskite for near-infrared lasing, Adv. Mater. 28 (2016) 8191–8196.

[126] S. Schunemann, K. Chen, S. Brittman, E. Garnett, H. Tuysuz, Preparation of organometal halide perovskite photonic crystal films for potential optoelectronic applications, ACS Appl. Mater. Interfaces 8 (2016) 25489–25495.

[127] I.D.W. Samuel, G.A. Turnbull, Organic semiconductor lasers, Chem. Rev. 107 (2007) 1272–1295.

[128] Y. Jia, R.A. Kerner, A.J. Grede, B.P. Rand, N.C. Giebink, Continuous-wave lasing in an organic–inorganic lead halide perovskite semiconductor, Nat. Photon. 11 (2017) 784–788.

[129] K. Chen, S. Schunemann, H. Tuysuz, Preparation of waterproof organometal halide perovskite photonic crystal beads, Angew. Chem., Int. Ed. Engl. 56 (2017) 6548–6552.

[130] M. Saliba, S.M. Wood, J.B. Patel, P.K. Nayak, J. Huang, J.A. Alexander-Webber, B. Wenger, S.D. Stranks, M.T. Horantner, J.T.W. Wang, R.J. Nicholas, L.M. Herz, M.B. Johnston, S.M. Morris, H.J. Snaith, M.K. Riede, Structured organic-inorganic perovskite toward a distributed feedback laser, Adv. Mater. 28 (2016) 923–929.

[131] F. Deschler, M. Price, S. Pathak, L.E. Klintberg, D.D. Jarausch, R. Higler, S. Huttner, T. Leijtens, S.D. Stranks, H.J. Snaith, M. Atature, R.T. Phillips, R.H. Friend, High photoluminescence efficiency and optically pumped lasing in solution-processed mixed halide perovskite semiconductors, J. Phys. Chem. Lett. 5 (2014) 1421–1426.

[132] S.T. Chen, A. Nurmikko, Stable green perovskite vertical-cavity surface-emitting lasers on rigid and flexible substrates, ACS Photon. 4 (2017) 2486–2494.

[133] A. Gharajeh, R. Haroldson, Z.T. Li, J. Moon, B. Balachandran, W. Hu, A. Zakhidov, Q. Gu, Continuous-wave operation in directly patterned perovskite distributed feedback light source at room temperature, Opt. Lett. 43 (2018) 611–614.

[134] H.A. Lorentz, The Theory of Electrons and Its Applications to the Phenomena of Light and Radiant Heat; a Course of Lectures Delivered in Columbia University, New York, in March and 1906, B.G. Teubner; G.E. Stechert & Co., Leipzig, New York, 1909.

[135] M. Scalora, M.A. Vincenti, D. de Ceglia, N. Akozbek, M.J. Bloemer, L. Roso, J. Trull, C. Cojocaru, J.W. Haus, Reevaluation of radiation reaction and consequences for light-matter interactions at the nanoscale, Opt. Express 26 (2018) 18055–18063.

[136] A.D. Rakic, A.B. Djurisic, J.M. Elazar, M.L. Majewski, Optical properties of metallic films for vertical-cavity optoelectronic devices, Appl. Opt. 37 (1998) 5271–5283.

[137] F.J.G. de Abajo, Nonlocal effects in the plasmons of strongly interacting nanoparticles, dimers, and waveguides, J. Phys. Chem. C 112 (2008) 17983–17987.

[138] J.M. McMahon, S.K. Gray, G.C. Schatz, Optical properties of nanowire dimers with a spatially nonlocal dielectric function, Nano Lett. 10 (2010) 3473–3481.

[139] C. Ciraci, R.T. Hill, J.J. Mock, Y. Urzhumov, A.I. Fernandez-Dominguez, S.A. Maier, J.B. Pendry, A. Chilkoti, D.R. Smith, Probing the ultimate limits of plasmonic enhancement, Science 337 (2012) 1072–1074.

[140] Y. Luo, A.I. Fernandez-Dominguez, A. Wiener, S.A. Maier, J.B. Pendry, Surface plasmons and nonlocality: A simple model, Phys. Rev. Lett. 111 (2013) 093901.

[141] M. Scalora, M.A. Vincenti, D. de Ceglia, J.W. Haus, Nonlocal and quantum-tunneling contributions to harmonic generation in nanostructures: Electron-cloud-screening effects, Phys. Rev. A 90 (2014) 013831.
[142] N.A. Mortensen, S. Raza, M. Wubs, T. Sondergaard, S.I. Bozhevolnyi, A generalized non-local optical response theory for plasmonic nanostructures, Nature Commun. 5 (2014) 3809.
[143] J.W. Haus, D. de Ceglia, M.A. Vincenti, M. Scalora, Quantum conductivity for metal–insulator–metal nanostructures, J. Opt. Soc. Am. A 31 (2014) 259–269.
[144] J.W. Haus, D. de Ceglia, M.A. Vincenti, M. Scalora, Nonlinear quantum tunneling effects in nanoplasmonic environments: two-photon absorption and harmonic generation, J. Opt. Soc. Am. B 31 (2014) A13–A19.
[145] M. Kaupp, The role of radial nodes of atomic orbitals for chemical bonding and the periodic table, J. Comput. Chem. 28 (2007) 320–325.
[146] M. Scalora, M.A. Vincenti, D. de Ceglia, C.M. Cojocaru, M. Grande, J.W. Haus, Nonlinear duffing oscillator model for third harmonic generation, J. Opt. Soc. Am. B 32 (2015) 2129–2138.
[147] I. Kriegel, F. Scotognella, L. Manna, Plasmonic doped semiconductor nanocrystals: Properties, fabrication, applications and perspectives, Phys. Rep. 674 (2017) 1–52.
[148] S.Q. Li, P.J. Guo, L.X. Zhang, W. Zhou, T.W. Odom, T. Seideman, J.B. Ketterson, R.P.H. Chang, Infrared plasmonics with indium-tin-oxide nanorod arrays, ACS Nano 5 (2011) 9161–9170.
[149] F.J.G. de Abajo, Graphene plasmonics: Challenges and opportunities, ACS Photon. 1 (2014) 135–152.
[150] J.Y. Ou, J.K. So, G. Adamo, A. Sulaev, L. Wang, N.I. Zheludev, Ultraviolet and visible range plasmonics in the topological insulator Bi1.5Sb0.5Te1.8Se1.2, Nature Commun. 5 (2014) 5139.
[151] Y.H. Jang, Y.J. Jang, S. Kim, L.N. Quan, K. Chung, D.H. Kim, Plasmonic solar cells: From rational design to mechanism overview, Chem. Rev. 116 (2016) 14982–15034.
[152] M.L. Juan, M. Righini, R. Quidant, Plasmon nano-optical tweezers, Nat. Photon. 5 (2011) 349–356.
[153] B. Sharma, R.R. Frontiera, A.I. Henry, E. Ringe, R.P. Van Duyne, SERS: Materials, applications, and the future, Mater. Today 15 (2012) 16–25.
[154] A.J. Haes, C.L. Haynes, A.D. McFarland, G.C. Schatz, R.R. Van Duyne, S.L. Zou, Plasmonic materials for surface-enhanced sensing and spectroscopy, MRS Bull. 30 (2005) 368–375.
[155] H.S. Zhou, I. Honma, H. Komiyama, J.W. Haus, Controlled synthesis and quantum-size effect in gold-coated nanoparticles, Phys. Rev. B 50 (1994) 12052–12056.
[156] J.T. Hugall, A. Singh, N.F. van Hulst, Plasmonic cavity coupling, ACS Photon. 5 (2018) 43–53.
[157] S.C. Warren, E. Thimsen, Plasmonic solar water splitting, Energy Environ. Sci. 5 (2012) 5133–5146.
[158] D.D. Evanoff, G. Chumanov, Synthesis and optical properties of silver nanoparticles and arrays, Chem. Phys. Chem. 6 (2005) 1221–1231.
[159] O.L. Muskens, V. Giannini, J.A. Sanchez-Gil, J.G. Rivas, Optical scattering resonances of single and coupled dimer plasmonic nanoantennas, Opt. Express 15 (2007) 17736–17746.
[160] W.R. Erwin, H.F. Zarick, E.M. Talbert, R. Bardhan, Light trapping in mesoporous solar cells with plasmonic nanostructures, Energy Environ. Sci. 9 (2016) 1577–1601.
[161] P.F. Liao, A. Wokaun, Lightning ROD effect in surface enhanced Raman-scattering, J. Chem. Phys. 76 (1982) 751–752.
[162] Y.Z. He, P. Basnet, S.E.H. Murph, Y.P. Zhao, Ag nanoparticle embedded TiO_2 composite nanorod arrays fabricated by oblique angle deposition: Toward plasmonic photocatalysis, ACS Appl. Mater. Interfaces 5 (2013) 11818–11827.
[163] S.K. Cushing, J.T. Li, F.K. Meng, T.R. Senty, S. Suri, M.J. Zhi, M. Li, A.D. Bristow, N.Q. Wu, Photocatalytic activity enhanced by plasmonic resonant energy transfer from metal to semiconductor, J. Am. Chem. Soc. 134 (2012) 15033–15041.
[164] S. Linic, P. Christopher, D.B. Ingram, Plasmonic-metal nanostructures for efficient conversion of solar to chemical energy, Nature Mater. 10 (2011) 911–921.
[165] C. Hagglund, M. Zach, G. Petersson, B. Kasemo, Electromagnetic coupling of light into a silicon solar cell by nanodisk plasmons, Appl. Phys. Lett. 92 (2008) 383.
[166] A.O. Govorov, J. Lee, N.A. Kotov, Theory of plasmon-enhanced forster energy transfer in optically excited semiconductor and metal nanoparticles, Phys. Rev. B 76 (2007) 16.
[167] P. Anger, P. Bharadwaj, L. Novotny, Enhancement and quenching of single-molecule fluorescence, Phys. Rev. Lett. 96 (2006) 113002.
[168] K.E. Sapsford, L. Berti, I.L. Medintz, Materials for fluorescence resonance energy transfer analysis: Beyond traditional donor–acceptor combinations, Angew. Chem., Int. Ed. Engl. 45 (2006) 4562–4588.
[169] M.P. Singh, G.F. Strouse, Involvement of the LSPR spectral overlap for energy transfer between a dye and Au nanoparticle, J. Am. Chem. Soc. 132 (2010) 9383–9391.
[170] J.T. Li, S.K. Cushing, F.K. Meng, T.R. Senty, A.D. Bristow, N.Q. Wu, Plasmon-induced resonance energy transfer for solar energy conversion, Nat. Photon. 9 (2015) 601–607.
[171] Z. Zhang, J.T. Yates, Band bending in semiconductors: Chemical and physical consequences at surfaces and interfaces, Chem. Rev. 112 (2012) 5520–5551.
[172] A. Takai, P.V. Kamat, Capture, store, and discharge. shuttling photogenerated electrons across TiO_2-silver interface, ACS Nano 5 (2011) 7369–7376.
[173] Y. Tian, T. Tatsuma, Mechanisms and applications of plasmon-induced charge separation at TiO_2 films loaded with gold nanoparticles, J. Am. Chem. Soc. 127 (2005) 7632–7637.
[174] P. Christopher, D.B. Ingram, S. Linic, Enhancing photochemical activity of semiconductor nanoparticles with optically active Ag nanostructures: Photochemistry mediated by Ag surface plasmons, J. Phys. Chem. C 114 (2010) 9173–9177.
[175] X.B. Yin, Z.L. Ye, J. Rho, Y. Wang, X. Zhang, Photonic spin hall effect at metasurfaces, Science 339 (2013) 1405–1407.
[176] S. Mubeen, G. Hernandez-Sosa, D. Moses, J. Lee, M. Moskovits, Plasmonic photosensitization of a wide band gap semiconductor: Converting plasmons to charge Carriers, Nano Lett. 11 (2011) 5548–5552.
[177] Z.F. Bian, T. Tachikawa, P. Zhang, M. Fujitsuka, T. Majima, Au/TiO_2 superstructure-based plasmonic photocatalysts exhibiting efficient charge separation and unprecedented activity, J. Am. Chem. Soc. 136 (2014) 458–465.
[178] S. Mukherjee, F. Libisch, N. Large, O. Neumann, L.V. Brown, J. Cheng, J.B. Lassiter, E.A. Carter, P. Nordlander, N.J. Halas, Hot electrons do the impossible: Plasmon-induced dissociation of H-2 on Au, Nano Lett. 13 (2013) 240–247.
[179] G. Chen, Nonlocal and nonequilibrium heat conduction in the vicinity of nanoparticles, Trans. ASME, J. Heat Transfer 118 (1996) 539–545.
[180] J.R. Adleman, D.A. Boyd, D.G. Goodwin, D. Psaltis, Heterogenous catalysis mediated by plasmon heating, Nano Lett. 9 (2009) 4417–4423.
[181] K.A. Willets, R.P. Van Duyne, Localized surface plasmon resonance spectroscopy and sensing, Annu. Rev. Phys. Chem. 58 (2007) 267–297.
[182] M.R. Jones, K.D. Osberg, R.J. Macfarlane, M.R. Langille, C.A. Mirkin, Templated techniques for the synthesis and assembly of plasmonic nanostructures, Chem. Rev. 111 (2011) 3736–3827.
[183] J.C. Blancon, A.V. Stier, H. Tsai, W. Nie, C.C. Stoumpos, B. Traore, L. Pedesseau, M. Kepenekian, F. Katsutani, G.T. Noe, J. Kono, S. Tretiak, S.A. Crooker, C. Katan, M.G. Kanatzidis, J.J. Crochet, J. Even, A.D. Mohite, Scaling law for excitons in 2d perovskite quantum wells, Nature Commun. 9 (2018) 2254.
[184] Y. Chen, Y. Sun, J. Peng, J. Tang, K. Zheng, Z. Liang, 2d Ruddlesden-Popper perovskites for optoelectronics, Adv. Mater. 30 (2018) 1703487.
[185] H. Tsai, R. Asadpour, J.-C. Blancon, C.C. Stoumpos, J. Even, P.M. Ajayan, M.G. Kanatzidis, M.A. Alam, A.D. Mohite, W. Nie, Design principles for electronic charge transport in solution-processed vertically stacked 2d perovskite quantum wells, Nature Commun. 9 (2018) 2130.

[186] H. Tsai, W. Nie, J.-C. Blancon, C.C. Stoumpos, C.M.M. Soe, J. Yoo, J. Crochet, S. Tretiak, J. Even, A. Sadhanala, G. Azzellino, R. Brenes, P.M. Ajayan, V. Bulovic, S.D. Stranks, R.H. Friend, M.G. Kanatzidis, A.D. Mohite, Stable light-emitting diodes using phase-pure Ruddlesden-Popper layered perovskites, Adv. Mater. 30 (2018) 1704217.

[187] K. Ema, M. Inomata, Y. Kato, H. Kunugita, Nearly perfect triplet-triplet energy transfer from wannier excitons to naphthalene in organic–inorganic hybrid quantum-well materials, Phys. Rev. Lett. 100 (2008) 257401.

[188] D.B. Mitzi, K. Chondroudis, C.R. Kagan, Design, structure, and optical properties of organic–inorganic perovskites containing an oligothiophene chromophore, Inorg. Chem. 38 (1999) 6246–6256.

[189] K. Chondroudis, D.B. Mitzi, Electroluminescence from an organic–inorganic perovskite incorporating a quaterthiophene dye within lead halide perovskite layers, Chem. Mater. 11 (1999) 3028–3030.

[190] G.C. Papavassiliou, G. Pagona, G.A. Mousdis, N. Karousis, Enhanced phosphorescence from nanocrystalline/microcrystalline materials based on (CH_3NH_3)(1-naphthylmethyl ammonium)(2)Pb_2Cl_7 and similar compounds, Chem. Phys. Lett. 570 (2013) 80–84.

[191] K. Jemli, P. Audebert, L. Galmiche, G. Le Trippe-Allard, D. Garrot, J.S. Lauret, E. Deeporte, Two-dimensional perovskite activation with an organic luminophore, ACS Appl. Mater. Interfaces 7 (2015) 21763–21769.

[192] K. Kikuchi, Y. Takeoka, M. Rikukawa, K. Sanui, Fabrication and characterization of organic–inorganic perovskite films containing fullerene derivatives, Colloids Surf. A 257–58 (2005) 199–202.

[193] M. Era, T. Kobayashi, K. Sakaguchi, E. Tsukamoto, Y. Oishi, Electric conduction of pbbr-based layered perovskite organic–inorganic superlattice having carbazole chromophore-linked ammonium molecule as an organic layer, Organ. Electron. 14 (2013) 1313–1317.

[194] J.V. Passarelli, D.J. Fairfield, N.A. Sather, M.P. Hendricks, H. Sai, C.L. Stern, S.I. Stupp, Enhanced out-of-plane conductivity and photovoltaic performance in n=1 layered perovskites through organic cation design, J. Am. Chem. Soc. 140 (2018) 7313–7323.

[195] T.P. White, E. Deleporte, T.C. Sum, Feature issue introduction: halide perovskites for optoelectronics, Opt. Express 26 (2018) A153–A156.

[196] H.L. Wang, S.C. Liu, B. Balachandran, J. Moon, R. Haroldson, Z.T. Li, A. Ishteev, Q. Gu, W.D. Zhou, A. Zakhidov, W. Hu, Nanoimprinted perovskite metasurface for enhanced photoluminescence, Opt. Express 25 (2017) A1162–A1171.

[197] B. Gholipour, G. Adamo, D. Cortecchia, H.N.S. Krishnamoorthy, M.D. Birowosuto, N.I. Zheludev, C. Soci, Organometallic perovskite metasurfaces, Adv. Mater. 29 (2017) 1604286.

[198] S.V. Makarov, V. Milichko, E.V. Ushakova, M. Omelyanovich, A. Cerdan Pasaran, R. Haroldson, B. Balachandran, H. Wang, W. Hu, Y.S. Kivshar, A.A. Zakhidov, Multifold emission enhancement in nanoimprinted hybrid perovskite metasurfaces, ACS Photon. 4 (2017) 728–735.

[199] E. Tiguntseva, A. Che by kin, A. Ishteev, R. Haroldson, B. Balachandran, E. Ushakova, F. Komissarenko, H. Wang, V. Milichko, A. Tsypkin, D. Zuev, W. Hu, S. Makarov, A. Zakhidov, Resonant silicon nanoparticles for enhancement of light absorption and photoluminescence from hybrid perovskite films and metasurfaces, Nanoscale 9 (2017) 12486–12493.

[200] F. Yuan, Z.X. Wu, H. Dong, B. Xia, J. Xi, S.Y. Ning, L. Ma, X. Hou, Electric field-modulated amplified spontaneous emission in organo-lead halide perovskite $CH_3NH_3PbI_3$, Appl. Phys. Lett. 107 (2015) 261106.

[201] L. Dou, Y. Yang, J. You, Z. Hong, W.-H. Chang, G. Li, Y. Yang, Solution-processed hybrid perovskite photodetectors with high detectivity, Nature Commun. 5 (2014) 5404.

[202] Y. Fang, Q. Dong, Y. Shao, Y. Yuan, J. Huang, Highly narrowband perovskite single-crystal photodetectors enabled by surface-charge recombination, Nat. Photon. 9 (2015) 679–686.

[203] Y. Lee, J. Kwon, E. Hwang, C.-H. Ra, W.J. Yoo, J.-H. Ahn, J.H. Park, J.H. Cho, High-performance perovskite-graphene hybrid photodetector, Adv. Mater. 27 (2015) 41–46.

[204] Q. Lin, A. Armin, D.M. Lyons, P.L. Burn, P. Meredith, Low noise, IR-blind organohalide perovskite photodiodes for visible light detection and imaging, Adv. Mater. 27 (2015) 2060–2064.

[205] Z.Y. Wang, Q.D. Ou, Y.P. Zhang, Q.H. Zhang, H.Y. Hoh, Q.L. Bao, Degradation of two-dimensional $CH_3NH_3PbI_3$ perovskite and $CH_3NH_3PbI_3$/graphene heterostructure, ACS Appl. Mater. Interfaces 10 (2018) 24258–24265.

[206] P. Ramasamy, D.H. Lim, B. Kim, S.H. Lee, M.S. Lee, J.S. Lee, All-inorganic cesium lead halide perovskite nanocrystals for photodetector applications, Chem. Commun. 52 (2016) 2067–2070.

[207] J.Z. Song, L.M. Xu, J.H. Li, J. Xue, Y.H. Dong, X.M. Li, H.B. Zeng, Monolayer and few-layer all-inorganic perovskites as a new family of two-dimensional semiconductors for printable optoelectronic devices, Adv. Mater. 28 (2016) 4861–4869.

[208] Z.Q. Yang, Y.H. Deng, X.W. Zhang, S. Wang, H.Z. Chen, S. Yang, J. Khurgin, N.X. Fang, X. Zhang, R.M. Ma, High-performance single-crystalline perovskite thin-film photodetector, Adv. Mater. 30 (2018) 1704333.

[209] M.X. Sun, Q.Y. Fang, Z.P. Zhang, D. Xie, Y.L. Sun, J.L. Xu, W.W. Li, T.L. Ren, Y.F. Zhang, All-inorganic perovskite nanowires ingazno heterojunction for high-performance ultraviolet visible photodetectors, ACS Appl. Mater. Interfaces 10 (2018) 7231–7238.

[210] K.W. Liu, M. Sakurai, M.Y. Liao, M. Aono, Giant improvement of the performance of ZnO nanowire photodetectors by Au nanoparticles, J. Phys. Chem. C 114 (2010) 19835–19839.

[211] K. Okamoto, I. Niki, A. Shvartser, Y. Narukawa, T. Mukai, A. Scherer, Surface-plasmon-enhanced light emitters based on InGaN quantum wells, Nature Mater. 3 (2004) 601–605.

[212] S.C. Lee, S. Krishna, S.R.J. Brueck, Quantum dot infrared photodetector enhanced by surface plasma wave excitation, Opt. Express 17 (2009) 23160–23168.

[213] Y.G. Sun, B. Mayers, Y.N. Xia, Metal nanostructures with hollow interiors, Adv. Mater. 15 (2003) 641–646.

[214] C. Zhang, S.Z. Jiang, Y.Y. Huo, A.H. Liu, S.C. Xu, X.Y. Liu, Z.C. Sun, Y.Y. Xu, Z. Li, B.Y. Man, SERS detection of R6G based on a novel graphene oxide/silver nanoparticles/silicon pyramid arrays structure, Opt. Express 23 (2015) 24811–24821.

[215] Z.H. Sun, L. Aigouy, Z.Y. Chen, Plasmonic-enhanced perovskite-graphene hybrid photodetectors, Nanoscale 8 (2016) 7377–7383.

[216] H. Wang, J.W. Lim, L.N. Quan, K. Chung, Y.J. Jang, Y. Ma, D.H. Kim, Perovskite-gold nanorod hybrid photodetector with high responsivity and low driving voltage, Adv. Opt. Mater. 6 (2018) 1701397.

[217] L. Tang, S.E. Kocabas, S. Latif, A.K. Okyay, D.S. Ly-Gagnon, K.C. Saraswat, D.A.B. Miller, Nanometre-scale germanium photodetector enhanced by a near-infrared dipole antenna, Nat. Photon. 2 (2008) 226–229.

[218] A. Sobhani, M.W. Knight, Y.M. Wang, B. Zheng, N.S. King, L.V. Brown, Z.Y. Fang, P. Nordlander, N.J. Halas, Narrowband photodetection in the near-infrared with a plasmon-induced hot electron device, Nature Commun. 4 (2013) 1643.

[219] M. Furchi, A. Urich, A. Pospischil, G. Lilley, K. Unterrainer, H. Detz, P. Klang, A.M. Andrews, W. Schrenk, G. Strasser, T. Mueller, Microcavity-integrated graphene photodetector, Nano Lett. 12 (2012) 2773–2777.

[220] M. Konstantakou, D. Perganti, P. Falaras, T. Stergiopoulos, Anti-solvent crystallization strategies for highly efficient perovskite solar cells, Crystals 7 (2017) 21.

[221] J. Song, L. Xu, J. Li, J. Xue, Y. Dong, X. Li, H. Zeng, Monolayer and few-layer all-inorganic perovskites as a new family of two-dimensional semiconductors for printable optoelectronic devices, Adv. Mater. 28 (2016) 4861–4869.

[222] A. Ng, Z. Ren, H. Hu, P.W.K. Fong, Q. Shen, S.H. Cheung, P. Qin, J.W. Lee, A.B. Djurišić, S.K. So, G. Li, Y. Yang, C. Surya, Cryogenic process for antisolvent-free high performance perovskite solar cells, Adv. Mater. 30 (2018) 1804402.

[223] J. Yang, J.B. You, C.C. Chen, W.C. Hsu, H.R. Tan, X.W. Zhang, Z.R. Hong, Y. Yang, Plasmonic polymer tandem solar cell, ACS Nano 5 (2011) 6210–6217.

[224] K.R. Catchpole, A. Polman, Plasmonic solar cells, Opt. Express 16 (2008) 21793–21800.

[225] P. Reineck, G.P. Lee, D. Brick, M. Karg, P. Mulvaney, U. Bach, A solid-state plasmonic solar cell via metal nanoparticle self-assembly, Adv. Mater. 24 (2012) 4750–4755.

[226] M. Saliba, W. Zhang, V.M. Burlakov, S.D. Stranks, Y. Sun, J.M. Ball, M.B. Johnston, A. Goriely, U. Wiesner, H.J. Snaith, Plasmonic-induced photon recycling in metal halide perovskite solar cells, Adv. Funct. Mater. 25 (2015) 5038–5046.

[227] A. Jiménez-Solano, S. Carretero-Palacios, H. Míguez, Absorption enhancement in methylammonium lead iodide perovskite solar cells with embedded arrays of dielectric particles, Opt. Express 26 (2018) A865–A878.

[228] A. Furasova, E. Calabró, E. Lamanna, E. Tiguntseva, E. Ushakova, E. Ubyivovk, V. Mikhailovskii, A. Zakhidov, S. Makarov, A. Di Carlo, Resonant silicon nanoparticles for enhanced light harvesting in halide perovskite solar cells, Adv. Opt. Mater. 6 (2018) 1800576.

[229] S.S. Mali, C.S. Shim, H. Kim, P.S. Patil, C.K. Hong, In situ processed gold nanoparticle-embedded TiO_2 nanofibers enabling plasmonic perovskite solar cells to exceed 14% conversion efficiency, Nanoscale 8 (2016) 2664–2677.

[230] Q. Luo, C.X. Zhang, X.S. Deng, H.B. Zhu, Z.Q. Li, Z.B. Wang, X.H. Chen, S.M. Huang, Plasmonic effects of metallic nanoparticles on enhancing performance of perovskite solar cells, ACS Appl. Mater. Interfaces 9 (2017) 34821–34832.

[231] S. Carretero-Palacios, A. Jiménez-Solano, H. Míguez, Plasmonic nanoparticles as light-harvesting enhancers in perovskite solar cells: A user's guide, ACS Energy Lett. 1 (2016) 323–331.

[232] M.Z. Long, Z.F. Chen, T.K. Zhang, Y.B. Xiao, X.L. Zeng, J. Chen, K.Y. Yan, J.B. Xu, Ultrathin efficient perovskite solar cells employing a periodic structure of a composite hole conductor for elevated plasmonic light harvesting and hole collection, Nanoscale 8 (2016) 6290–6299.

[233] C.K. Lim, Q. Li, T. Zhang, T. Thomay, A.N. Cartwright, M.T. Swihart, P.N. Prasad, Enhanced fatigue resistance of suppressed hysteresis in perovskite solar cells by an organic crosslinker, Sol. Energy Mater. Sol. Cells 176 (2018) 30–35.

[234] H.H. Tsai, W.Y. Nie, J.C. Blancon, C.C.S. Toumpos, R. Asadpour, B. Harutyunyan, A.J. Neukirch, R. Verduzco, J.J. Crochet, S. Tretiak, L. Pedesseau, J. Even, M.A. Alam, G. Gupta, J. Lou, P.M. Ajayan, M.J. Bedzyk, M.G. Kanatzidis, A.D. Mohite, High-efficiency two-dimensional Ruddlesden-Popper perovskite solar cells, Nature 536 (2016) 312–316.

[235] J.C. Blancon, H. Tsai, W. Nie, C.C. Stoumpos, L. Pedesseau, C. Katan, M. Kepenekian, C.M.M. Soe, K. Appavoo, M.Y. Sfeir, S. Tretiak, P.M. Ajayan, M.G. Kanatzidis, J. Even, J.J. Crochet, A.D. Mohite, Perovskite physics extremely efficient internal exciton dissociation through edge states in layered 2d perovskites, Science 355 (2017) 1288–1291.

[236] M. Lira-Cantu, Perovskite solar cells stability lies at interfaces, Nat. Energy 2 (2017) 17115.

[237] P. Pust, P.J. Schmidt, W. Schnick, A revolution in lighting, Nature Mater. 14 (2015) 454–458.

[238] J.Z. Song, J.H. Li, X.M. Li, L.M. Xu, Y.H. Dong, H.B. Zeng, Quantum dot light-emitting diodes based on inorganic perovskite cesium lead halides ($CsPbX_3$), Adv. Mater. 27 (2015) 7162–7167.

[239] X. Li, Y. Wu, S. Zhang, B. Cai, Y. Gu, J. Song, H. Zeng, $CsPbX_3$ quantum dots for lighting and displays: Room-temperature synthesis, photoluminescence superiorities, underlying origins and white light-emitting diodes, Adv. Funct. Mater. 26 (2016) 2435–2445.

[240] J. Li, L. Xu, T. Wang, J. Song, J. Chen, J. Xue, Y. Dong, B. Cai, Q. Shan, B. Han, H. Zeng, 50-fold EQE improvement up to 6.27% of solution-processed all-inorganic perovskite $CsPbBr_3$ QLEDs via surface ligand density control, Adv. Mater. 29 (2017) 1603885.

[241] J. Song, J. Li, L. Xu, J. Li, F. Zhang, B. Han, Q. Shan, H. Zeng, Room-temperature triple-ligand surface engineering synergistically boosts ink stability, ecombination dynamics, and charge injection toward EQE-11.6% perovskite QLEDs,, Adv. Mater. 30 (2018) e1800764.

[242] Z.K. Tan, R.S. Moghaddam, M.L. Lai, P. Docampo, R. Higler, F. Deschler, M. Price, A. Sadhanala, L.M. Pazos, D. Credgington, F. Hanusch, T. Bein, H.J. Snaith, R.H. Friend, Bright light-emitting diodes based on organometal halide perovskite, Nature Nanotechnol. 9 (2014) 687–692.

[243] F.A. Ponce, D.P. Bour, W. Gotz, N.M. Johnson, H.I. Helava, I. Grzegory, J. Jun, Homoepitaxy of GaN on polished bulk single crystals by metalorganic chemical vapor deposition, Appl. Phys. Lett. 68 (1996) 917–919.

[244] H.-W. Lin, Y.-J. Lu, H.-Y. Chen, H.-M. Lee, S. Gwo, InGaN/GaN nanorod array white light-emitting diode, Appl. Phys. Lett. 97 (2010) 1274.

[245] Y. Jiang, Y. Li, Y. Li, Z. Deng, T. Lu, Z. Ma, P. Zuo, L. Dai, L. Wang, H. Jia, W. Wang, J. Zhou, W. Liu, H. Chen, Realization of high-luminous-efficiency ingan light-emitting diodes in the green gap range, Sci. Rep. 5 (2015) 10883.

[246] H.C. Cho, S.H. Jeong, M.H. Park, Y.H. Kim, C. Wolf, C.L. Lee, J.H. Heo, A. Sadhanala, N. Myoung, S. Yoo, S.H. Im, R.H. Friend, T.W. Lee, Overcoming the electroluminescence efficiency limitations of perovskite light-emitting diodes, Science 350 (2015) 1222–1225.

[247] N. Wang, L. Cheng, R. Ge, S. Zhang, Y. Miao, W. Zou, C. Yi, Y. Sun, Y. Cao, R. Yang, Y. Wei, Q. Guo, Y. Ke, M. Yu, Y. Jin, Y. Liu, Q. Ding, D. Di, L. Yang, G. Xing, H. Tian, C. Jin, F. Gao, R.H. Friend, J. Wang, W. Huang, Perovskite light-emitting diodes based on solution-processed self-organized multiple quantum wells, Nat. Photon. 10 (2016) 699–704.

[248] M. Yuan, Q. Li Na, R. Comin, G. Walters, R. Sabatini, O. Voznyy, S. Hoogland, Y. Zhao, E.M. Beauregard, P. Kanjanaboos, Z. Lu, D.H. Kim, E.H. Sargent, Perovskite energy funnels for efficient light-emitting diodes, Nature Nanotechnol. 11 (2016) 872–877.

[249] Z.G. Xiao, R.A. Kerner, L.F. Zhao, N.L. Tran, K.M. Lee, T.W. Koh, G.D. Scholes, B.P. Rand, Efficient perovskite light-emitting diodes featuring nanometre-sized crystallites, Nat. Photon. 11 (2017) 108–115.

[250] Y. Zhang, J. Liu, Z. Wang, Y. Xue, Q. Ou, L. Polavarapu, J. Zheng, X. Qi, Q. Bao, Synthesis, properties, and optical applications of low-dimensional perovskites, Chem. Commun. 52 (2016) 13637–13655.

[251] X.L. Zhang, B. Xu, W.G. Wang, S. Liu, Y.J. Zheng, S.M. Chen, K. Wang, X.W. Sun, Plasmonic perovskite light-emitting diodes based on the Ag-$CsPbBr_3$ system, ACS Appl. Mater. Interfaces 9 (2017) 4926–4931.

[252] P. Chen, Z.Y. Xiong, X.Y. Wu, M. Shao, Y. Meng, Z.H. Xiong, C.H. Gao, Nearly 100% efficiency enhancement of $CH_3NH_3PbBr_3$ perovskite light-emitting diodes by utilizing plasmonic Au nanoparticles, J. Phys. Chem. Lett. 8 (2017) 3961–3969.

[253] Y. Meng, X.Y. Wu, Z.Y. Xiong, C.Y. Lin, Z.H. Xiong, E. Blount, P. Chen, Electrode quenching control for highly efficient $CsPbBr_3$ perovskite light-emitting diodes via surface plasmon resonance and enhanced hole injection by Au nanoparticles, Nanotechnology 29 (2018) 175203.

[254] W. Ding, Y.X. Wang, H. Chen, S.Y. Chou, Plasmonic nanocavity organic light-emitting diode with significantly enhanced light extraction, contrast, viewing angle, brightness, and low-glare, Adv. Funct. Mater. 24 (2014) 6329–6339.

[255] C.H. Liu, G. Clark, T. Fryett, S.F. Wu, J.J. Zheng, F. Hatami, X.D. Xu, A. Majumdar, Nanocavity integrated van der waals heterostructure light-emitting tunneling diode, Nano Lett. 17 (2017) 200–205.

[256] S. Jeon, S. Lee, K.H. Han, H. Shin, K.H. Kim, J.H. Jeong, J.J. Kim, High-quality white OLEDs with comparable efficiencies to LEDs, Adv. Opt. Mater. 6 (2018) 1701349.

[257] H.M. Presby, A.F. Benner, C.A. Edwards, Laser micromachining of efficient fiber microlenses, Appl. Opt. 29 (1990) 2692–2695.

[258] N.F. Rulkov, M.A. Vorontsov, L. Illing, Chaotic free-space laser communication over a turbulent channel, Phys. Rev. Lett. 89 (2002) 277905.

[259] H.-R. Jiang, N. Yoshinaga, M. Sano, Active motion of a janus particle by self-thermophoresis in a defocused laser beam, Phys. Rev. Lett. 105 (2010) 268302.

[260] J.-P. Colletier, M.R. Sawaya, M. Gingery, J.A. Rodriguez, D. Cascio, A.S. Brewster, T. Michels-Clark, R.H. Hice, N. Coquelle, S. Boutet, G.J. Williams, M. Messerschmidt, D.P. DePonte, R.G. Sierra, H. Laksmono, J.E. Koglin, M.S. Hunter, H.-W. Park, M. Uervirojnangkoorn, D.K. Bideshi, A.T. Brunger, B.A. Federici, N.K. Sauter, D.S. Eisenberg, De novo phasing with X-ray laser reveals mosquito larvicide binAB structure, Nature 539 (2016) 43–47.

[261] B.R. Sutherland, S. Hoogland, M.M. Adachi, C.T.O. Wong, E.H. Sargent, Conformal organohalide perovskites enable lasing on spherical resonators, ACS Nano 8 (2014) 10947–10952.

[262] X.F. Liu, L. Niu, C.Y. Wu, C.X. Cong, H. Wang, Q.S. Zeng, H.Y. He, Q.D. Fu, W. Fu, T. Yu, C.H. Jin, Z. Liu, T.C. Sum, Periodic organic-inorganic halide perovskite microplatelet arrays on silicon substrates for room-temperature lasing, Adv. Sci. 3 (2016) 1600137.

[263] C. Huang, W. Sun, Y. Fan, Y. Wang, Y. Gao, N. Zhang, K. Wang, S. Liu, S. Wang, S. Xiao, Q. Song, Formation of lead halide perovskite based plasmonic nanolasers and nanolaser arrays by tailoring the substrate, ACS Nano 12 (2018) 3865–3874.

[264] Y. Chen, M. Yu, S. Ye, J. Song, J. Qu, All-inorganic $CsPbBr_3$ perovskite quantum dots embedded in dual-mesoporous silica with moisture resistance for two-photon-pumped plasmonic nanolasers, Nanoscale 10 (2018) 6704–6711.

[265] T.P. Zhang, S. Callard, C. Jamois, C. Chevalier, D. Feng, A. Belarouci, Plasmonic-photonic crystal coupled nanolaser, Nanotechnology 25 (2014) 315201.

[266] Y. Zhang, Y. Wang, Z.-Q. Xu, J. Liu, J. Song, Y. Xue, Z. Wang, J. Zheng, L. Jiang, C. Zheng, F. Huang, B. Sun, Y.-B. Cheng, Q. Bao, Reversible structural swell–shrink and recoverable optical properties in hybrid inorganic–organic perovskite, ACS Nano 10 (2016) 7031–7038.

[267] K. Wang, W. Sun, J. Li, Z. Gu, S. Xiao, Q. Song, Unidirectional lasing emissions from $CH_3NH_3PbBr_3$ perovskite microdisks, ACS Photon. 3 (2016) 1125–1130.

[268] R.F. Oulton, V.J. Sorger, D.A. Genov, D.F.P. Pile, X. Zhang, A hybrid plasmonic waveguide for subwavelength confinement and long-range propagation, Nat. Photon. 2 (2008) 496–500.

[269] G. Walters, B.R. Sutherland, S. Hoogland, D. Shi, R. Comin, D.P. Sellan, O.M. Bake, E.H. Sargent, Two-photon absorption in organometallic bromide perovskites, ACS Nano 9 (2015) 9340–9346.

[270] B.S. Kalanoor, L. Gouda, R. Gottesman, S. Tirosh, E. Haltzi, A. Zaban, Y.R. Tischler, Third-order optical nonlinearities in organometallic methylammonium lead iodide perovskite thin films, ACS Photon. 3 (2016) 361–370.

[271] Y. Wang, X. Li, X. Zhao, L. Xiao, H. Zeng, H. Sun, Nonlinear absorption and low-threshold multiphoton pumped stimulated emission from all-inorganic perovskite nanocrystals, Nano Lett. 16 (2016) 448–453.

[272] A. Manzi, Y. Tong, J. Feucht, E.-P. Yao, L. Polavarapu, A.S. Urban, J. Feldmann, Resonantly enhanced multiple exciton generation through below-band-gap multi-photon absorption in perovskite nanocrystals, Nature Commun. 9 (2018) 1518.

[273] K. Wei, Z.J. Xu, R.Z. Chen, X. Zheng, X.G. Cheng, T. Jiang, Temperature-dependent excitonic photoluminescence excited by two-photon absorption in perovskite $CsPbBr_3$ quantum dots, Opt. Lett. 41 (2016) 3821–3824.

[274] Z.Y. Gu, K.Y. Wang, W.Z. Sun, J.K. Li, S. Liu, Q.H. Song, S.M. Xiao, Two-photon pumped $CH_3NH_3PbBr_3$ perovskite microwire lasers, Adv. Opt. Mater. 4 (2016) 472–479.

[275] Y.S. Gao, S. Wang, C. Huang, N.B. Yi, K.Y. Wang, S.M. Xiao, Q.H. Song, Room temperature three-photon pumped $CH_3NH_3PbBr_3$ perovskite microlasers, Sci. Rep. 7 (2017) 45391.

[276] F.O. Saouma, C.C. Stoumpos, M.G. Kanatzidis, Y.S. Kim, J.I. Jang, Multiphoton absorption order of $CsPbBr_3$ as determined by wavelength-dependent nonlinear optical spectroscopy, J. Phys. Chem. Lett. 8 (2017) 4912–4917.

[277] W. Chen, S. Bhaumik, S.A. Veldhuis, G. Xing, Q. Xu, M. Gratzel, S. Mhaisalkar, N. Mathews, T.C. Sum, Giant five-photon absorption from multidimensional core–shell halide perovskite colloidal nanocrystals, Nature Commun. 8 (2017) 15198.

[278] D. Yang, S. Chu, Y. Wang, C.K. Siu, S. Pan, S.F. Yu, Frequency upconverted amplified spontaneous emission and lasing from inorganic perovskite under simultaneous six-photon absorption, Opt. Lett. 43 (2018) 2066–2069.

[279] Y. Zhou, Z.P. Hu, Y. Li, J.Q. Xu, X.S. Tang, Y.L. Tang, $CsPbBr_3$ nanocrystal saturable absorber for mode-locking ytterbium fiber laser, Appl. Phys. Lett. 108 (2016) 831.

[280] M. Isarov, L.Z. Tan, M.I. Bodnarchuk, M.V. Kovalenko, A.M. Rappe, E. Lifshitz, Rashba effect in a single colloidal $CsPbBr_3$ perovskite nanocrystal detected by magneto-optical measurements, Nano Lett. 17 (2017) 5020–5026.

[281] S.Y. Liu, X.H. Fang, Y.M. Wang, X.P. Zhang, Two-photon pumped amplified spontaneous emission based on all-inorganic perovskite nanocrystals embedded with gold nanorods, Opt. Mater. 81 (2018) 55–58.

[282] W. Liu, X. Li, Y. Song, C. Zhang, X. Han, H. Long, B. Wang, K. Wang, P. Lu, Cooperative enhancement of two-photon-absorption-induced photoluminescence from a 2d perovskite-microsphere hybrid dielectric structure, Adv. Funct. Mater. 28 (2018) 1707550.

[283] Z. Wang, Z. Dong, H. Zhu, L. Jin, M.-H. Chiu, L.-J. Li, Q.-H. Xu, G. Eda, S.A. Maier, A.T.S. Wee, C.-W. Qiu, J.K.W. Yang, Selectively plasmon-enhanced second-harmonic generation from monolayer tungsten diselenide on flexible substrates, ACS Nano 12 (2018) 1859–1867.

[284] H. Aouani, M. Rahmani, M. Navarro-Cia, S.A. Maier, Third-harmonic-upconversion enhancement from a single semiconductor nanoparticle coupled to a plasmonic antenna, Nature Nanotechnol. 9 (2014) 290–294.

[285] A. Baev, P.N. Prasad, H. Agren, M. Samoc, M. Wegener, Metaphotonics: An emerging field with opportunities and challenges, Phys. Rep. 594 (2015) 1–60.

[286] I. Liberal, N. Engheta, Near-zero refractive index photonics, Nat. Photon. 11 (2017) 149–158.

[287] X. Liu, W.C. Law, M. Jeon, X.L. Wang, M.X. Liu, C. Kim, P.N. Prasad, M.T. Swihart, Cu2-xSe nanocrystals with localized surface plasmon resonance as sensitive contrast agents for in vivo photoacoustic imaging: Demonstration of sentinel lymph node mapping, Adv. Healthcare Mater. 2 (2013) 952–957.

[288] C.C. Stoumpos, C.D. Malliakas, J.A. Peters, Z. Liu, M. Sebastian, J. Im, T.C. Chasapis, A.C. Wibowo, D.Y. Chung, A.J. Freeman, B.W. Wessels, M.G. Kanatzidis, Crystal growth of the perovskite semiconductor $CsPbBr_3$: A new material for high-energy radiation detection, Cryst. Growth Des. 13 (2013) 2722–2727.

[289] H. Wei, D. DeSantis, W. Wei, Y. Deng, D. Guo, T.J. Savenije, L. Cao, J. Huang, Dopant compensation in alloyed $CH_3NH_3PbBr_3$-xClx perovskite single crystals for gamma-ray spectroscopy, Nature Mater. 16 (2017) 826.

[290] Y. He, L. Matei, H.J. Jung, K.M. McCall, M. Chen, C.C. Stoumpos, Z. Liu, J.A. Peters, D.Y. Chung, B.W. Wessels, M.R. Wasielewski, V.P. Dravid, A. Burger, M.G. Kanatzidis, High spectral resolution of gamma-rays at room temperature by perovskite $CsPbBr_3$ single crystals, Nature Commun. 9 (2018) 1609.

[291] S. Yakunin, M. Sytnyk, D. Kriegner, S. Shrestha, M. Richter, G.J. Matt, H. Azimi, C.J. Brabec, J. Stangl, M.V. Kovalenko, W. Heiss, Detection of X-ray photons by solution-processed lead halide perovskites, Nat. Photon. 9 (2015) 444.

[292] S. Shrestha, R. Fischer, G.J. Matt, P. Feldner, T. Michel, A. Osvet, I. Levchuk, B. Merle, S. Golkar, H. Chen, S.F. Tedde, O. Schmidt, R. Hock, M. Rührig, M. Göken, W. Heiss, G. Anton, C.J. Brabec, High-performance direct conversion X-ray detectors based on sintered hybrid lead triiodide perovskite wafers, Nat. Photon. 11 (2017) 436.

[293] Y.C. Kim, K.H. Kim, D.-Y. Son, D.-N. Jeong, J.-Y. Seo, Y.S. Choi, I.T. Han, S.Y. Lee, N.-G. Park, Printable organometallic perovskite enables large-area, low-dose X-ray imaging, Nature 550 (2017) 87.

[294] Q. Chen, J. Wu, X. Ou, B. Huang, J. Almutlaq, A.A. Zhumekenov, X. Guan, S. Han, L. Liang, Z. Yi, J. Li, X. Xie, Y. Wang, Y. Li, D. Fan, D.B.L. Teh, A.H. All, O.F. Mohammed, O.M. Bakr, T. Wu, M. Bettinelli, H. Yang, W. Huang, X. Liu, All-inorganic perovskite nanocrystal scintillators, Nature 561 (2018) 88–93.

[295] C. Zhang, D. Sun, C.X. Sheng, Y.X. Zhai, K. Mielczarek, A. Zakhidov, Z.V. Vardeny, Magnetic field effects in hybrid perovskite devices, Nat. Phys. 11 (2015) 427.

[296] P. Odenthal, W. Talmadge, N. Gundlach, R. Wang, C. Zhang, D. Sun, Z.-G. Yu, Z. Valy Vardeny, Y.S. Li, Spin-polarized exciton quantum beating in hybrid organic–inorganic perovskites, Nat. Phys. 13 (2017) 894.

[297] D. Niesner, M. Wilhelm, I. Levchuk, A. Osvet, S. Shrestha, M. Batentschuk, C. Brabec, T. Fauster, Giant rashba splitting in $CH_3NH_3PbBr_3$ organic-inorganic perovskite, Phys. Rev. Lett. 117 (2016) 126401.

[298] Y. Zhai, S. Baniya, C. Zhang, J. Li, P. Haney, C.-X. Sheng, E. Ehrenfreund, Z.V. Vardeny, Giant rashba splitting in 2d organic–inorganic halide perovskites measured by transient spectroscopies, Sci. Adv. 3 (2017) e1700704.

[299] Y.-C. Hsiao, T. Wu, M. Li, B. Hu, Magneto-optical studies on spin-dependent charge recombination and dissociation in perovskite solar cells, Adv. Mater. 27 (2015) 2899–2906.

[300] M. Fu, P. Tamarat, H. Huang, J. Even, A.L. Rogach, B. Lounis, Neutral and charged exciton fine structure in single lead halide perovskite nanocrystals revealed by magneto-optical spectroscopy, Nano Lett. 17 (2017) 2895–2901.
[301] G. Long, C. Jiang, R. Sabatini, Z. Yang, M. Wei, L.N. Quan, Q. Liang, A. Rasmita, M. Askerka, G. Walters, X. Gong, J. Xing, X. Wen, R. Quintero-Bermudez, H. Yuan, G. Xing, X.R. Wang, D. Song, O. Voznyy, M. Zhang, S. Hoogland, W. Gao, Q. Xiong, E.H. Sargent, Spin control in reduced-dimensional chiral perovskites, Nat. Photon. 12 (2018) 528–533.
[302] Y.-M. He, G. Clark, J.R. Schaibley, Y. He, M.-C. Chen, Y.-J. Wei, X. Ding, Q. Zhang, W. Yao, X. Xu, C.-Y. Lu, J.-W. Pan, Single quantum emitters in monolayer semiconductors, Nature Nanotechnol. 10 (2015) 497.
[303] Y.-S. Park, S. Guo, N.S. Makarov, V.I. Klimov, Room temperature single-photon emission from individual perovskite quantum dots, ACS Nano 9 (2015) 10386–10393.